INTEGRATION OF POLYPYRROLE WITH METAL COMPLEXES OF 2,6-PYRIDINEDICARBOXYLIC ACID AND THEIR ELECTROCHEMICAL STUDIES AS POTENTIAL ELECTRODE MATERIAL IN SUPERCAPACITOR APPLICATION

SADIA TANZIM

FACULTY OF SCIENCE
UNIVERSITI MALAYA
KUALA LUMPUR

2023

INTEGRATION OF POLYPYRROLE WITH METAL COMPLEXES OF 2,6-PYRIDINEDICARBOXYLIC ACID AND THEIR ELECTROCHEMICAL STUDIES AS POTENTIAL ELECTRODE MATERIAL IN SUPERCAPACITOR APPLICATION

SADIA TANZIM

DISSERTATION SUBMITTED IN FULFILMENT OF THE REQUIREMENTS FOR THE DEGREE OF MASTER OF SCIENCE

DEPARTMENT OF CHEMISTRY
FACULTY OF SCIENCE
UNIVERSITI MALAYA
KUALA LUMPUR

2023

UNIVERSITI MALAYA

ORIGINAL LITERARY WORK DECLARATION

Name of Candidate: **SADIA TANZIM**

Registration/Matric No: **S2129487/1**

Name of Degree: **MASTER OF SCIENCE**

Title of Project Paper/Research Report/Dissertation/Thesis ("this Work"):

Integration of Polypyrrole with Metal Complexes of 2,6-Pyridinedicarboxylic Acid and their Electrochemical Studies as Potential Electrode Material in Supercapacitor Application.

Field of Study: **CHEMISTRY**

I do solemnly declare that:

(1) I am the sole author/writer of this Work;
(2) This Work is original;
(3) Any use of any work in which copyright exists was done by way of fair dealing and for permitted purposes and any excerpt or extract from, or reference to or reproduction of any copyright work has been disclosed expressly and sufficiently and the title of the Work and its authorship have been acknowledged in this Work;
(4) I do not have any actual knowledge nor do I ought reasonably to know that the making of this work constitutes an infringement of any copyright work;
(5) I hereby assign all and every rights in the copyright to this Work to the University of Malaya ("UM"), who henceforth shall be owner of the copyright in this Work and that any reproduction or use in any form or by any means whatsoever is prohibited without the written consent of UM having been first had and obtained;
(6) I am fully aware that if in the course of making this Work I have infringed any copyright whether intentionally or otherwise, I may be subject to legal action or any other action as may be determined by UM.

Candidate's Signature

Date: 10th December 2023

Subscribed and solemnly declared befc

Witness's Signature

Date: 10th December 2023

Name:

Designation:

INTEGRATION OF POLYPYRROLE WITH METAL COMPLEXES OF 2,6-PYRIDINEDICARBOXYLIC ACID AND THEIR ELECTROCHEMICAL STUDIES AS POTENTIAL ELECTRODE MATERIAL IN SUPERCAPACITOR APPLICATION

ABSTRACT

In this study, four transition metal complexes of PDC namely: AgPDC, CdPDC, CuPDC and ZnPDC were synthesized, characterized and integrated with polypyrrole (PPY) to create four new composite materials: PPY-AgPDC, PPY-CdPDC, PPY-CuPDC and PPY-ZnPDC for studying their electrochemical performance. PPY and the composites were synthesized using two techniques: *in*-situ oxidative polymerization (powder) and electrochemical polymerization (thin films). The composite materials were characterized by FTIR spectroscopic technique, powder X-ray diffraction technique, TGA, FESEM and EDX. XRD studies reveal AgPDC, CuPDC and ZnPDC were similar to previously reported structures whereas CdPDC was identified as a new crystal structure. FESEM analysis of powder composites revealed that the complexes were encapsulated by the microspheres of PPY with an average size of 0.5 µm whereas, analysis of the film composites revealed that the complexes were embedded irregularly within the PPY microspheres with an average size of 1.2 µm. Powder PPY and its composites were mixed with carbon black and PVDF to form slurry and coated evenly over graphite sheet as working electrode. With Ag/AgCl reference and Pt wire counter electrode, the CV was performed in room temperature at potential range of -0.2 V to +0.8 V in 1 M H_2SO_4 electrolyte. Thin films of PPY and its composites on ITO glass as working electrode with Ag/AgCl reference and graphite rod counter electrode was used to perform CV in room temperature at potential range of -0.5 V to +0.9 V in 0.01 M $K_3[Fe(CN)_6]$ + 0.1M KCl electrolyte solution. Based on the shape of the voltammograms at 10 $mV.s^{-1}$ scan rate, the powder composites exhibited improved capacitive behaviour and the film composites exhibited better pseudocapacitive behaviour than PPY. EIS of the powder composites was performed in the same electrochemical cell set-up as CV, meanwhile the films were extracted from ITO and performed directly. The conductivity values determined for PPY powder slurry was 8.62×10^{-4} S.cm^{-1} and for PPY film was 1.04×10^{-5} S.cm^{-1}. Powder composites exhibited conductivity in the range of $1.03 \times 10^{-3} – 4.41 \times 10^{-3}$ S.cm^{-1} and film composites were in range of $4.78 \times 10^{-5} – 2.16 \times 10^{-5}$ S.cm^{-1}. All fabricated composites achieved higher conductivities, reduced resistance, than pure PPY. These electrochemical traits are promising for their future application as supercapacitors.

Keywords: supercapacitors, polypyrrole, 2,6-pyridinedicarboxylic acid, metal complex, electrochemical studies

ABSTRAK

Dalam kajian ini, empat kompleks logam peralihan PDC iaitu: AgPDC, CdPDC, CuPDC dan ZnPDC telah disintesis, dicirikan, dan diintegrasikan dengan polipirrol (PPY) membentuk empat bahan komposit baru: PPY-AgPDC, PPY-CdPDC, PPY-CuPDC dan PPY-ZnPDC untuk mengkaji prestasi elektrokimia mereka. PPY dan kompositnya disintesis menggunakan dua teknik yang berbeza: polimerisasi oksidatif in-situ (sampel berbentuk serbuk) dan polimerisasi elektrokimia (sampel berbentuk filem). Bahan komposit ini dicirikan menggunakan teknik spektroskopi FTIR, teknik difraksi sinar-X serbuk, TGA, FESEM dan EDX. Kajian XRD mendedahkan bahawa AgPDC, CuPDC dan ZnPDC serupa dengan struktur yang dilaporkan sebelum ini, sementara CdPDC dikenal pasti sebagai struktur hablur baru. Analisis FESEM terhadap komposit serbuk menunjukkan kompleks itu diapit oleh mikrosfera PPY dengan saiz purata 0.5 µm, manakala analisis komposit filem menunjukkan kompleks itu terbenam secara tidak teratur dalam mikrosfera PPY dengan saiz purata 1.2 µm. Serbuk PPY dan kompositnya dicampur dengan arang hitam dan PVDF untuk membentuk larutan dan disapu rata ke atas sehelai kertas grafit sebagai elektrod kerja. Dengan elektrod rujukan Ag/AgCl dan elektrod kontra wayar Pt, CV dijalankan pada suhu bilik pada julat voltan -0.2 V hingga +0.8 V dalam elektrolit 1 M H_2SO_4. Filem nipis PPY dan kompositnya pada kaca ITO sebagai elektrod kerja dengan elektrod rujukan Ag/AgCl dan elektrod kontra batang grafit digunakan untuk menjalankan CV pada suhu bilik pada julat voltan -0.5 V hingga +0.9 V dalam larutan elektrolit 0.01 M $K_3[Fe(CN)_6]$ + 0.1 M KCl. Berdasarkan bentuk voltamogram pada kadar pindaan 10 mV.s-1, komposit serbuk menunjukkan tingkah laku kapasitif yang lebih baik dan komposit filem menunjukkan tingkah laku palsu-kapasitif yang lebih baik daripada PPY. EIS komposit serbuk dijalankan dalam set-up sel elektrokimia yang sama seperti CV, sementara filem diekstrak dari ITO dan dijalankan secara langsung. Nilai kekonduksian yang ditentukan untuk larutan serbuk PPY adalah 8.62×10^{-4} S.cm^{-1} dan untuk filem PPY adalah 1.04×10^{-5} S.cm^{-1}. Komposit serbuk menunjukkan kekonduksian dalam julat 1.03×10^{-3} hingga 4.41×10^{-3} S.cm^{-1} dan komposit filem berada dalam julat 4.78×10^{-5} hingga 2.16×10^{-5} S.cm^{-1}. Semua komposit yang dibuat mencapai kekonduksian yang lebih tinggi, rintangan yang dikurangkan, berbanding dengan PPY tulen. Sifat elektrokimia ini menjanjikan untuk aplikasi masa depan mereka sebagai superkapasitor.

Keywords: superkapasitor, polipirrole, 2,6-piridindikarboksilik asid, sebatian logam, kajian elektrokimia

ACKNOWLEDGEMENTS

First and foremost, I express my deepest gratitude and praises to Allah the Almighty, the Most Gracious and the Most Merciful for blessing me throughout the journey of my life, for providing me with knowledge, provisions, guidance, strength and patience, enabling me to further my studies by pursuing this degree.

I would like to convey my sincerest appreciation and respect to my supervisors; Associate Prof. Dr. Siti Nadiah Abdul Halim and Associate Prof. Dr. H.N.M Ekramul Mahmud for their invaluable time, support and expert guidance as well being a constant inspiration throughout the course of my research work. I express my heartfelt gratitude to Prof. Dr. Siti Rohana Binti Majid and Associate Prof. Dr. Mohd Fakhrul Zamani Bin Abdul Kadir for allowing and assisting me to conduct the electrochemical analysis in their laboratories. I also send my special thanks to Dr. Rozie Binti Sarip for her warm encouragement and kind spirit that motivated me during the beginning of my research.

I humbly acknowledge the Malaysian International Scholarship (MIS) 2022 that I was offered by the Ministry of Higher Education Malaysia during my third semester. I am forever grateful for their financial support that enabled me to extend my study for the completion of my research.

Most importantly, I express my gratitude and love to my dear parents and my little brother for their unconditional support, sacrifices, prayers and for being the driving force of my life.

TABLE OF CONTENTS

CHAPTER 4: RESULTS AND DISCUSSION ……………………………………..43

LIST OF FIGURES

LIST OF TABLES

LIST OF SYMBOLS AND ABBREVIATIONS

PDC : 2,6-pyridinedicarboxylic acid
APS : Ammonium persulfate
ATR : Attenuated total reflection
R_b : Bulk resistance
CdPDC : Cadmium 2,6-pyridinedicarboxylic acid complex
R_{ct} : Charge transfer resistance
Z^* : Complex impedance
CuPDC : Copper 2,6-pyridinedicarboxylic acid complex
CE : Counter electrode
I : Current
CV : Cyclic voltammetry
σ_{dc} : DC conductivity
DTG : Differential thermal analysis
DMSO : Dimethylsulfoxide
Δt : Discharging time
EIS : Electrochemical impedance spectroscopy
EIS : Electronic impedance spectroscopy
E : Energy density
EDX : Energy dispersive X-ray
R_s : Equivalent series resistance
FESEM : Field emission scanning electron microscope
FTIR : Fourier transform infrared
GCD : Galvanostatic charge discharge
GCE : Glassy carbon electrode
GO : Graphene oxide

Z_i	:	Imaginary impedance
ITO	:	Indium tin oxide
MOF	:	Metal organic framework
NMP	:	N-methyl pyrrolidone
p-TSO	:	*Para*-toluenesulfonate
PPY	:	Polypyrrole
PPY-CdPDC	:	Polypyrrole cadmium 2,6-pyridinedicarboxylic acid composite
PPY-CuPDC	:	Polypyrrole copper 2,6-pyridinedicarboxylic acid composite
PPY-AgPDC	:	Polypyrrole silver 2,6-pyridinedicarboxylic acid composite
PPY-ZnPDC	:	Polypyrrole zinc 2,6-pyridinedicarboxylic acid composite
PVDF	:	Polyvinylidene fluoride
PXRD	:	Powder X-ray diffraction
P	:	Power density
Z_r	:	Real impedance
RE	:	Reference electrode
SCE	:	Saturated calomel electrode
AgPDC	:	Silver 2,6-pyridinedicarboxylic acid complex
C_s	:	Specific capacitance
SD	:	Standard deviation
TGA	:	Thermogravimetric analysis
WE	:	Working electrode
V	:	Working potential window
XRD	:	X-ray diffraction
ZnPDC	:	Zinc 2,6-pyridinedicarboxylic acid complex

LIST OF APPENDICES

CHAPTER 1: INTRODUCTION

1.1 Overview of coordination compounds

The design and development of coordination compounds based on various transition metals and organic bridging ligands has gained significant attention over the years owing to their interesting structural diversity and novel topologies. Many new forms of coordination compounds have emerged which has consequently led researchers explore their potential applications in fields such as catalysis (Malinowski et al., 2020; Glaser & Wenger, 2020), gas storage and separation (Fan et al., 2021; Tsivadze et al., 2019), chemical sensing (Liu et al., 2020), drug delivery (Mallakpour et al., 2022; Krasnovskaya et al., 2020) and energy storage (Zhang et al., 2019; Chuhadiya et al., 2021).

Coordination compounds include metal complexes, metal organic frameworks (MOFs), coordination polymers and nanoparticles. In the synthesis of coordination compounds, the use of multifunctional ligands comprising of both carboxylic acids and N-hetero aromatic groups (*e.g.* pyridine, pyrazole, pyrazine) has revealed to be excellent building blocks to create polymeric structures and bring rigidity to the complexes (Hassanpoor et al., 2018; Murinzi et al., 2017). The carboxylic groups possess flexible chelating behaviour and because of its numerous possible binding modes, it enables to generate a diverse range of coordination compounds. In the class of pyridinedicarboxylate ligands, N,O-donors are the representative hybrid spacers of the positional isomers of the anions (see **Figure 1.1**) and they are applied to produce varied coordination structures including complexes, coordination polymers and MOFs in a supramolecular arrangement (Scaldini et al., 2014).

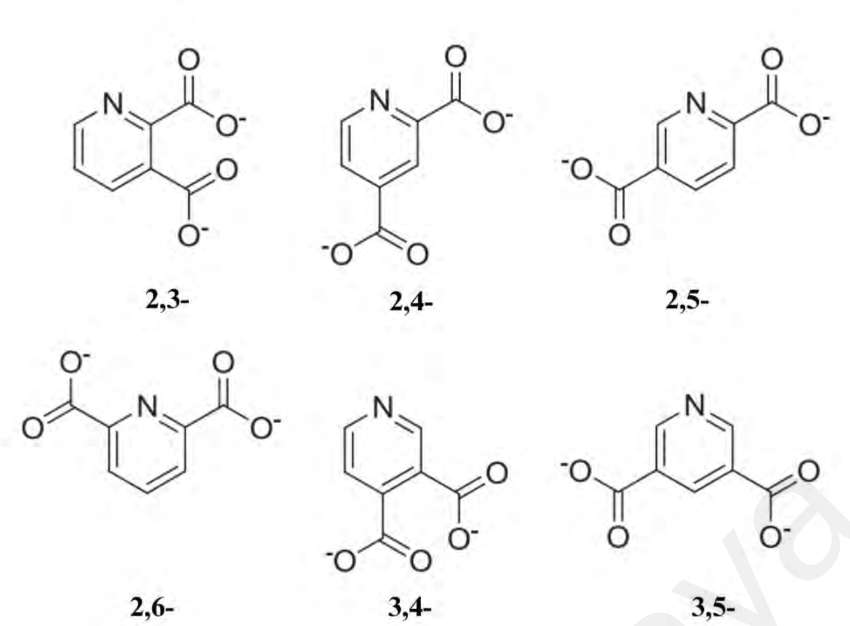

Figure 1.1: Positional isomers of pyridinedicarboxylate anions (Image taken from Scaldini et al., 2014).

Dipicolinic acid or 2,6-pyridinedicarboxylic acid (PDC) is a ligand that is suitable for designing coordination compounds because it serves as a versatile chelating agent with limited steric hindrance and induces self-assembly processes depending on reaction conditions (Derikvand et al., 2012). Its multiple binding modes arise from its two carboxyl functional groups and pyridine nitrogen centre as shown in **Figure 1.2** below. PDC is a natural product that was first discovered in bacterial spores (Bach et al., 1966). It is known for its low toxicity, corrosion inhibition property, cost effectiveness, solubility and amphophilic nature meaning that it can be stained with either an acidic or basic dye. These attributes make PDC favourable for modelling various pharmacologically active compounds (Gonzalez-Baró et al., 2005; Norkus et al., 2003; Heidari et al., 2022) and as catalysts (Du et al., 2021; Zhang et al., 2020).

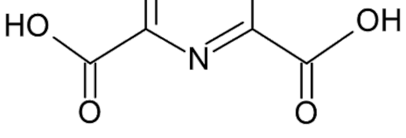

Figure 1.2: Chemical structure of PDC.

Hassanpoor et al. (2018) obtained 1253 examples of coordination compounds with PDC ligands in the Cambridge Structural Database (CSD ver. 5.38 update Feb 2017). Their studies compiled an astonishing 66 different binding modes of the ligand with an abundance of first row transition metal coordination compounds (Cr, Fe, Co, Ni, Cu and Zn). Evidently, the report shows a growing interest and potential in designing and forming new coordination compounds with the organic ligand. Existing PDC based complexes as well as compounds associated with co-ligands have comprehensively studied on their crystallinity for diverse applications in areas of biological and biochemistry owing to its good stability and biocompatibility (Tığ et al., 2017). The carboxyl groups of PDC can combine to form polymeric chains under suitable reaction conditions with the potential influence of N atom from the pyridine ring on the coordination mode, whereby it develops an electron transport feature. Studies have effectively proven that PDC is an electrochemically active and easily infusible compound.

1.2 Coordination compounds-based composite materials

Combination of two or more constituent materials possessing different physical and chemical traits produces a composite material that has enhanced properties which are otherwise not attainable by the individual components. Coordination compounds not only facilitate the transport of charged species in electrolyte, but also shortens the ion diffusion path in its solid-state phase as a result of the morphological changes it brings in the composites by their structural architectures (Tang et al., 2018). Hence, composite formation helps in improving the properties of individual components to induce synergistic effects on its overall performance. Composite materials are used in a wide range of applications and are tailored based on desirable properties. These compounds have gained attention in the development of solar cells, rechargeable batteries, electronic and electrochemical sensors, supercapacitors and fuel cells. Compounds such as MOFs are among the popular active materials of composites studied for high performance supercapacitors displaying superior cyclic stability, high capacitance and high power density (Sundriyal et al., 2018). PDC based compounds and derivatives have been also been used in various composites for their corrosion inhibition in alloys (Chen et al., 2020), in anti-counterfeiting and flexible composite material for LED chips (Yong Jung & Soo Yi et al., 2021), phase change composite material for thermal management of batteries (Ma et al., 2023) and electrochemical sensor for detecting uric acid (Cui et al., 2021). The favourable qualities of polymeric PDC are also rendered useful for energy storage applications as they can add new properties to conducting polymer electrodes as composite materials that increases its capacitance or charge storing ability (Arvas et al., 2022).

1.3 Energy storage device and supercapacitor applications

To address the issues concerned with the consumption of conventional energy resources and climate change repercussions, the development of new and sustainable modes of energy storage technologies has received considerable attention in research (Yang et al., 2013; Dubal et al., 2015; Xuan et al., 2015; Gopi et al., 2020; Saikiya et al., 2021). This encompasses the shift towards renewable sources of energy and optimization of the techniques associated with efficient energy storge and conversion systems. As our reliance on electronics continues to grow, there is an increasing need for clean, high-performance, and cost-effective lightweight energy storage devices (Choudhary et al., 2021). Among the available storage systems applicable to electrical power sources, electrochemical energy storage modes like rechargeable batteries and supercapacitors have been the subject of extensive research for the past decades (Tang et al., 2017) involving thoughtful design strategies aimed at fulfilling this demand.

Commercially available rechargeable batteries like lead-acid batteries, lithium-ion batteries have widespread small to large scale applications in smart phones, hybrid electric vehicles, medical devices owning to its high energy storage ability and energy density (≈200 $\mathrm{Wh.kg^{-1}}$). However, it also possesses few drawbacks such as low power density (≤1 $\mathrm{kW.kg^{-1}}$), long charge/discharge times, short cycle lives, environmental and thermal safety issues (Huang et al., 2022; Olabi et al., 2022). In comparison, supercapacitors offer higher power density delivery (10 $\mathrm{kW.kg^{-1}}$), faster charge/discharge time within seconds, exceptionally longer cycle lives (>100,000), extensive operational temperature range, mechanical flexibility and environmental sustainability (Muhamad et al., 2017; Sharma et al., 2020). Hence supercapacitors are regarded as highly promising and potential candidates for energy storage applications.

The selection of electrode material plays a pivotal role in determining an energy storage device's performance. Current trend in research revolves around broadening the range of materials used in designing supercapacitors. This expansion includes diversifying the materials employed for inorganic supercapacitor electrodes, which typically involves substances such as activated carbon, transition metal oxides, conductive polymers, and various other conductive inorganic materials. Ever since the development of conducting polymers through the pioneering joint research work that earned the researchers their Nobel Prize in Chemistry for the year 2000, there has been a remarkable progress in the study for new and innovative design strategies for energy storage devices with different conducting polymer derivative hybrid nanocomposites as modified electrode materials (Shimoga et al., 2021; Fleischmann et al., 2020). Conducting polymers are organic polymers that differ from conventional polymers by possessing conjugated bonds which allows it to have optoelectrical properties similar to inorganic semiconductors. The presence of a conjugated system offers free movement of delocalized π electrons within the polymer structure hence it constructs pathways for charge transport (Nezakati et al., 2018). Not only these materials possess extensive range of electrical conductivity but also offer flexible tuning of its conductivity by preparing their composites or by doping. Besides that, owing to their simple and cost-effective approaches, low density and corrosion resistance, there have been major advances in studies for energy storage, sensors, flexible electronics and biomedical applications (Tang et al., 2017; Yussef et al., 2018). Popularly used conducting polymers include polypyrrole, polyacetylene, polyaniline, polythiophene and their derivatives.

Polypyrrole (PPY) is a five membered heterocyclic conjugated polymer known to have good conductivity, low cost, facile synthesis, controllable dielectric loss ability and good environmental stability (Wang et al., 2015). **Figure 1.3** shows the chemical structure of PPY**.** PPY and its derivatives are one of the most studied modified electrode materials for supercapacitors owing to their ease of tuneability and synergistic properties with other electroactive compounds including rapid charge/discharge rate, high energy density and high thermal stability (Kim et al., 2016). Despite such good qualities, pristine PPY-based supercapacitors typically possess low conductivity, poor mechanical strength and poor cycling stability which eventually results in structural collapse from swelling and shrinking of the polymer chains by prolonged charge/discharge processes (Muhamad et al., 2017). Therefore, to tackle this issue PPY has been incorporated with different metal hybrid architectures, counter ions and dopants creating nanocomposites of varied morphologies and their studies have shown significant improvement of electrochemical performance (Wang et al., 2020) upon fabrication as high-performance electrode material for supercapacitor application (Shimoga et al., 2021), flexible electronics and electrochemical biosensors (Choudhary et al., 2021).

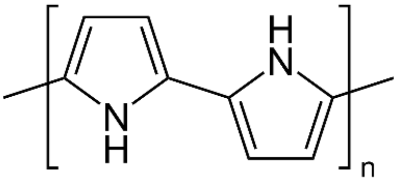

Figure 1.3: Chemical structure of PPY.

To compensate for the shortcomings of pristine PPY for supercapacitor electrodes it is therefore, important to investigate the potential of various metal-coordinated PDC complexes with PPY as these complexes can bring interesting structure and morphology to the electrode materials which might influence to the mechanical stability, surface area, capacitance, conductivity and the electrochemical performance of supercapacitors.

1.4 Research problem

In order to meet the rapidly increasing global demand of energy, it is crucial to develop environmental-friendly, high-performance energy storage materials. Constructing an electrode by judicious fabrication of different materials for energy storage devices like supercapacitors is essential to facilitate the electrochemical kinetics process and capacitive properties (Wang et al., 2021). Hence there have been many successful efforts in fabricating new and enhanced supercapacitor electrodes for flexible electronics with a facile and low-cost synthesis having the ease of reproducibility and stability (Wang et al., 2020; Fan et al., 2022; Shimoga et al., 2021). One of the challenges that arises for supercapacitor application is the incorporation of easy methods to prepare an electrode material with strong electrochemical performance and efficiency (Guo et al., 2020). Another challenge remains is to develop these high-performance electrode materials with reduced material cost that could hinder the reproducibility and large-scale application of the devices (Guan et al., 2017; Parnell et al., 2019; Sriram et al., 2023).

PPY and its composites are one of the most popularly studied conducting polymers as supercapacitor materials because of its electronic properties, biocompatibility, ease of fabrication and tunability with other compounds as well as good electric and thermal stability (Zayan et al., 2020). There are many PDC based complexes with transition metals reported focusing on their crystallographic studies (Etaiw & El-Bendary, 2019; Kremer & Englert, 2019) and biological activities (Zang et al.,2015; Li et al., 2020). However, to the best of current knowledge their studies as electrode material for energy storage have not been extensively explored yet. A study of polymeric PDC with PPY has been investigated which revealed interesting structural properties that lead to increased specific capacity of 854.2 $F.g^{-1}$ at 2.7 $A.g^{-1}$ with a high energy density of 884.4 $Wh.kg^{-1}$ (Arvas et al., 2022). A systematic review of reported metal-based PPY nanocomposites concerning supercapacitor applications showed noteworthy results both on the physio-chemical properties and electrochemical properties caused by synergistic effect of individual components (Shimoga et al, 2021). Likewise, multiple studies have proven that the introduction of metal coordination structures could improve the electrochemical stability of the composites by mediating effective charge transfer through PPY (Xie et al., 2019; Gan et al., 2015).

It is therefore necessary to develop new composite materials fabricated with PPY and PDC based complexes of transition metals offering better electrical conductivity and capacitance considering the advantages of cost-effectiveness, simple preparation methods and biocompatibility of the constituent materials.

1.5 Research objectives

(i) To synthesize and characterize PDC-based metal complexes of Ag, Cd, Cu and Zn via self-assembly at ambient conditions.

(ii) To synthesize and characterize PPY with the obtained PDC-based metal complexes creating composites as powder and films by *in situ* oxidative and electrochemical polymerization processes, respectively.

(iii) To determine the electrochemical behaviour by CV and EIS of the composite powder and films.

1.6 Dissertation outline

This dissertation is divided into five chapters. Chapter 1 begins with the overview of coordination compounds and their composite materials, current trend of energy storage devices and supercapacitors followed by the research problem, objectives and dissertation outline.

Chapter 2 consists of literature review which provides more background of coordination compounds and their advantages for supercapacitor application, supercapacitor and its types, electrochemical parameters, charge transfer mechanism of PPY, comparison of findings with previous reported electrochemical studies of PDC based complexes and metal hybrid-PPY composites as electrode materials.

Chapter 3 consists of the experimental process of synthesizing PDC complexes and its PPY composites. The characterization parameters as well as the electrode preparation are also presented in detail.

Chapter 4 comprises the results and discussion of the research. The characterization of the PDC complexes and its PPY composites as powder and film are discussed in detail. The CV of the powder composites was done as slurry coated over graphite sheets and the film composites was done over ITO glass both in a similar three-electrode cell set up. The CV and EIS responses of PPY/metal-PDC composites are presented with comparison to the pure PPY.

Chapter 5 summarizes and concludes the dissertation by fulfilling the research objectives and some suggestion for future work.

CHAPTER 2: LITERATURE REVIEW

2.1 Overview of coordination compounds

A coordination compound is a neutral complex or an ionic compound having a central metal atom or ion (Lewis acid, electron acceptor) surrounded by a set of ligands (Lewis bases, electron donors) which are joined by coordinate bonds. A wide range of metals can form coordination compounds, and some of the most commonly involved metals include transition and main group metals. These metals exhibit variable oxidation states, making them suitable for forming coordination complexes with different ligands. Transition metals, in particular, are known for their ability to form colourful complexes due to the presence of d-electron transitions. Additionally, many other metals and metalloids can also participate in coordination chemistry, depending on the specific ligands and conditions.

Ligands in coordination compounds are molecules or ions that can donate electron pairs to a central metal atom or ion. They form coordinate bonds with the metal, resulting in the formation of a complex. Ligands can be classified based on their charge and the number of lone pairs of electrons they can donate. These ligands contribute to the stability and diverse properties of coordination compounds. Besides, it can also influence the reactivity and applications of the resulting complexes (Weller et al., 2014).

Coordination compounds have definite geometries around the central metal atom or ion. Square planar, tetrahedral and octahedral geometries are among the most common structures of coordination compounds. These can be obtained by varying the choice of ligands which then can lead to different types of coordination compounds including coordination polymer and metal-organic frameworks. The term ‘coordination polymer’ is used to describe the extended networks or infinite array of repeating coordination units creating solid state structures in at least one dimension (Batten et al., 2012). When the crystalline coordination network of metals and polydentate organic ligands extend in 2D or 3D under suitable reaction conditions, the class of materials are commonly termed as MOFs. MOFs are characteristically porous coordination polymers having flexible tailorability compared to traditional porous materials like zeolites and activated carbons (Jiao et al., 2019). Common ligands used for the synthesis of MOFs using various metals include 1,4-benzenedicarboxylic acid (Villarroel-Rocha et al., 2022; Winarta et al., 2019), benzene-1,3,5-tricarboxylic acid (Roy et al., 2023; Manyani et al., 2023), 4,4-biphenyldicarboxylic acid (Decker et al., 2020), imidazoles (Kouser et al., 2022) etc.

2.2 Advantages of coordination compounds for supercapacitor applications

Lately, there has been a growing research interest in advanced nanocomposite materials derived from transition metal-based coordination compounds with tailored composition and structures for electrochemical energy storage and conversion systems such as Li-ion batteries, supercapacitors and fuel cells (Guan et al., 2017; Srivastav et al., 2019; Wen et al., 2020). Compared to conventional inorganic and polymeric functional materials, coordination compounds take the advantages of the electrochemically active metal centres and organic functional groups, fully accessible coordination sites and interesting morphological architectures by synthetic conditions with additional active components (Wu et al., 2017). MOFs related functional materials are popularly studied for energy storage application because of their flexible post-synthetic modifications, high surface area and tunable porosity. High surface area in an electrode material provides abundant electrochemical active sites for enabling charge storage processes such as adsorption/desorption and surface redox reactions. Porous structures are ideal for accommodating guest electrolyte species and facilitating mass transport (Guan et al., 2017). Since the morphology and structure of an electrode material greatly influences the surface-related processes in the accessible areas, structural stability and providing diffusion pathways for electrolyte ions, it ultimately determines the electrochemical performance of the device.

2.3 Supercapacitors

Supercapacitors are electrochemical energy storage devices whose charge storage process is similar to that of rechargeable batteries. The components that comprise a supercapacitor device are two electrodes, metallic current collectors, electrolyte and a separator. Supercapacitors have two distinct assembly structures which are two-electrode cell and three-electrode cell. While the two-electrode cells are used for both research and commercial purposes, the three-electrode cells have an additional reference electrode and are utilized mainly for research studies that require high precision in measurements (Olabi et al., 2022).

Compiled in **Table 2.1** is a brief list of characteristics of various electrochemical storage devices. Specific power (W.kg^{-1}) or power density and specific energy (Wh.kg^{-1}) or energy density are the two important parameters which indicates the performance comparison of a storage device. Energy density refers to the amount of energy accumulated in an electrode material per unit volume and power density reveals the conversion rate of that accumulated energy. The higher the energy density is of a system, the greater is its ability to store energy (Mulik et al., 2022). From the Ragone plot of **Figure 2.1**, batteries show higher specific energy compared to others, whereas conventional capacitors have higher power density. Ideally, the target for most applications is to possess a storage device with both the power density and specific energy. Supercapacitors and associated hybrid storage systems exhibit a linear increase in energy storage and release capacity by several orders of magnitude, bridging the gap between conventional dielectric capacitors and batteries. For applications requiring high energy release in a short span of time, supercapacitors are replacing batteries in terms of power and capacitors in terms of energy owing to their larger advantages over both the storage systems (Meng et al., 2017; Sarno et al., 2020). Currently supercapacitors have diverse applications in portable electronics, light rail, electric and hybrid automobiles, industrial equipment, power grids, power backup and storing the regenerative braking energy of electric vehicles (Choudhary et al., 2021; Huang et al., 2022).

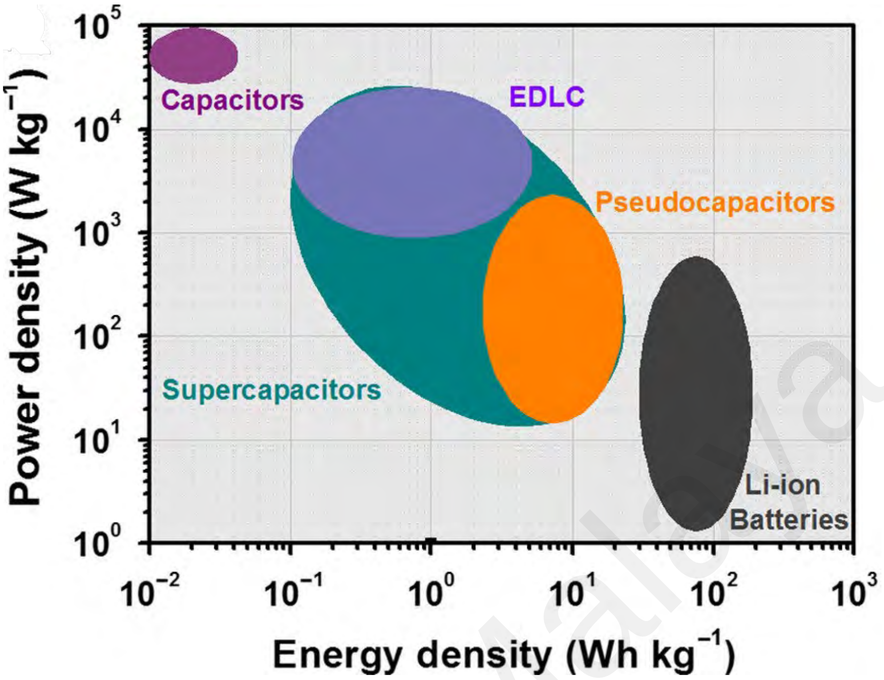

Figure 2.1: Ragone plot showing the energy and power relationship of various energy storage systems (Image taken from Jiang & Liu, 2019).

The performance of a supercapacitor is mainly governed by the electrode material and its charge storage process mechanism (Sharma & Kumar, 2020). Hence, ongoing research in the field of electrochemical storages has been dedicated to the design, introduction and fabrication of new composite materials for electrodes that can provide a stable and reliable supply of energy (Noori et al., 2019). An ideal electrode material for supercapacitor should be inexpensive, corrosion resistant, provide high electrical conductivity, chemical and thermal stability, ease of morphology manipulation and higher capacitance arising from its larger surface area (Forounzandeh et al., 2020; Yu et al., 2015). Carbon based materials (*e.g.* graphene, activated carbon, carbon nanotubes), metal oxides (*e.g.* RuO_2, IrO_2, MnO_2) and conducting polymers (*e.g.* PPY, polyaniline, polythiophene) are the majorly studied electrode materials for energy storage devices.

Table 2.1: Characteristic properties of different energy storage devices (Adapted with modification from Noori et al., 2019)

Characteristics	**Capacitor**	**Supercapacitor**		**Battery**
		EDLC	**Pseudocapacitor**	
Nature of charge storage	Physical	Physical Reversible ion adsorption	Physio-chemical Redox reaction, intercalation, doping or underpotential deposition	Chemical Redox reaction, Intercalation/deintercalation or change in oxidation state
Cycle life	Almost infinite	> 10,00,000	> 100,000	150 – 1500
Cycle life limitation	None	None	Decomposition and degradation of active material at high over-potentials	Loss of mechanical stability and chemical reversibility of reactions, degradation of active materials at high over-potentials
Energy density	Very low	Low	Moderate	Very high
Power density	Very high	High	High	Low to moderate
Self-discharge	High	High	Moderate	Very low
Storage mechanism	Non-faradaic process	Non-faradaic process	Faradaic process	Non-faradaic process
Materials	Metals (*e.g.* aluminium, tantalum, niobium)	Carbon based materials (*e.g.* porous carbon, graphene, CNT)	Conducting polymers (e.g. PPY, PANI), metal oxides/ hydrides/ sulfides (*e.g.* MnO_2, Co_3O_4, RuO_2, V_2O_5), Metal organic frameworks (*e.g.* $Ni_3(HITP)_2$, ZIF-67)	High theoretical capacity materials (*e.g.* $LiMnPO_4$, $LiCoO_2$)
Environmental impact	Very low	Very low	Low	Medium to high

2.4 Types of supercapacitors

Supercapacitors are divided into two major categories based on their material composition and charge storage mechanisms: electric double layer capacitor (EDLC) and pseudocapacitor. **Figure 2.2** illustrates the two types of supercapacitors.

EDLC stores charge electrostatically by the absorption and desorption of electrolyte ions at the electrode-electrolyte interface. Upon applying voltage, the charge carriers of the ion-containing electrolyte migrate towards the oppositely charged electrode forming a double layer and the EDLC gets charged. Conversely in the discharging process, the ions get repelled. EDLCs can have quite longer cycle life (> 10,00,00) due to the double layer charge storage in the absence of any chemical change of active materials during the charge/discharge process. The electrodes are based on carbon materials e.g. activated carbon, porous carbon and graphene (Noori et al., 2019; Sharma & Kumar, 2020).

Pseudocapacitor stores electric charge by reversible faradaic reactions that involves charge transfer of redox active materials at the electrode-electrolyte interface. The electrodes are typically metal oxides/hydroxides (*e.g.* MnO_2, CoO_x, NiO, Fe_2O_3) and conducting polymers (*e.g.* PPY) (Chen, 2013; Arunkumar Paul, 2017; Yu et al., 2015). They are proven to have greater electrochemical storage capacity and energy density than EDLCs. In the field of flexible and portable electronics, pseudocapacitor materials fabricated with conducting polymers and metallic nanostructures are currently gaining attention as promising components to facilitate efficient capacitance (Shimoga et al., 2021).

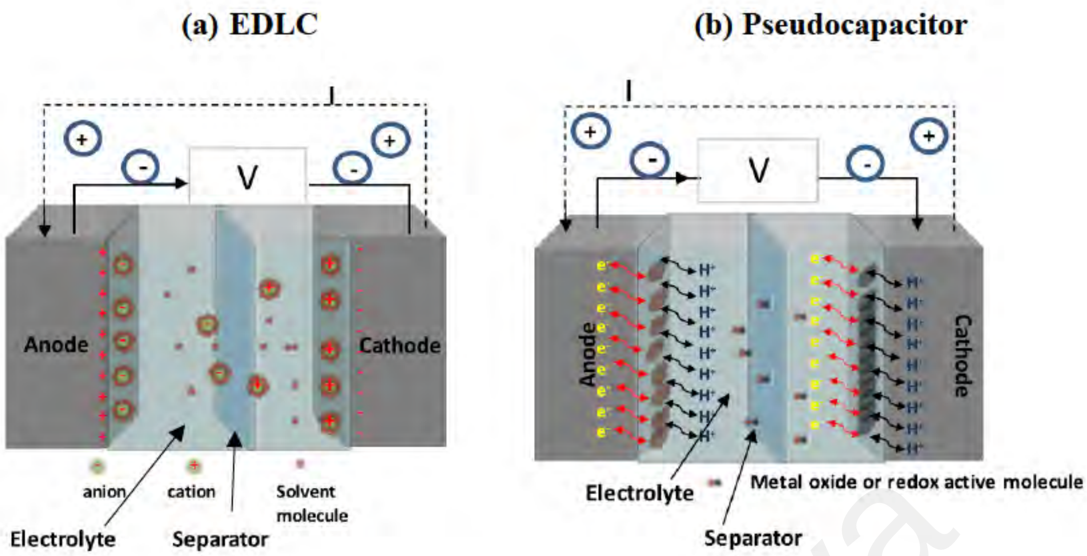

Figure 2.2: Schematic illustration of two types of supercapacitors (a) EDLC and (b) Pseudocapacitor (Image taken from Sarno, 2020).

As research progresses with the incorporation of new materials for electrodes for attaining better capacitance, a third category of supercapacitor have emerged which exhibit both faradaic and non-faradaic processes. This type of supercapacitor is called hybrids and they are made of irregular electrodes (Sharma & Kumar, 2020). For example, a hybrid supercapacitor cell was built with faradaic or pseudocapacitive type material (*e.g.* Co_3O_4, $Ni(OH)_2$) and a non-faradaic or EDLC type material (*e.g.* activated carbon) (Hao et al., 2018; Ensafi et al., 2018).

2.5 Electrochemical parameters of supercapacitors

Cyclic voltammetry (CV), galvanostatic charge-discharge (GCD) and electrochemical impedance spectroscopy (EIS) tests are usually performed to evaluate the electrochemical performance of an electrode active material. Various parameters such as specific capacitance, cycling stability, power density, energy density and charge-discharge rates are considered for energy storage studies.

CV curves are plotted against applied potential (V) vs. corresponding response current (I) The shape of CV curves is generally characteristic to each kind of energy storage system as represented in **Figure 2.3**. For ideal supercapacitors, the CV curves are rectangular however for real supercapacitors deviations may occur due to redox reactions at the interface. The position of redox peaks is useful for determining the type of redox reactions occurring in the system. The shape of CV curves is hence very useful for identifying the electrode material as battery-type or capacitor-type. Battery-type materials exhibit intense and clearly separated redox peaks in CV and plateaus in GCD curves. Whereas EDLC materials exhibit a nearly rectangular CV curves and a very linear voltage response in GCD measurements. Pseudocapacitive materials takes on a quasi-rectangular CV shape and an analogous triangular plateau in GCD. Meanwhile, the CV curves of a hybrid supercapacitor resembles both EDLC and pseudocapacitor (Huang et al., 2022).

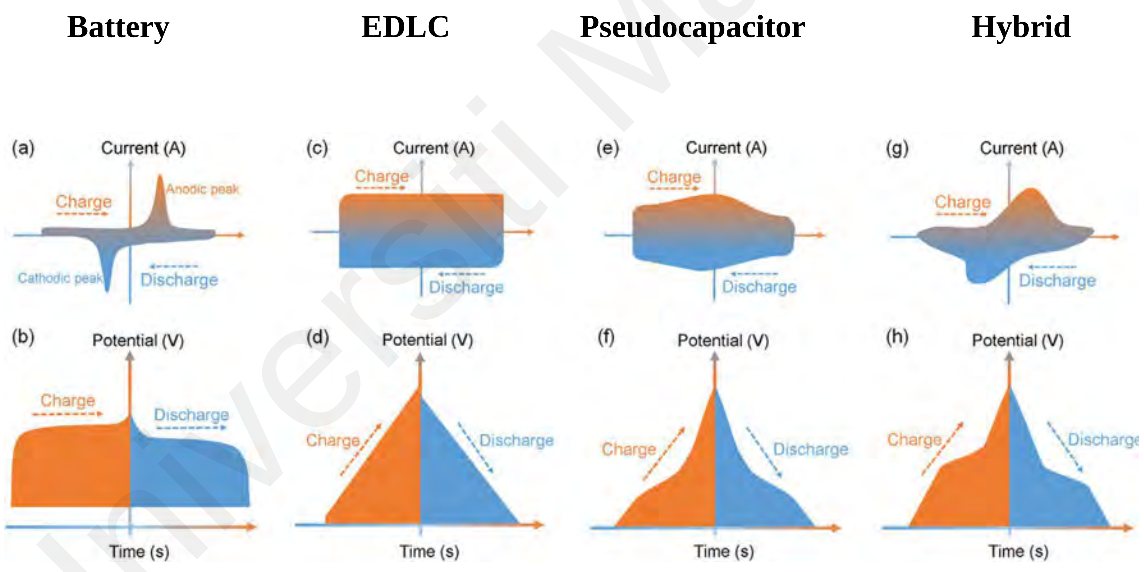
Battery **EDLC** **Pseudocapacitor** **Hybrid**

Figure 2.3: Comparison of the electrochemical behaviour of a typical battery and supercapacitor. CV and GCD curves of (a,b) battery and supercapacitor: (c,d) EDLC; (e,f) pseudocapacitor; (g,h) hybrid (Image taken from Huang et al., 2022).

Specific capacitance (C_s) measures the ability of a supercapacitor to store electrical charge per mass of the active material (F g^{-1}). The specific capacitance can be calculated from GCD measurements using **Eq. [2.1]:**

$$C_s = \frac{I \times \Delta t}{m \times \mathrm{V}} \quad [2.1]$$

where, C_s = specific capacitance (F.g^{-1}), I/m (A.g^{-1}) is the applied current density, Δt (s) is the discharging time, V (V) is the working potential window to discharge the cell (Sethi et al., 2020).

The energy and power density can be subsequently determined from the generally used formulas **Eq. [2.2]** and **Eq. [2.3]** respectively:

$$E = \frac{1}{2} \times C_s \times V^2 \quad [2.2]$$

$$P = \frac{V^2}{4mR_s} \quad [2.3]$$

where E is the energy density (Wh.kg^{-1}), P is the power density (W.kg^{-1}), m is the mass of the electroactive material and R_s is the equivalent series resistance or bulk resistance (Zhang & Pan, 2015).

Impedance studies from EIS can give the information about the electrical conductivity and overall resistance of the materials. By a simple definition, impedance is based on the measurement of current response to an applied potential perturbation in the form of sine wave **(Bardini, 2015).** There are two standard type of plots that are generated from EIS data: Nyquist plot and Bode plot (**Figure 2.4**). Most published EIS data are published by representing it as Nyquist plot.

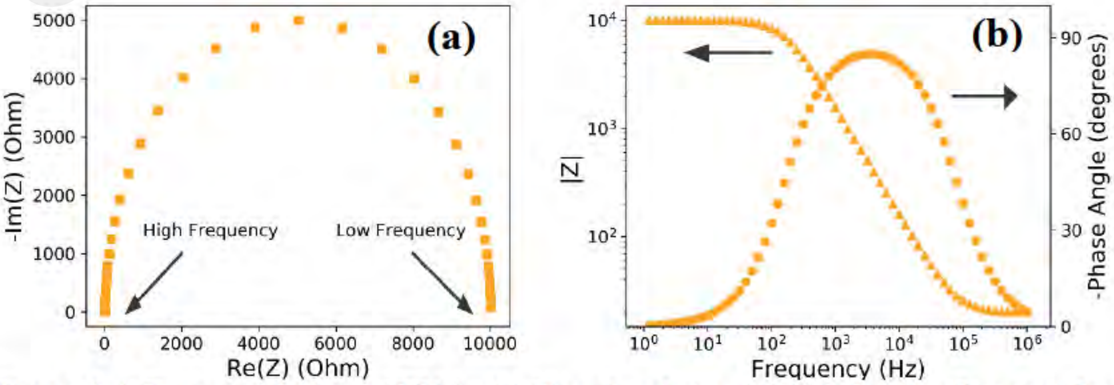

Figure 2.4: Representation of EIS in (a) Nyquist plot and (b) Bode plot (Image taken from Bardini, 2015).

The Nyquist plots can also help to describe the electrochemical system by constructing the equivalent circuit diagram of the device simulated by a software (**Figure 2.5**). The data is plotted with the real (*x* axis) and the imaginary (*y* axis) parts of complex impedance.

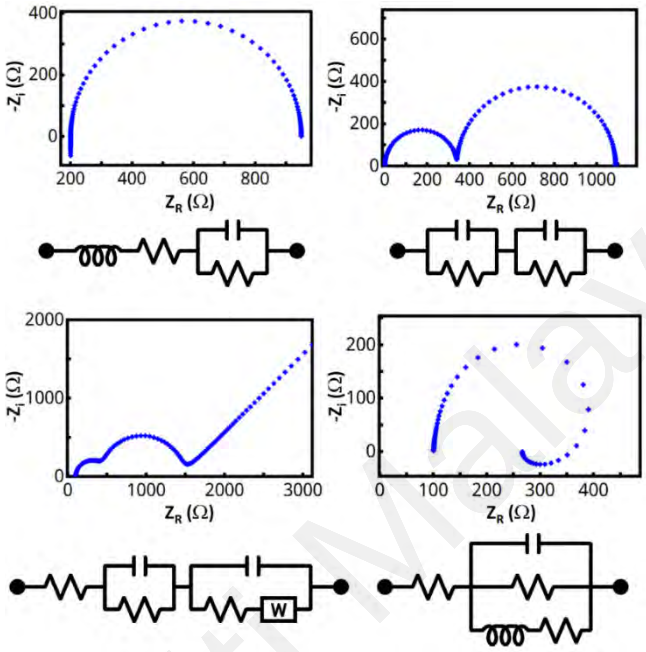

Figure 2.5: Examples of Nyquist plots of different equivalent circuit networks (Image sourced from www.pineresearch.com).

2.6 Charge transfer mechanism of conducting polymers

Conductivity of the conducting polymers arises from two main factors: their conjugated backbone and the presence of a negatively charged dopant molecule (Balint et al., 2014). A conjugated backbone has alternating series of single and double bonds (see **Figure 2.6** and **Figure 2.7**). The overlapping of *p*-orbitals in the π-bonds allow electrons to be easily delocalized and freely move between the atoms, hereby causing the charge transfer in the polymer. The synthesis of a conducting polymer in its neutral state occurs only in the presence of a dopant molecule. A dopant introduces a charge carrier into the polymer chain by protonation/deprotonation and relocalize them as polarons or bipolarons. As electric potential is applied, the dopants move in/out of the polymer, disrupting the stable neutral state and allow charge transfer in the form of polarons or bipolarons.

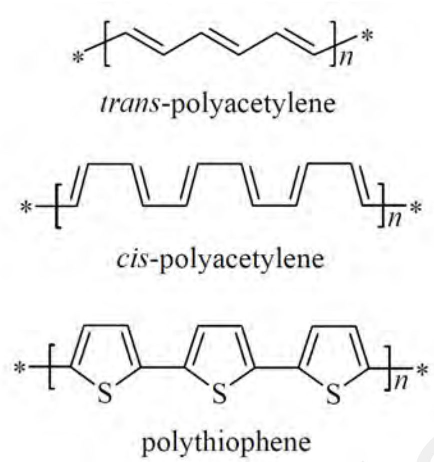

Figure 2.6: Examples of conducting polymer structures (Image taken from Ateh et al., 2006).

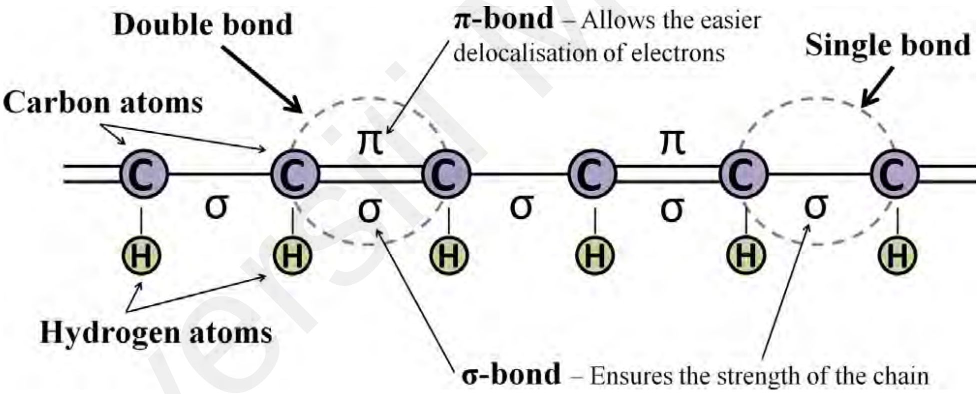

Figure 2.7: Schematic of a conjugated backbone: a conducting polymer chain containing alternating single and double bonds (Image taken from Balint et al., 2014).

The electrical conductivity of PPY is influenced by its doping level, the degree of disorder, synthesis method and conditions (Ghanbari et al., 2018). **Figure 2.8** depicts the charge transfer mechanism of PPY. Specifically, the conductivity of PPY arises from the movement of bipolarons and the inter-chain hopping of anions/cations within the material (Ateh et al., 2006; Balint et al., 2014). Since the physio/chemical and electrical properties are controllable with the ease of synthesis, PPY is highly ideal than other conducting polymers for energy storage applications (Shimoga et al., 2021).

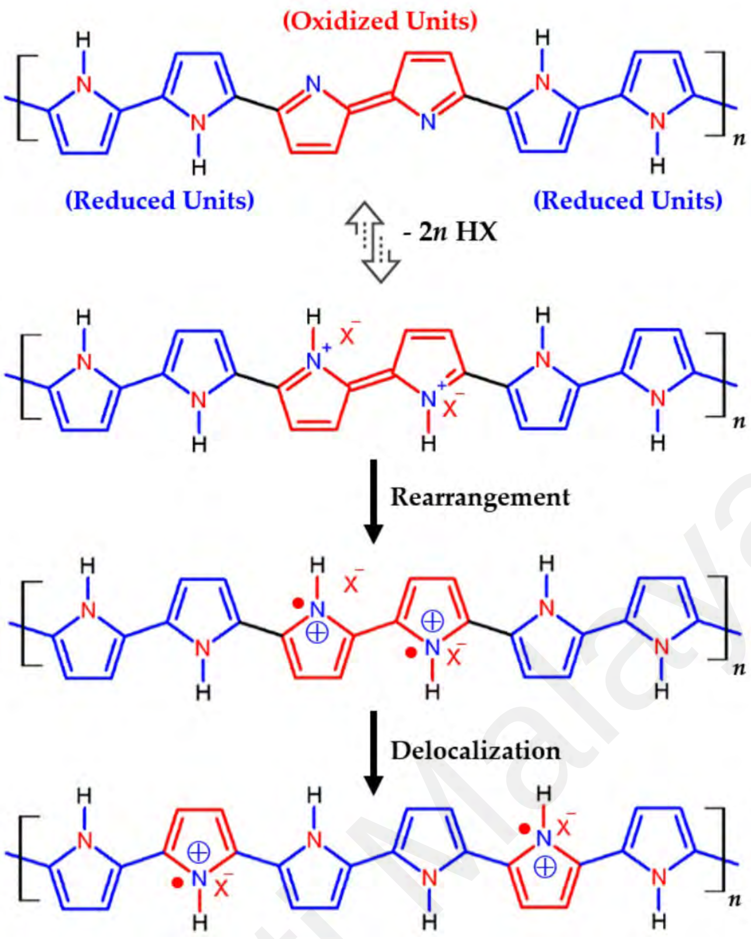

Figure 2.8: Charge transfer mechanism of PPY (Image taken from Shimoga et al, 2021).

2.7 Synthesis methods of PPY

PPY is commonly synthesized by two main methods: electrochemical polymerization of pyrrole monomer using dopants and chemical oxidation using strong oxidizing agents (Ateh et al., 2006; Kim et al., 2016). Chemical oxidative polymerization is a simple popular method for fast fabrication of the polymer to produce bulk quantities in the form of powder, dispersion and coating. However, the homogeneity of PPY with uniform structure is difficult to obtain by this method. Electrochemical polymerization via chronoamperometry through deposition on electrode surface as films is an ideal method as it allows easier modification of the conducting polymer morphology and its electrochemical properties besides providing high rates of purity and accuracy (Pang et al., 2021). Other desired electrochemically active compounds are usually added together with the monomer during polymerization to fabricate a hybrid composite material. Other synthesis method of PPY involves ultrasonication, vapor phase polymerization, electrospinning, photopolymerization, microemulsion and mechanochemical polymerization. Through different synthesis method, measuring parameters, conditions and instruments (four-point probe, impedance spectroscopy), typical conductivity range of PPY has been reported from 10^{-10}-10^{2} S.cm^{-1} (Stejskal et al., 2016; Kaynak, 2019; Husain et al., 2021).

Figure 2.9 (A) shows the reaction scheme of electropolymerized PPY doped with *p*-TSO. The PPY was deposited as film over the Fe foil electrode. During chronoamperometry when the anodic potential was applied to the Fe foil working electrode, the electrons left the electrode and formed C-N^{+} radical within the pyrrole monomer ring. The chain propagation was continued afterwards by oxidation, coupling and deprotonation until PPY was formed. Meanwhile, to compensate the charge imbalance at the working electrode, TSO^{-} from the electrolyte is expected to penetrate into the polymer forming a neutral PPY film as the final product (Liao et al., 2017).

Figure 2.9 (B) shows the proposed reaction scheme of PPY obtained by chemical oxidation using $(NH_4)_2S_2O_8$ in aqueous solvent. The mechanism is quite similar to that of the electrochemical polymerization and is generally widely accepted (Tan & Ghandi, 2013). In this case, the oxidant causes the loss of one electron of pyrrole, creating a radical cation. Then, coupling of the two pyrrole radical cations form 2,2′-bipyrrole with deprotonation. The chain propagation is subsequently carried on with other oxidized segments. During propagation, re-oxidation, coupling and deprotonation occurs till the final PPY is formed in neutral state as fine black powder (Wang, 2016).

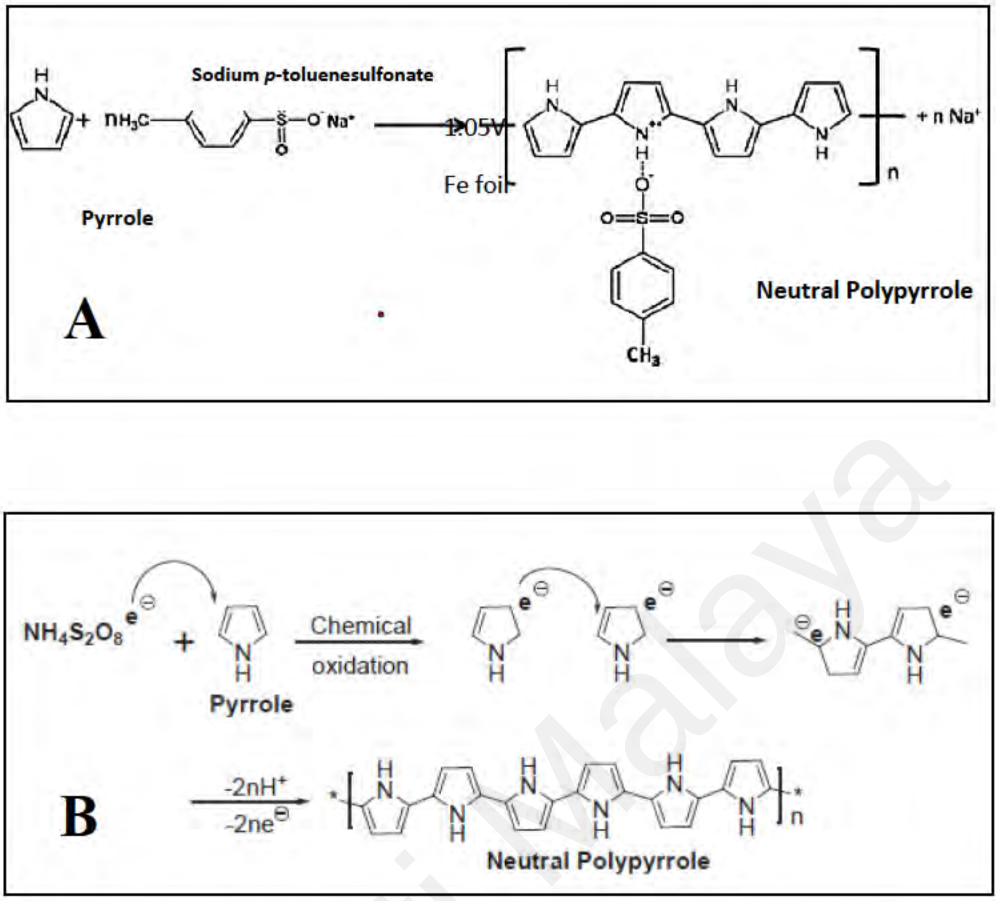

Figure 2.9: Scheme of two different polymerization methods of pyrrole (A) electrodeposition of PPY doped with *p*-TSO on Fe foil via chronoamperometry at 1.05 V with saturated calomel electrode (SCE) as reference and Pt foil as counter electrode (Image taken from Liao et al., 2017); (B) chemical oxidation of pyrrole to PPY with ammonium persulfate as oxidizing agent (Image taken from Wang et al., 2015).

2.8 Reported electrochemical studies of PDC based compounds

PDC as electropolymerized film [P(PDC)] has been known for its electroanalysis application as biosensors when integrated with variety of immobilized biomolecules benefitting from its rich electroactive centre. The initial discovery of P(PDC) film having good affinity with nano-gold coated electrode for enzymatic sensors (Ciao et al., 2007) garnered attention on its electrochemical studies by modifying it for sensing other biologically active molecules. Nano-gold was modified on P(PDC) film over glassy carbon electrode (GCE) via electrodeposition and a DNA probe was immobilized on the modified electrode via adsorption/immersion to construct a DNA biosensor for the detection of PAT gene fragment found in transgenic plants (Yang et al., 2007) and for the determination of anticancer drug gemcitabine (Tığ et al., 2016). Nano-gold particles and P(PDC) was also incorporated with graphene oxide-modified GCE which was developed as a novel sensor for electrochemical determination of ascorbic acid, uric acid and dopamine (Tığ et al., 2017). The electrode was seen to exhibit good electrochemical behaviour due to synergistic effects of each of the components making the composite electrode. When modified with ATPS-Fe_3O_4 nanoparticles, P(PDC)/GCE showed enhanced effective surface area for the determination of NADH (nicotinamide adenine dinucleotide) and its antioxidant capacity (Cui et al., 2011). All the four studies as biosensors displayed satisfactory selectivity and notable reproducibility of their respective methods proving the effectiveness of PDC as an electrochemically active, easily infusible compound.

There have been few studies on the electrochemical behaviour of PDC based transition metal complexes for a varied range of applications. Zn(II) complexes with PDC was synthesized using both reflux and non-reflux method in methanol-water solvent media and showed promising results when it was electrochemically tested for toxicity using Brine Shrimp Lethality Test (Martak & Christanti, 2014). Cu(II) PDC complex crystals were synthesized to investigate its bioactivity by interactions with herring sperm DNA (Zang et al., 2015). In most cases the facile synthesis of available PDC based metal complexes were performed at room temperature in water solvent mixed media, making it easier for production on a large-scale basis. For example, crystal structure analysis was done for distorted octahedral complexes of Cu(II) and Zn(II) with PDC obtained by slow evaporation in an ethanol-water solution media (Okabe & Oya, 2000). Good electrical conductivity in the range of 10^{-4} and 10^{-2} $S.cm^{-1}$ measured by four-point probe method of metal-PDC-piperazine based coordination compounds have been reported for two lanthanide metals (La, Nd) when used as insoluble polymer electrolytes, proposed for solid phase semiconducting material applications (Ay et al., 2018).

The shape of the cyclic voltammogram of PDC based compounds so far can be best described as duck shaped with redox peaks when in $K_3[Fe(CN)]_6$ electrolyte (**Figure 2.10**). It can be observed that the electrochemical behaviour by CV of the modified glassy carbon electrode (GCE) whether with composite polymerized PDC [P(PDC)] or as transition metal complex [Co(II)-PDC], there is a good peak potential separation for a reversible system. In both cases, $Fe(CN)_6^{3-/4-}$ was used as a redox probe and its lower values indicate good electron transfer ability (ΔE_p) of the electrodes (Murinzi et al., 2017). **Figure 2.10 (I)b** and **(I)c** shows the immobilization of ATPS-Fe_3O_4 on the modified P(PDC)/GCE decreased the ΔE_p and increased the peak current (I_p), suggesting that the immobilization increased the electron transfer rate between the electrode surface and $Fe(CN)_6^{3-/4-}$ owing to its good conductivity and large surface area of the nanoparticles. The metal-PDC complex as Co(II)-PDC/GCE showed similar lowered ΔE_pvalues when compared to bare GCE in **Figure 2.10 (II)**, indicating good electron transfer ability. It can be inferred that PDC has good electron transfer ability as observed by its CV response whether as a composite polymerized material or simply as a metal complex.

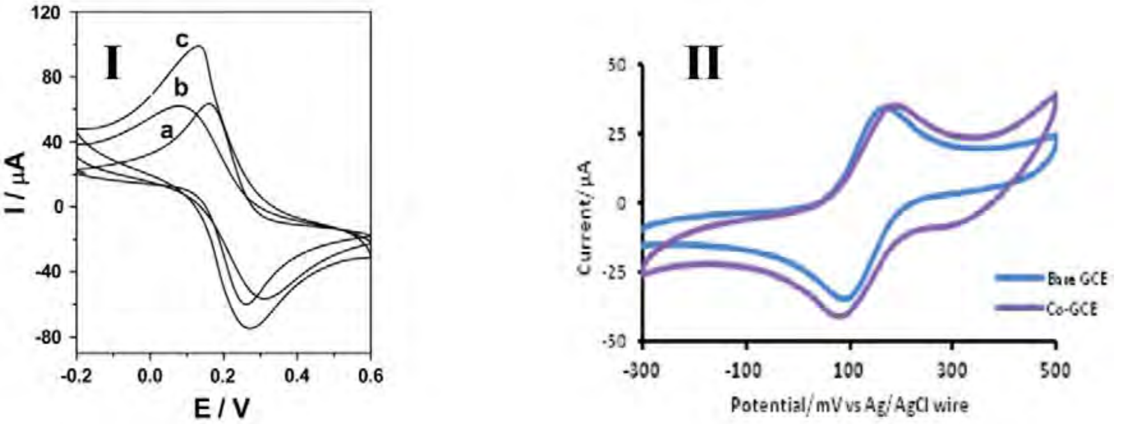

Figure 2.10: CV curves of different electrodes with and without containing PDC compounds at 100 mV.s^{-1} scan rate; (I) In 1:1 solution of 5 mM Fe(CN)$_6$$^{3-/4-}$ and 0.1 M KCl where (a) GCE, (b) P(PDC)/GCE, (c) ATPS-Fe$_3$O$_4$/P(PDC)/GCE (Image taken from Cui et al., 2011); (II) In 1 mM Fe(CN)$_6$$^{3-/4-}$ and 0.1 M KCl where *blue* = Bare GCE and *purple* = Co(II)-PDC/GCE (Image taken from Murinzi et al., 2017).

Recently, pure PDC doped PPY (PDC/PPY) (0.02 M) was successfully synthesized by hydrothermal reaction on carbon felt electrode giving rise to interesting porous structural properties on the electrode surface (Arvas et al., 2022). Its design was to perform as a promising asymmetric aqueous supercapacitor device giving exceptionally high specific capacity of 854.2 Fg^{-1} at 2.7 A.g^{-1} current density with 884.4 Wh.kg^{-1} energy density via GCD and good cycling stability with 87.3% capacitance retention after 400 cycles at 10 A.g^{-1} current density and 3 V operating voltage by CV measurements. The three-electrode system was assembled in 1 M H_2SO_4 electrolyte with graphite plate as counter electrode. The synthesis through hydrothermal polymerization of pyrrole with PDC was performed at a moderate temperature of 180°C with $FeCl_3.6H_2O$ as oxidant, which is an alternate way than some of the existing PPY composite design methods where usually the composite material is either chemically or electrochemically polymerized and deposited over an electrode surface. Nonetheless, the results of this study still proved the efficacy of the judicious fabrication of PPY with PDC as new porous composite films displaying good capacitive properties through synergistic effect.

2.9 Studies of PPY with various metal compounds as composite electrode materials

Transition metals have already been utilized and incorporated with different conducting polymers including PPY making hybrid composites for electrode material and have shown positive results for improved electrochemical performances as hybrid electrodes for energy storage. Shimoga et al., (2021) documented diverse list of metal-based composites integrated with PPY network demonstrating a significant improvement in specific capacitance when compared to the components by its own. Early transition metals (*e.g.,* Ag, Cu, Cd, Zn) have already been fabricated into PPY based hybrid composites. In most cases, the metallic components are metal oxides and MOFs. Because of their tuneable properties, porosity and very high surface area, there have been several studies of MOFs with conducting polymers and carbon materials as electrodes (Shin et al., 2023). For example, Liu et al. (2020) prepared bimetal organic framework nanosheets wrapping PPY nanotubes (NiCo-MOF@PNTs) as composites and its assembly as asymmetric supercapacitor demonstrates a high energy density of 41.2 Wh.kg^{-1} at a power density of 375 W.kg^{-1}. However, most pristine MOFs are electrically insulating, have lower cycling stability, steric hindrance for ion insertion, limited stable voltage window and poor rate performance in comparison, as a result they are commonly incorporated with other electroactive materials to overcome their drawbacks (Shin et al., 2023; Juni et al., 2021). **Table 2.2** lists some existing supercapacitor electrode studies of transition metals (Ag, Cd, Cu and Zn) based compounds.

Table 2.2: Selected studies of transition metals compounds as hybrid nanocomposites and their electrochemical performance

Fabricated electrode	**Electrolyte**	**Specific capacitance**	**Current density or Scan rate**	**Capacitance retention**
Ag/PPY on graphite sheet (Gan et al., 2015)	1 M H_2SO_4	414 $F.g^{-1}$	0.2 $A.g^{-1}$	98.9% at 0.5 A g^{-1} after 1000 cycles
CuO/PPY on Cu foam (Shen et al., 2021)	3 M KOH	675 $F.g^{-1}$	2 $mA.cm^{-2}$	103.57% after 8000 cycles
$CdCO_3/CdO/Co_3O_4$ on Ni foam (Henríquez et al., 2021)	3 M KOH	84 $F.g^{-1}$	1 $mA.cm^{-2}$	92% after 6000 cycles
rGO/CdS/PPY on graphite rod (Purty et al., 2018)	1 M KCl	~844 $F.g^{-1}$	~1 $A.g^{-1}$	92.8% after 2000 cycles
$ZnCo_2O_4$/PPY on Ni foam (Chen et al., 2015)	3 M KOH	1559 $F.g^{-1}$	2.0 $mA.cm^{-2}$	90% at 10.0 mA cm^{-2} after 5000 cycles
ZnO/PPY on fluorine tin oxide (Xue et al., 2020)	1 M KCl	161.02 $F.g^{-1}$	0.5 $A.g^{-1}$	70.71% after 5000 cycles

The encapsulation of silver nanoparticles by PPY is among the easiest method available to fabricate PPY-metal composite electrodes. The redox reaction between $AgNO_3$ and PPY provides a facile route to produce Ag/PPY based nanocomposites with core-shell structures (Singh et al., 2020; Bhat, 2023), surface loading (Sabalová et al., 2017; Mao et al., 2018), yolk-shaped structures (Zhao et al., 2019; Rodtuk et al., 2023) and nanowires (Baratto & Pezzin, 2022). In certain cases, upon incorporation of metal composites with PPY via polymerization, a similar trend of redox peaks has been reported from CV compared to PPY electrode alone, hence showing the influence of metal entities in the composite. The redox peaks observed for Ag/PPY nanocomposite electrode (Gan et al., 2015) at 0.5 V and 0.2 V has been associated with the oxidation and reduction of Ag nanoparticles in the composite (**Figure 2.11 (a,b)**). In this example, silver nanoclusters from $AgNO_3$ were electrodeposited via in situ redox reaction with pyrrole on graphite sheet. The results showed the composite had good capacitance behaviour

(**Table 2.2**) through both CV and GCD studies and the redox behaviour is affected by the size of Ag particles. Furthermore, comparison of the EIS performance of PPY vs Ag/PPY recorded in frequency range of 10 mHz to 100 kHz revealed low equivalent series resistance and charge transfer resistance of Ag/PPY, which suggested better utilization of PPY in the composite as the addition of Ag particles enhanced the electron hopping system of the conducting polymer. The composite had typical cauliflower like PPY with Ag nanoparticles and clusters embedded within the film after optimization. The evenly distributed Ag nanoparticles enhanced electron hopping while the nanoclusters acted as spacers that avoided the restacking of PPY film.

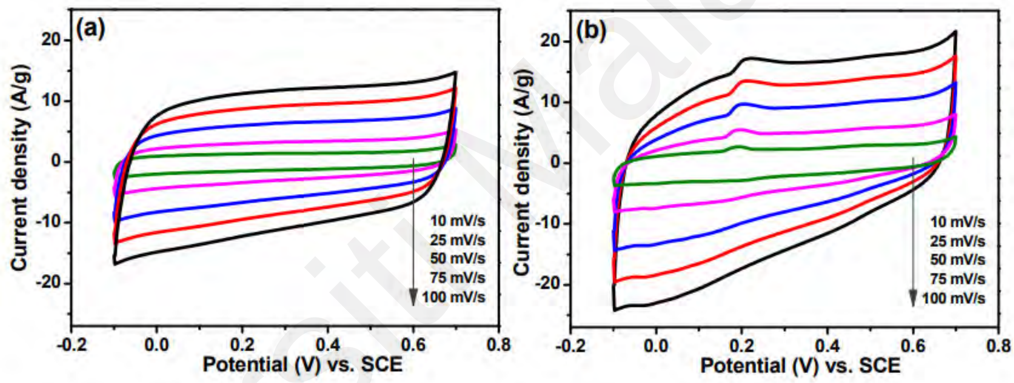

Figure 2.11: Reported CV curves (a) PPY, (b) Ag/PPY electrode (Image taken from Gan et al., 2015).

Cadmium based PPY nanocomposites such as CdO/PPY and CdS/PPY are reported as enhanced photocatalysts with improved photoconductivity (Madani et al., 2011; Shan et al., 2018; Ahmad et al., 2020; Anwar et al., 2020) and as enhanced thermoelectric materials (Bibi & Shakoor, 2021) compared to pristine PPY. The prospects of CdS/PPY as electrode materials for supercapacitor was also studied by fabricating it with reduced graphene oxide (rGO) nanosheets (Purty et al., 2018). The results revealed that rGO/CdS/PPY composite had low charge transfer resistance, great capacitance, good cyclic stability with 92.8 % capacitance retention after 2000 cycles (**Table 2.2**). It was also suggested that the optimized composite possessed both EDLC and pseudocapacitor behaviour which showed improved efficiency as a hybrid supercapacitor with better electrochemical performance than pure PPY.

Copper oxides and copper sulfides have been established as important materials in the field of energy storage applications, catalysis and photovoltaics (Majumdar & Ghosh, 2021; Majumdar, 2021) because of their low cost, high chemical stability and durability. CuO heterojunction nanowire arrays with PPY (CuO/PPY) have been reported to exhibit high capacitance without the use of any binders (Shen et al., 2021; Zhang et al., 2021). The increased capacitance was due to the increased specific surface area that afforded sufficient active sites and improved electron transfer. Besides supercapacitors, copper based PPY composite materials have been investigated in high cyclic stability anodes for Li-ion batteries (Feng et al, 2020), Na-ion batteries (Yue et al., 2022), nanocatalytic tumour therapy (Chen et al., 2022), enhanced solar hydrogen generation as catalysts (Ghost et al., 2020) and dye-sensitized solar cells (Rafique et al., 2021).

Zn-ion batteries and hybrid supercapacitors using aqueous electrolytes are newly emerging as promising energy storage devices (Liu et al., 2020). PPY has been incorporated with Zn based materials exhibiting high energy storage potential. A Zn/PPY composite cathode fabricated with graphene oxide has been reported to exhibit high energy and power density that outperformed the Zn-ion hybrid supercapacitors using carbon cathodes (Yang et al., 2021). The performance was attributed to the insertion/de-insertion of monovalent anions and fast ion-diffusion process in the pores of the composite material. Xue et al. (2020) also reported ZnO/PPY nanocomposites whose orderly porous structures shortened the charge carrier transport distance and increased the capacitance. Another orderly porous Zn based PPY composite ($ZnCo_2O_4$/PPY) was reported that had $ZnCo_2O_4$ nanowires which served as efficient scaffolds to ensure the fine distribution of PPY at nanoscale, making them electrochemically accessible and enhance the adhesion of the composite materials over the Ni foam substrate (Chen et al., 2015). Pairs of distinct reversible redox peaks are noted at different scan rates with -0.1 V to 0.58 V for $ZnCo_2O_4$/PPY hybrid composites (**Figure 2.12(a,b)**) which were attributed to rapid faradaic capacitive behaviour and electrode polarization effect. The hybrid electrode material was fabricated by a facile two-step method through electro-polymerization of 0.5 M pyrrole monomers with $ZnCo_2O_4$ nanowires on Ni foam and was free from carbon additives and binders. The electrochemical performance of improved stability and high capacitance were attributed to the synergistic effect of the pseudocapacitive properties of $ZnCo_2O_4$ nanowires and PPY nanofilms from their porous architectures which facilitated good conductivity and facile ion diffusion path.

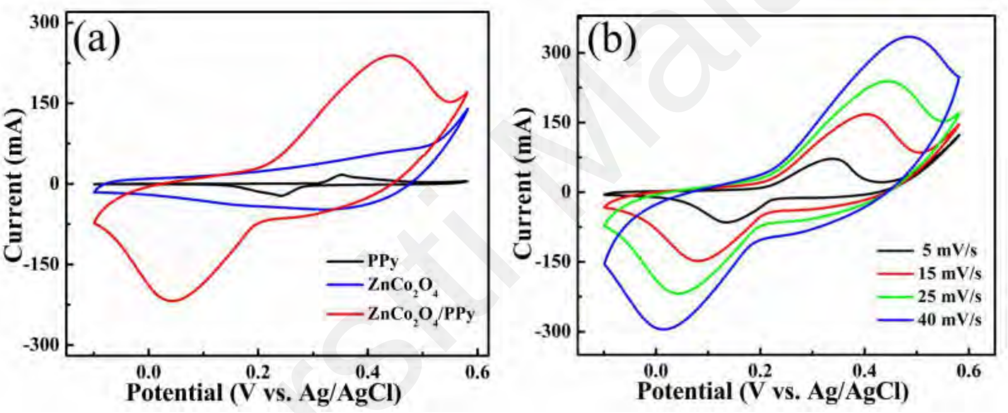

Figure 2.12: Reported CV curves (a) PPY, $ZnCo_2O_4$, $ZnCo_2O_4$/PPY hybrid electrodes at 25 mV.s^{-1} (b) $ZnCo_2O_4$/PPY (Image taken from Chen et al., 2015).

2.10 Summary

The surface morphology and the structure of electrode material plays an important role in its electrochemical performance. Existing PPY-metal composites have diverse morphologies obtained by both chemical oxidative and electropolymerized deposition that influenced the charge transfer and storage mechanism of its fabricated device. The studies of the four transition metals of interest – Ag, Cd, Cu and Zn with PPY has been reported but mostly as metal oxides or sulfides. Furthermore, PDC based metal complexes of Ag, Cu and Zn has also been reported (CCDC-248754, CCDC-1936104 and CCDC-

143229 respectively) however their electrochemical studies as composites electrode for supercapacitor has been less explored.

PPY on its own as an electrode material has relatively low specific capacity per unit gram and its large-scale application is hindered by its low cycling life due to shrinkage of its polymer chains during the charge-discharge process (Sarno, 2020). However, when it is integrated with other chemically active materials it is shown to function as an efficient pathway for charge transfer as well as endure fast redox reaction instigated by the corresponding metal components. Hence, there have been many successful efforts in fabricating new and enhanced supercapacitor electrodes for flexible electronics with a facile and low-cost synthesis having the ease of reproducibility and stability (Wang et al., 2020; Fan et al., 2022; Shimoga et al., 2021). Since the fabrication of other metal-based compounds and PDC with PPY have already been reported to show good conductivity and capacitive properties, the incorporation of PPY into metal-PDC based complexes can be predicted to give interesting results regarding the significance of extending new studies for PDC based metal complexes as hybrid electrode materials for energy storage devices.

CHAPTER 3: METHODOLOGY

3.1 Chemicals and reagents used

All the chemicals and solvents were analytical reagent grade and were used without additional purification. The list of chemicals used in this work are compiled in **Table 3.1**.

Table 3.1: List of chemicals

Manufacturer	**Chemicals**	**Molecular weight ($g.mol^{-1}$)**	**Details**
Sigma-Aldrich (Steinhem, Germany)	PDC ($C_7H_5NO_4$)	167.12	99%
	Pyrrole (C_4H_5N)	67.09	98% 0.967 $g.mL^{-1}$ at 25 °C
	Sodium *p*-toluenesulfonate, *p*-TSO ($CH_3C_6H_4SO_3Na$)	195.18	95%
	Potassium hexacyanoferrate ($K_3[Fe(CN)]_6$)	329.24	≥99%
	Ammonium persulfate, APS ($[NH_4]_2S_2O8$)	228.20	≥98.5%
	Zinc chloride ($ZnCl_2$)	136.30	≥98%
	Polyvinylidene fluoride, PVDF ($[CH_2CF_2]_n$)	~534,000 by GPC (average)	1.74 g/mL at 25 °C
R&M chemicals (Subang, Malaysia)	Dimethyl sulfoxide, DMSO ($[CH_3]_2SO$)	78.13	≥98%
	Potassium chloride (KCl)	74.55	99 - 100.5%
Systerm Chemicals (Shah Alam, Malaysia)	Copper nitrate trihydrate ($Cu[NO_3]_2.3H_2O$)	241.60	99%
Fisher Scientific (Leicestershire, UK)	Silver nitrate ($AgNO_3$)	169.87	≥99.7%
	Carbon black (C)	12.01	≥99.9%
Scharlau (Barcelona, Spain)	Cadmium nitrate tetrahydrate ($Cd[NO_3]_2.4H_2O$)	308.47	99%
Merck (Darmstadt, Germany	N-methyl pyrrolidone, NMP (C_5H_9NO)	99.13	99.5%
Friendemann Schmidt (Germany)	Sulphuric acid (H_2SO_4)	98.08	95-97%

3.2 Instrumentations and measurement parameters

The characterization processes involved in this research are compiled with details in this section.

3.2.1 Fourier transform infrared spectroscopy (FTIR)

Each of the synthesized complexes, PPY-complex composites and pure PPY were characterized by FTIR spectrophotometer from Perkin Elmer FTIR-Spectrum 400 in the region of 4000-400 cm^{-1} wavelength by identifying the characteristic bands of functional groups. Prior measurement, the sample films were carefully peeled off the ITO piece whereas the powder and crystal samples were finely grounded. The FTIR was performed by attenuated total reflection (ATR) technique where a small amount of sample was simply placed and pressed against a highly refractive index prism (made of germanium). The infrared spectrum was measured using infrared light beam that is totally internally reflected by the prism in contact with the sample. The FTIR peaks of samples were analysed using Spectraglyph 1.2 software.

3.2.2 Thermogravimetric analysis (TGA)

Thermal stability of all the samples was studied by Perkin Elmer TGA-4000 Thermogravimetric Analyzer at temperatures 30°C-600°C at a heating rate of 10°C min^{-1}. About 5-10 mg of each sample was taken and the TGA curves were analysed using Origin 8.5 software and Excel.

3.2.3 X-ray diffraction (XRD)

The crystallinity and molecular structure of the complexes were characterized and confirmed from its bulk sample by XRD analysis. High quality single crystals were selected and studied on Oxford Supernova single crystal X-ray diffractometer from Agilent. Powder X-ray diffraction (PXRD) analysis was conducted using EMPYREAN

PANalytical X'Pert HighScore diffractometer. The results of the metal complexes were further compared with previously reported available data.

3.2.4 Field emission scanning electron microscopy (FESEM) and energy dispersion X-ray (EDX)

Surface morphological images, weight percentages and EDX spectral data in order to confirm the elemental composition of all the prepared samples were produced and measured concurrently by Hitachi FESEM Model SU8220. Before transferring into the FESEM sample chamber, the powder samples were evenly dispersed on the carbon adhesive and the films were simple cut into small pieces and pasted over the adhesive.

3.2.5 Cyclic voltammetry (CV)

Electrochemical synthesis of PPY and its film composites on ITO glass were performed on DY2312 Digi-Ivy Potentiostat at room temperature in a three-electrode system. The same potentiostat was used to perform CV for recording and comparing the shape of the voltammograms and current responses at fixed potential window and scan rate. The CV of the powder composites as slurry on graphite sheet in a three-electrode system was performed on Metrohm Autolab potentiostat PGSTAT30 at room temperature. Data analysis was carried out using NOVA 2.1.6 and Origin 8.5 software. More details of the electrochemical cell set-up for CV are discussed in **Section 3.5.1** and **Section 3.5.2**.

3.2.6 Electrochemical impedance spectroscopy (EIS)

To analyze impedance and determine the conductivity of the composite sample films, the impedance was measured by HIOKI 3532-50 LCR HiTESTER in the frequency range of 40 Hz to 5 MHz at room temperature. More details about the set-up are discussed in **Section 3.5.4**. Meanwhile, the impedance of the powder composites samples was measured in the same three-electrode cell after its CV which was performed on Metrohm Autolab potentiostat PGSTAT30 at room temperature. Frequency of 0.1 Hz to 100 kHz was applied under open circuit voltage at 0.01 potential amplitude. More details about the set-up are discussed in **Section 3.5.3**. The Nyquist plots were studied using Origin 8.5 software.

3.3 Experimental procedures for the synthesis of metal-PDC complexes

Synthesis of metal–PDC crystals were all performed at room temperature using simple dissolution method while maintaining a 3:1 solvent ratio of H_2O–DMSO adapted from literature (Vijayan, 2020). Visual images of the complexes are shown in **Appendix E**.

3.3.1 AgPDC

$AgNO_3$ (0.076 g, 0.45 mmol) and PDC (0.15 g, 0.90 mmol) were dissolved and sonicated for a minute in 18 mL distilled water and 6 mL DMSO, respectively. The acid solution was poured into the silver salt solution in a dropwise manner and was left to react undisturbed. Colourless prismatic crystals (0.181 g, 80.39%) were seen after a week and they were isolated upon filtration, washed with water and acetone and left to dry at room temperature and collected.

3.3.2 CdPDC

$Cd(NO_3)_2.4H_2O$ (0.309 g, 0.97 mmol) and PDC (0.491 g, 4.44 mmol) were dissolved and sonicated for 2 minutes in 18 mL distilled water and 6 mL DMSO, respectively. The acid solution was poured into the cadmium salt solution in a dropwise manner and was left to react undisturbed. White crystals were seen slowly forming and after a week the obtained the crystals (0.668 g, 83.5%) were isolated upon filtration, washed with water and acetone and left to dry at room temperature and collected.

3.3.3 CuPDC

$Cu(NO_3)_2.3H_2O$ (0.204g, 0.82 mmol) and PDC (0.396g, 2.39 mmol) were dissolved and sonicated for a minute in 15 mL distilled water and 5 mL DMSO, respectively. The acid solution was poured into the copper salt solution in a dropwise manner and was left to react undisturbed. Blue crystals were seen within few minutes after the pouring was complete. After 1 week the obtained the crystals (0.491g, 83%) were isolated upon filtration, washed with acetone and collected after it was left to dry at room temperature.

3.3.4 ZnPDC

$ZnCl_2$ (0.052g, 3.6 mmol) and PDC (1.20g, 7.2 mmol) were dissolved and sonicated for a minute in 15 mL distilled water and 5 mL DMSO, respectively. The acid solution was poured into the silver salt solution in a dropwise manner and was left to react undisturbed. White crystals (0.577g, 46.08%) were seen shortly after the pouring was complete. After 2 weeks the crystals were isolated upon filtration, washed with water and acetone, left to dry at room temperature and collected.

3.4 Experimental procedures for the synthesis of PPY/metal–PDC composites

3.4.1 By chemical oxidation

PPY/metal–PDC composites and pure PPY were synthesized in a similar manner by following a literature (Wang et al., 2018) using *in-situ* polymerization technique. Pyrrole monomer (69 μL, 0.05 M) solution was prepared in 20 mL of distilled water and set aside. 10 mL of distilled water was added to 0.05 g of the prepared complex, sonicated for 10 minutes to let it disperse as nanoparticles and then was subsequently poured into the pyrrole solution. Ammonium persulfate (0.45 g, 0.1 M) solution was prepared with 20 mL of distilled water and then was added to the pyrrole-complex mixture while stirring continuously for 3-4 hours to allow polymerization. The reaction mixture was left aside, later the black precipitate of the composite formed was filtered, rinsed with distilled water and acetone multiple times to remove any remaining reactants. Pure PPY was also prepared in the same manner except for the inclusion of complexes. After collecting, the PPY/metal-PDC composites as well as pure PPY were dried in oven at 80°C for 24 hours to remove any moisture. All the samples were obtained as black colour powder which is characteristic of PPY (**Figure 3.1**)

Figure 3.1: Typical black colour powder form of PPY and its composites by chemical oxidation.

3.4.2 By electrochemical polymerization

About 0.025 g of metal-PDC complex was taken and sonicated for an hour in 40 mL distilled water, meanwhile 0.97 g (0.08 M) of sodium *p*-toluenesulfonate dopant and 1 mL (0.28 M) of pyrrole monomer were taken and mixed with 10mL distilled water. After the complex was finely dispersed via sonication it was added to the pyrrole solution with 2-3 drops of pH 5 phosphate buffer and was poured into a three-electrode glass vessel. The electrochemical cell was prepared using Ag/AgCl reference electrode (RE), ITO glass piece (2 cm × 3 cm) as working electrode (WE) with its conductive side suspended into the analyte and facing towards the graphite rod counter electrode (CE) as shown in **Figure 3.3**. Once it was ready, potential was applied from 1.25 V to -0.2 V at a scan rate of 50 mVs^{-1} for 20 cycles. A black film eventually covered the ITO surface that was suspended into the solution. After the synthesis was completed, the ITO piece with the composite film was taken out and washed with distilled water to remove any unreacted monomers and was left to dry in air. Pure PPY was prepared in the exact manner as above without including any metal complex into it. All composites deposited over the ITO piece as fine black films with a surface area roughly about 2 cm × 2 cm as shown in **Figure 3.2**.

Figure 3.2: Polymeric film deposit on the conductive side of ITO glass piece after electrochemical synthesis.

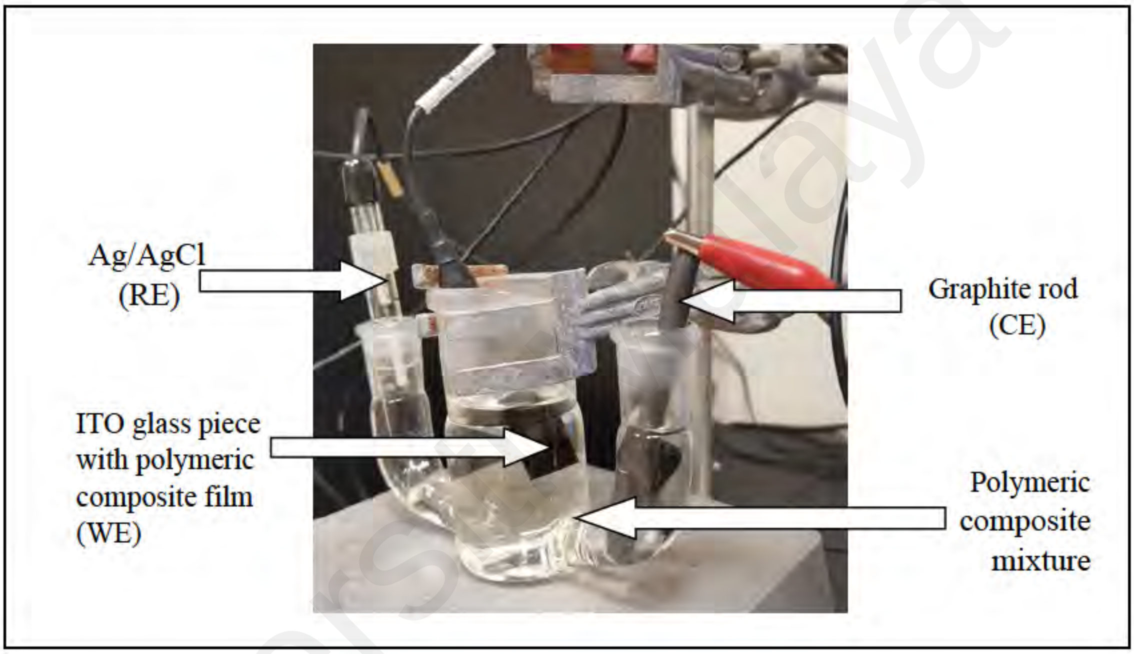

Figure 3.3: Three-electrode cell set up for electrochemical polymerization of PPY and its composites.

3.5 Electrochemical analysis

3.5.1 CV of PPY/metal–PDC powder composites

A viscous slurry of each sample was prepared consisting of the powder sample, carbon black powder and PVDF at 8:1:1 mass ratio in NMP solvent. Carbon black was added to aid in conductivity and PVDF helps to bind the active material together (Imaduddin et al., 2021). The slurry was then coated on a graphite sheet covering 1 cm^2 of it (see **Figure 3.4**) and dried in oven at 60°C for 3 hours prior analysis. The CV of PPY and its powder composites were conducted on the slurry-coated graphite sheets as working electrodes, Ag/AgCl as reference electrode and platinum wire as counter electrode immersed in 1 M H_2SO_4 electrolyte (see **Figure 3.5**). The CV was recorded at -0.2 V to +0.8 V potential window and a scan rate of 10 $mV.s^{-1}$ in 3 cycles.

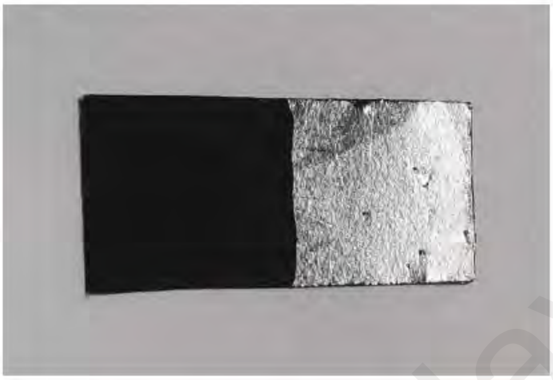

Figure 3.4: Slurry of sample coated on graphite sheet.

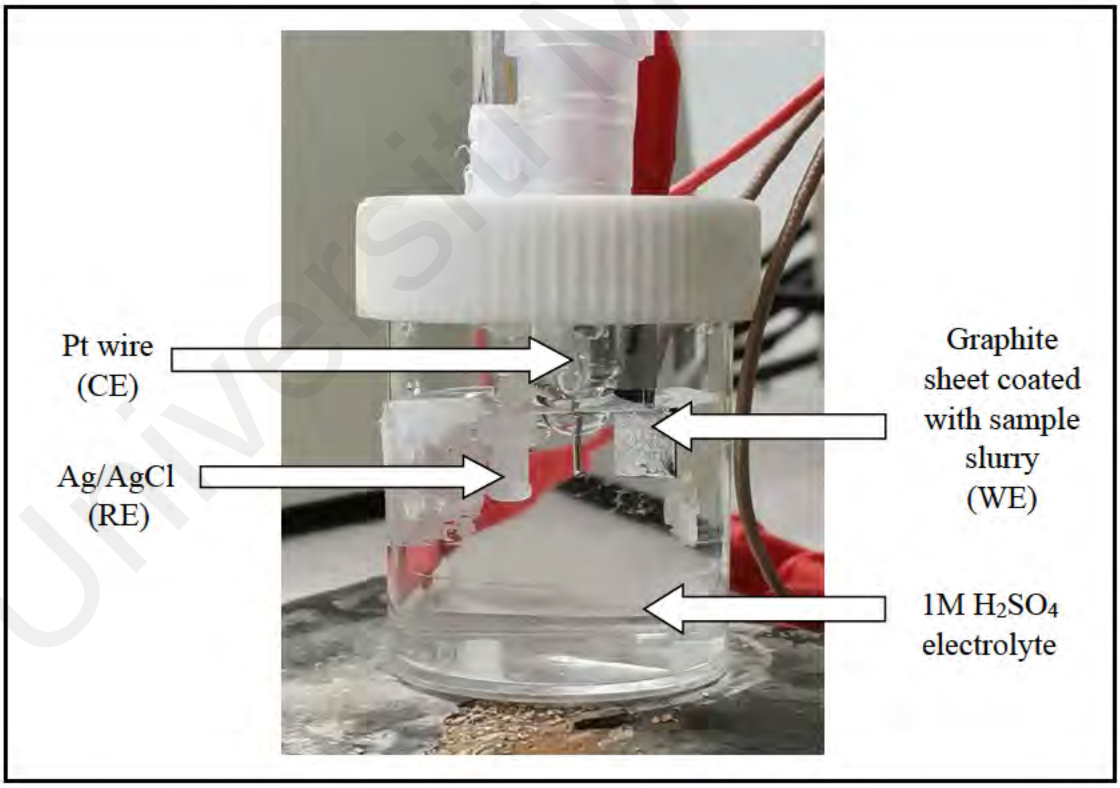

Figure 3.5: Electrochemical cell set-up for CV of powder composites.

3.5.2 CV of PPY/metal–PDC film composites

In order to investigate the electrochemical properties of PPY and its composites, CV was recorded at room temperature at potential range of -0.5 V to +0.9 V and scan rate of 10 mV.s^{-1} in 3 cycles. Ag/AgCl reference electrode, ITO electrode piece with the composite film as working electrode and graphite rod as counter electrode were suspended into the electrolyte solution in a three-electrode glass vessel (See **Figure 3.6**). The electrolyte was prepared in 50 mL distilled water with 0.16 g (0.01 M) of potassium hexacyanoferrate ($K_3[Fe(CN)]_6$) and 0.38 g (0.1 M) of KCl. Potassium hexacyanoferrate is a known redox additive that is added to an electrolyte mixture to improve the charge transport with its faradaic redox reaction [$Fe(CN)_6^{4-}/Fe(CN)_6^{3-}$] and enhance the electrochemical performance of a device (Qin et al., 2022).

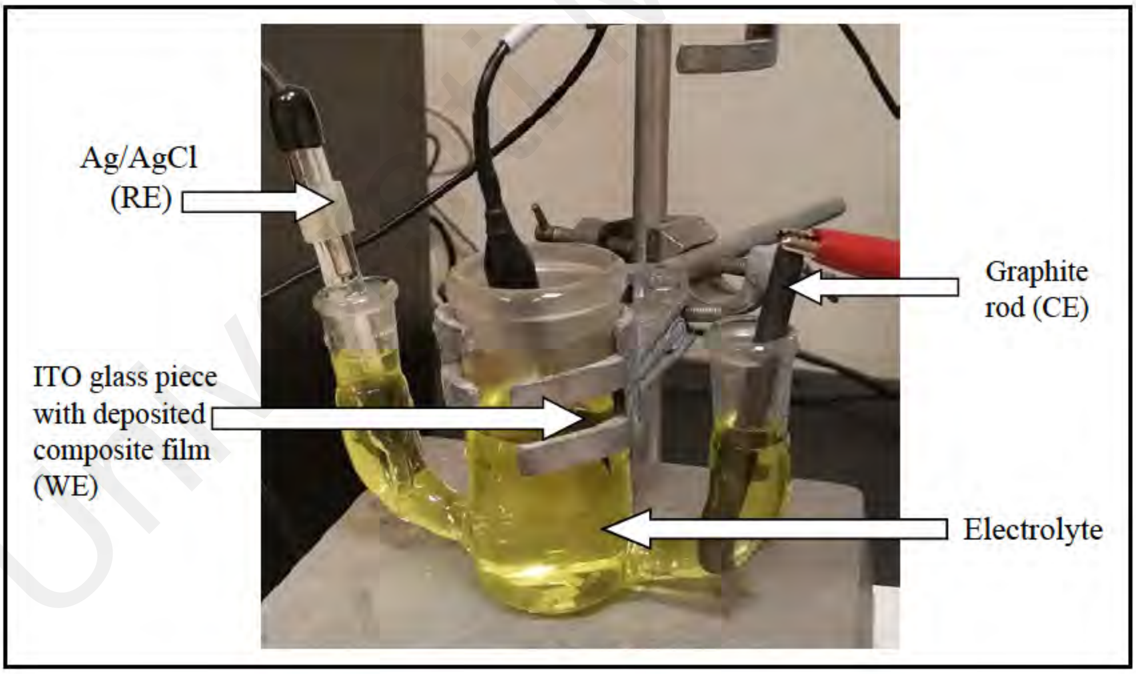

Figure 3.6: Electrochemical set-up for film composite formation by CV.

3.5.3 EIS of PPY/metal–PDC powder composites

The EIS of PPY and its powder composites was carried out in the same electrochemical set up as mentioned in **Section 3.5.1** and shown in **Figure 3.5**. It was conducted in the frequency range of 0.1 Hz – 100 kHz at room temperature in 1 M H_2SO_4 electrolyte. The conductivity and resistances were determined from the obtained Nyquist impedance plots.

3.5.4 EIS of PPY/metal–PDC film composites

The conductivity and resistances of all the complexes, PPY film and its film composites was determined by EIS in the frequency range of 40 Hz – 5 MHz at room temperature from its Nyquist impedance plots. The prepared samples were placed between a stainless-steel electrode holder. The metal-PDC complexes were first compressed to form disks having an area of about 2 cm^2 by applying about 5 tons pressure. The prepared disk was sandwiched between two stainless steel holders and then its impedance was measured. PPY and its composites obtained as deposited films were initially peeled off from the ITO glass piece and were placed between the electrodes for acquiring the impedance spectra. Due to the thin nature of the film composites, it was directly placed between the electrode holder fully covering the surface of 2 cm^2 without cutting the excessive portion (see **Figure 3.7**). For calculating conductivity, the thickness and area of the samples were noted and the bulk resistance was obtained from its Nyquist plot.

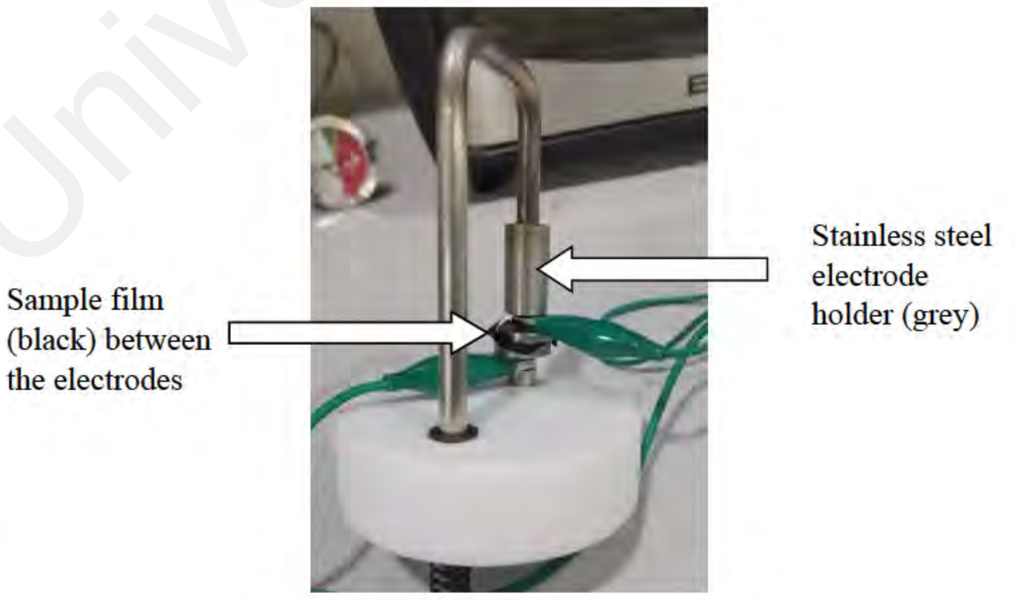

Figure 3.7: EIS set-up for films.

CHAPTER 4: RESULTS AND DISCUSSION

4.1 FTIR analysis

4.1.1 Metal complexes

FTIR spectral analysis of the metal–PDC complexes is summarized and represented in **Table 4.1 and Appendix A.** The peaks of the complexes were compared to free PDC ligand. The characteristic stretching bands of ν(O-H), ν(C=N), ν(C=O), δ(C-H) and ν(C=C) of the ligand are present for all its metal complexes. New broad peaks over 3000 cm^{-1} are observed for all metal complexes indicating the presence of water molecules through O-H stretching vibrations. For metal–PDC complexes, the absorption bands for the C=O stretching vibrations are observed sharply in 1690-1750 cm^{-1} region and it indicates the presence of protonated carboxyl bond which is arising from the PDC ligand. Whereas, the absence of sharp peaks in the same region indicates that the carboxyl bond has been deprotonated and the lowered shift of peaks arise from the metal back bonding to the ligand's C=O antibonding orbital. Hence, the chelating behavior of PDC to the metals is suggested by the shift of carbonyl stretching bands in the metal complexes (Zang et al., 2015; Demir et al., 2017; Murinzi et al., 2017). The asymmetric COO^- stretching vibrations (ν_{as}) of the complexes are observed around 1570-1650 cm^{-1} region meanwhile, the symmetric COO^- stretching vibrations (ν_s) are observed around 1290-1390 cm^{-1} region. The difference between the asymmetric (ν_{as}) and symmetric carboxylate (ν_s) stretching bands *i.e.,* $\Delta\nu(COO^-) = [\nu_{as}(COO^-) - \nu_s(COO^-)]$ is used to distinguish the various coordination modes of the ligand. The carboxylate ion may coordinate to a metal ion in one of the ways shown in **Figure 4.1.** A large difference over 200 cm^{-1} is known to imply monodentate coordination while a difference of 100 cm^{-1} and below implies bidentate coordination of the carboxyl group to the metal (Zang et al., 2015; Khan et al., 2009).

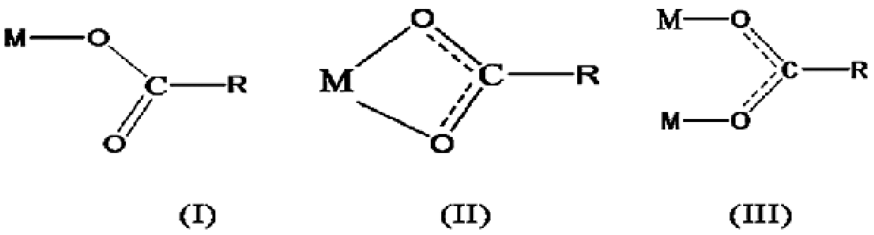

Figure 4.1: Binding modes of carboxyl group. (I) monodentate mode, (II) bidentate mode and (III) bridging mode (Image taken from Shahroosvand et al., 2013).

AgPDC**:** The IR spectrum of AgPDC reveals the presence of $\underline{v}$(C=O) stretching band by a medium peak at 1729 cm^{-1}. Furthermore, asymmetric and symmetric COO^{-} stretching bands are also observed at 1583 cm^{-1} and 1302 cm^{-1} respectively. The presence of v(C=O) and v(COO^{-}) bands indicate that the ligand is partially deprotonated with a single carboxyl group coordinated to Ag^{+} ion. Its Δv(COO^{-}) value (281 cm^{-1}) being greater than 200 cm^{-1} also supports the monodentate binding mode. Two new peaks are observed sharp at 469 cm^{-1} and 533 cm^{-1} which correspond to v(Ag-N) and v(Ag-O) vibrations respectively. In addition, peaks observed at increased wavelengths at 1545 cm^{-1} and 1451 cm^{-1} are assigned to the aromatic v(C=N) and v(C=C). Hence, this suggests that each PDC molecule is bidentately coordinated to an Ag^{+} ion through its nitrogen and one oxygen of its carboxyl group. v(C=N) band of AgPDC is observed to be the highest among the metal–PDC complexes and this can be explained by the comparatively larger bond length of Ag-N and shorter bond length of C-N obtained from its single crystal structure. Shorter bond length is known to result stronger bond energy and higher vibrational frequency (Nguyen et al., 2022). Broad peaks observed at 3297 cm^{-1} corresponds to v(O-H) stretching vibrations shows the presence of water molecules. The structure of AgPDC is shown in **Figure 4.2**. All the peaks are well in agreement with previously reported values of AgPDC (Etaiw & El-bendary, 2018).

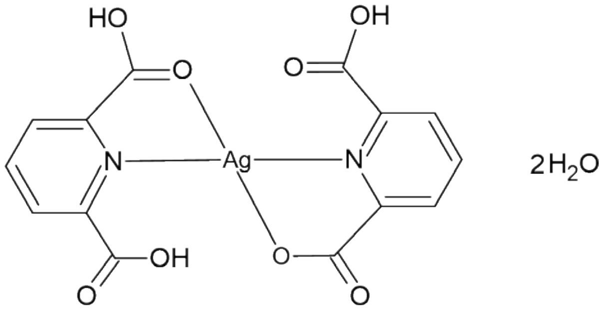

Figure 4.2: Molecular structure of AgPDC.

CdPDC**:** A sharp peak corresponding to *v*(C=O) is observed at 1692 cm^{-1} similar to the free ligand. Medium bands of v_{as}(COO$^-$) and v_s(COO$^-$) are observed at 1614-1574 cm^{-1} and 1373 cm^{-1} respectively and their difference of 218 cm^{-1} and 201 cm^{-1} indicate monodentate binding mode to the Cd(II) center. Presence of medium *v*(Cd-O) and weak *v*(Cd-N) vibrations are also observed at 535 cm^{-1} and 467 cm^{-1} (Yin et al., 2015). Since the *v*(C=O) peak of CdPDC is observed at the same wavenumber as the free ligand this also suggests the presence of some protonated carboxyl groups from PDC, which is further confirmed from single crystal that it is in fact attributed to the presence of an uncoordinated PDC in the single crystal lattice. Multiple sharp bands representative of *v*(C=N), *v*(C=C) and pyridyl ring vibrations are observed at 1470 cm^{-1}, 1460 cm^{-1} and 1300-700 cm^{-1} regions respectively (Murinzi et al., 2017). Broad bands centered at 3405 cm^{-1} indicate the presence of coordinated water molecules in structure. The structure of CdPDC is shown below in **Figure 4.3**. The three Cd-coordinated water molecules are shown in parenthesis and the bridging bonds of Cd-O are depicted *via* arrow signs.

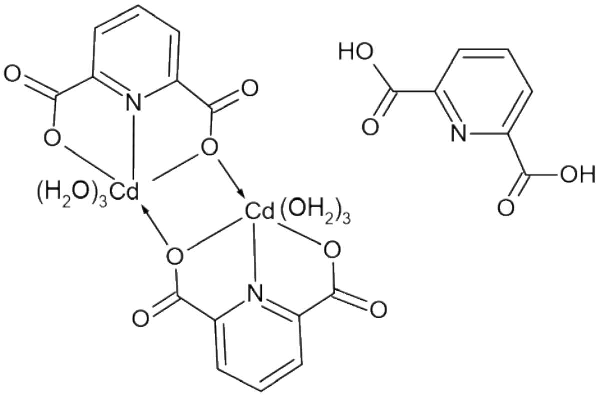

Figure 4.3: Molecular structure of CdPDC.

CuPDC**:** Lowered *v*(C=O) stretching band at 1673 cm^{-1} indicates the presence of deprotonated carboxyl group (Majumder et al., 2006). Both the asymmetric and symmetric carboxyl stretches show a similar shift to lower wavelengths at 1648-1596 cm^{-1} and 1332-1311 cm^{-1} respectively, thereby increasing the *Δv*(COO$^-$) values to 316 cm^{-1} and 285 cm^{-1}. It suggested that the carboxyl groups behave as monodentate to the Cu(II) center. New peaks occurring at 459 cm^{-1} and 575 cm^{-1} are attributed to *v*(Cu-O) and *v*(Cu-N) respectively (Derikvand et al., 2012). Among the complexes, CuPDC has lower metal-O and higher metal-N vibrational bands arising from its larger bond length of Cu-O and shorter bond length of Cu-N respectively (Nguyen et al., 2022). Peaks corresponding to *v*(C=N) and *v*(C=C) are observed at 1471-1427 cm^{-1} regions, the increased shift hence indicated that the ligand binds as tridentate with its nitrogen and two carboxyl groups to the metal. These results are in agreement with its single crystal structure. The presence of water is confirmed upon observing broad peaks centered around 3498 cm^{-1} from *v*(O-H) vibrations (Scaldini et al., 2014). The structure of CuPDC is depicted in **Figure 4.4**.

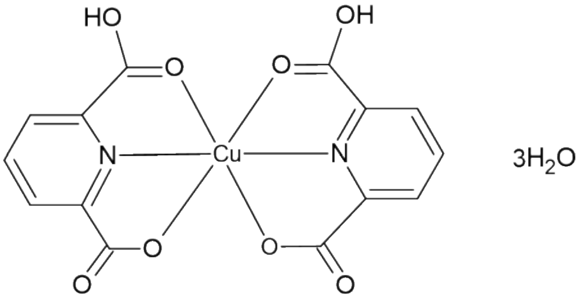

Figure 4.4: Molecular structure of CuPDC.

ZnPDC**:** The *v*(C=O), v_{as}(COO$^-$) and v_s(COO$^-$) stretches are observed sharply at 1692 cm^{-1}, 1595-1574 cm^{-1} and 1330 cm^{-1} respectively. Values of Δv(COO$^-$) being 265 cm^{-1} and 281 cm^{-1} and the absence of strong band of protonated C=O at 1690-1750 cm^{-1} region suggests that the carboxyl group of the ligand binds as monodentate to the Zn(II) center. The *v*(C=N) and *v*(C=C) peaks are present relatively unchanged at 1455 cm^{-1} and 1413 cm^{-1} respectively, however new peaks are seen to occur at 516-458 cm^{-1} attributed to the *v*(Zn-O) and *v*(Zn-N) vibrations. As a result, it suggests that the ligand behaves as tridentate to the metal. Broad peaks are seen at 2819-3068 cm^{-1} which are correlated to *v*(O-H) indicating the presence of water molecules in the complex. The results are in agreement to its single crystal and literature (Martak & Christanti, 2014). The structure of ZnPDC can be seen in **Figure 4.5.**

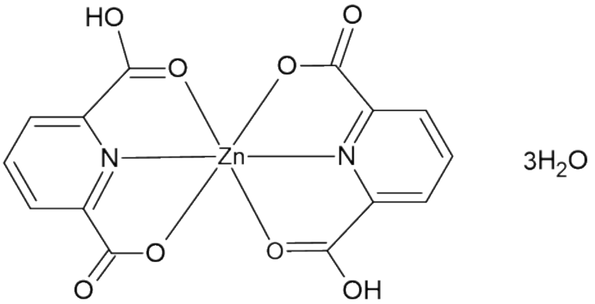

Figure 4.5: Molecular structure of ZnPDC.

4.1.2 PPY/metal–PDC powder composites

The successful incorporation of PPY into the metal complexes was identified by comparing the resulting spectra of the composite powder samples with the original metal complexes and pure PPY. The characteristic peaks of the important functional groups of the metal complex and PPY within the composites are identified and summarized in **Table 4.2** and stacked in **Appendix B**. The important peaks of the free PPY as synthesized include 1680 cm^{-1} (C=N) stretch, 1577 cm^{-1} (C=C) stretch, 1300 cm^{-1} (C-N) stretch, 3514 cm^{-1} (N-H) stretch. Furthermore, (C-H) wagging peaks can also be seen at 800-934 cm^{-1} region. The peaks observed in the present work matched close to the ones available in literature (Chogule et al., 2011), hence confirming the formation of PPY.

Identifying peaks of the PPY in the composites can be found at 1618-1644 cm^{-1} (C=N) stretch, 1300-1355 cm^{-1} (C-N) stretch, 1600-1618 cm^{-1} (C=C) stretch and 3535-3650 cm^{-1} (N-H) stretch. The C-H wagging bands of PPY closely overlaps the corresponding bands of PDC from the metal complexes in the composites, occurring as multiple sharp bands in the region 800-950 cm^{-1}. Evidence of the metal complexes in the composites was confirmed as small distinct peaks appeared in each of their spectra: 1700-1734 cm^{-1} (C=O) stretch, 1600-1635 cm^{-1} (C=N) stretch, 1400-1458 cm^{-1} (C=C) stretch, 3181-3584 cm^{-1} (O-H) stretch as well as the metal-O and metal-N bands occurring at 458-508 cm^{-1} are well in agreement with the peaks of their free metal complexes. There is an overall increase in (C=O) and (C=N) stretching bands of the composites when compared to its respective metal complex. This could arise due to the influence of (C=N) bonds from both PDC (N-pyridyl) and PPY (N-pyrrole).

4.1.3 PPY/metal–PDC film composites

In a similar manner, the FTIR spectra of the film composites were compared with the original metal complexes and pure PPY film. The characteristic peaks of the important functional groups of the metal complex and PPY within the composites are identified and summarized in **Table 4.3** and stacked in **Appendix C**. The important peaks of the free PPY doped *p*-TSO as synthesized include 1271 cm^{-1} (C-N^{+}) stretch, 1643 cm^{-1} (C=C) stretch, and 1004-959 cm^{-1} (=C-H) wagging which is associated with ring deformation of the radical cations (Tian et al., 2020; Liao et al., 2017a; Vera et al., 2014)). The characteristic peak of the doped *p*-TSO is identified by the sharp peaks at 1122-1077 cm^{-1} which is assigned to the O=S=O stretching vibrations (Tian et al., 2020; Liao et al., 2017b). The peaks observed in the present work matched close to the ones available in literature, hence confirming the formation of PPY doped *p*-TSO film.

Identifying peaks of the PPY in the composites can be found around 1280 cm^{-1} (C-N^{+}) stretch), 1645 cm^{-1} (C=C) stretch and 995-955 cm^{-1} (=C-H) wagging. Evidence of the metal complexes in the composites was also confirmed as small distinct peaks appeared in each of their spectra around 1700 cm^{-1} (C=O) stretch, 1510 cm^{-1} (C=N) stretch, 1430-1499 cm^{-1} (C=C) stretch, 3022-3177 cm^{-1} (O-H) stretch of carboxyl group. Moreover, the metal-O and metal-N bands occurring at 451-579 cm^{-1} region for the composites are in good agreement with the peaks of their respective complexes.

4.1.4 Conclusion

The characteristic peaks of the important functional groups of PDC, metal-N and metal-O are identified for all metal–PDC complexes. The results in this work are in agreement with existing literature and also supported by its crystal structure data. This helped to easily identify the characteristic peaks for the PPY/metal–PDC composites and distinguish the peaks from pure PPY.

Table 4.1: Assignment of characteristic bands from FTIR Spectral data of PDC and its metal complexes

Assigned functional group	**Wavelength (cm^{-1})**				
	PDC	**AgPDC**	**CdPDC**	**CuPDC**	**ZnPDC**
$\nu(C=O)$	1693 s	1729 m	1692 s	1673 m	1692 s
$\nu_{as}(COO^-)$	1574 m	1583 m	1614 w 1574 w	1648 w 1596 m	1595 w 1574 m
$\nu_s(COO^-)$	1328 w	1302 m	1396 w 1373 m	1332 m 1311 m	1330 w 1293 m
$\Delta\nu(COO^-) = \nu_{as}(COO^-) - \nu_s(COO^-)$	246	281	218 201	316 285	265 281
$\nu(O\text{-}H)$	2620 b 2829 b	3297 b	3405 b	3498 b	3068 b
$\nu(C=N)$	1456 m	1545 w	1470 w	1471 w	1455 m
$\nu(C=C)$	1412 m	1451 w	1460 w	1427 w	1413 m
$\delta(C\text{-}H)$	749 s	760 m	766 s	769 m	764 s
ν(Metal-O) ν(Metal-N)	-	533 w 469 w	535 m 467 w	459 w 575 m	516 w 458 w

ν=stretching, ν_s=symmetric stretching, ν_{as}=asymmetric stretching, δ=bending; s=sharp, m=medium, b=broad, w=weak

Table 4.2: Assignment of important bands from FTIR spectral data of PPY/metal–PDC powder composites

Powder composites	**Obtained absorption signals for assigned vibrations (cm^{-1})**									
	PDC groups						**PPY groups**			
	***v*(C=O)**	***v*(C=N)**	***v*(C=C)**	***v*(O-H)**	***v* (Metal-O)**	***v* (Metal-N)**	***v*(C=N)**	***v*(C-N)**	***v*(C=C)**	***v*(N-H)**
PPY	-	-	-	-	-	-	1680	1300	1577	3514
PPY-AgPDC	1732 m	1635 w	1458 w	3259 w	502 m	470 m	1644 w	1335 w	1600 w	3535 w
PPY-CdPDC	1717 m	1600 w	1456 w	3260 m	575 w	499 w	1636 w	1354 w	1617 w	3524 b
PPY-CuPDC	1734 m	1602 w	1457 w	3534 w	478 w	577 w	1636 w	1355 w	1600 w	3650 w
PPY-ZnPDC	1700 m	1618 m	1400 w	3181 b	508 w	458 w	1618 m	1300 b	1618 m	3575 w

v=stretching; s=sharp, m=medium, b=broad, w=weak

Table 4.3: Assignment of important bands from FTIR spectral data of PPY/metal–PDC film composites

Film composites	**Obtained absorption signals for assigned vibrations (cm^{-1})**									
	PDC groups						**PPY groups**			***p*-TSO group**
	***v*(C=O)**	***v*(C=N)**	***v*(C=C)**	***v*(O-H)**	***v*(Metal-O)**	***v*(Metal-N)**	***ω*(=C-H)**	***v*(C-N$^+$)**	***v*(C=C)**	***v*(O=S=O)**
PPY	-	-	-	-	-	-	1004 s 959 w	1271 w	1643 m	1122 b 1077 b
PPY-AgPDC	1700 w	1522 b	1436 b	3177 b	510 w	475 w	993 m 953 w	1282 m	1642 b	1110 b 1078 b
PPY-CdPDC	1700 w	1523 b	1499 b	3054 b	559 w	461 w	999 m 953 w	1284 w	1648 b	1124 w 1081 b
PPY-CuPDC	1701 b	1499 b	1431 b	3022 b	462 w	579 w	992 m 956 w	1273 m	1649 b	1110 m 1081 b
PPY-ZnPDC	1700 b	1524 b	1435 w	3084 b	500 w	451 w	992 m 955 w	1288 w	1645 b	1114 m 1080 b

v=stretching, *ω*=wagging; w = weak; m = medium; b = broad; s = sharp

4.2 XRD studies

4.2.1 Metal complexes

[Ag($C_7H_4NO_4$)($C_7H_5NO_4$)].2H_2O : PXRD pattern (blue) and single crystal pattern (red) of synthesized AgPDC are shown in **Figure 4.10 (a).** The PXRD peaks are in good agreement with the single crystal peaks thus the sharp peaks confirmed the crystal structure of AgPDC and justified that it had been successfully prepared under current synthetic conditions. The crystal parameters of synthesized AgPDC also match very well with the previously reported structure (Wang et al., 2004) (CCDC-248754). The Ag^+ atom in the crystal structure has a distorted tetrahedral coordination geometry with two bidentate PDCs in a *trans* arrangement and the planar ligands are almost perpendicular to each other. The asymmetric unit of AgPDC is shown in **Figure 4.6**. The bond length of Ag1– N1/N2 (2.326(3) Å, 2.325(3) Å) is shorter than Ag1–O1/O2 (2.505(3) Å, 2.507(3) Å). This difference is reflected in the FTIR as well and suggested stronger Ag-N interactions. It has a triclinic crystal system and PLATON study on its structure revealed that its unit cell contained no accessible void and hence, no pores. This also confirms that AgPDC is a metal complex. The complexes are linked to each other *via* symmetric O—H···O bonds of water molecules extending to form a stable 3D network.

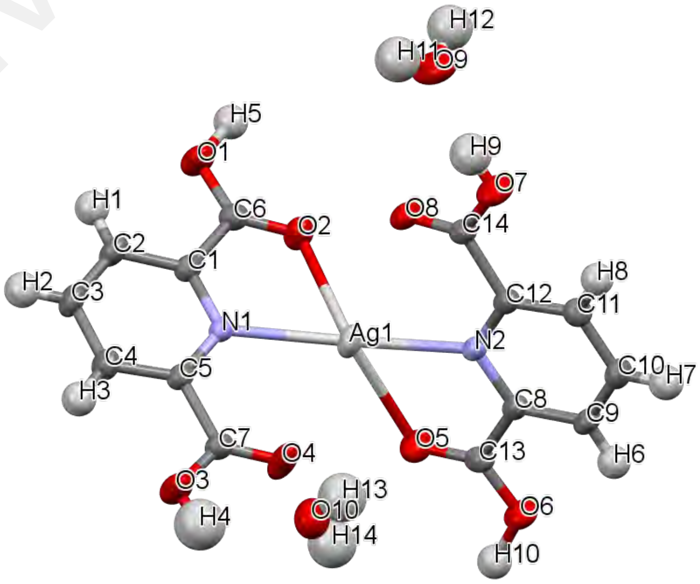

Figure 4.6: A view of AgPDC showing the labelled atoms with the thermal ellipsoids at 50% probability level.

$[Cd(C_7H_3NO_4)(3H_2O)].C_7H_5NO_4$: Figure 4.10 (b) shows the PXRD pattern of synthesized CdPDC approximately matching with the pattern from its single crystal diffraction. There is slight difference in the intensity of some peaks which may be due to the preferred orientation of atoms in the crystal structure and powder samples. A view of the molecular structure of CdPDC obtained from its single crystal is shown in **Figure 4.7.** CdPDC is a new unreported crystal that crystallizes in a monoclinic system with $P2_1/c$ space group. Within the asymmetric unit, the crystal consists of one Cd(II) atom coordinated to three water molecules, two ligands in tridentate and monodentate manner respectively forming a pentagonal bipyramidal geometry together with one free PDC. The free PDC molecule is hydrogen bonded to one coordinated water molecule via intermolecular hydrogen bond of O-H···N perpendicular to the ab crystallographic axis, thereby extending the structure into a 2-D network along this axis. The bond length of Cd1–N1 is 2.321(2) and for Cd1–O1/O4 is 2.475(2) Å, 2.398(2) Å. The single crystal parameters of this new CdPDC coordination complex obtained in this study are summarized in **Appendix D.**

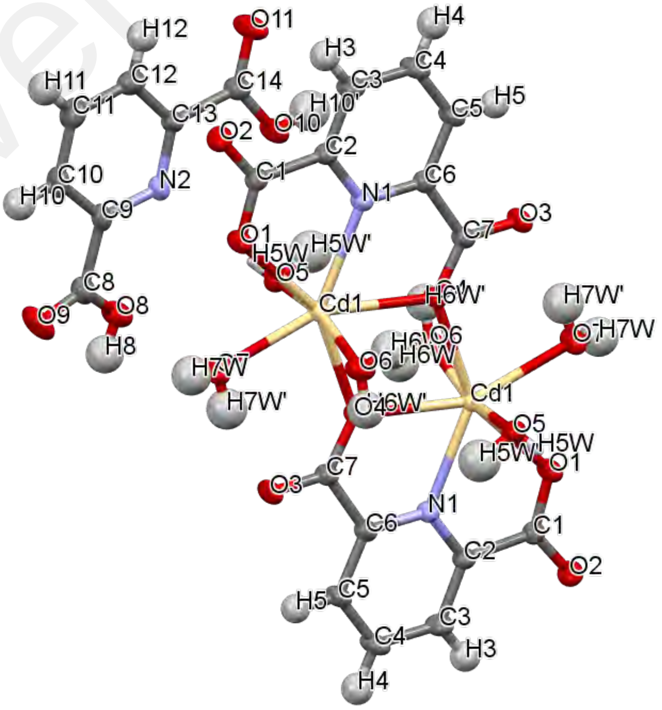

Figure 4.7: A view of CdPDC showing the labelled atoms with the thermal ellipsoids at 50% probability level.

$[Cu(C_7H_5NO_4)(C_7H_3NO_4)].3H_2O$: Figure 4.6 (c) compares the PXRD and single crystal patterns of CuPDC and their sharp peaks are well in agreement with each other proving that the single crystal is the representative of the bulk of CuPDC. Single crystal reveals that Cu(II) crystallizes in an orthorhombic system coordinated with two ligands where one is deprotonated dianion and the other is neutral. This different behavior of the ligands to the metal is suggested to be as a result of Jahn-Teller effect by the d^9 electronic configuration of Cu(II) (Okabe & Oya, 2000). The single crystal parameters of the synthesized CuPDC match very well with the previously reported structure (CCDC-1936104). A view of the molecular structure of CuPDC obtained from its single crystal is shown in **Figure 4.8.** PLATON study on its crystal unit cell reveals the absence of any pores in the structure. This 1:2 complex has a distorted octahedral geometry about the metal centers where each Cu(II) ion is bonded to four oxygen atoms and two N-pyridyl atoms from the two tridentate ligand molecules. The bond lengths of Cu-N are 1.910(4)-1.996(5) Å and Cu-O are 2.028(5)-2.458(4) Å. The crystal structure is stabilized by O–H···O intermolecular hydrogen bonds between the complex and three water molecules.

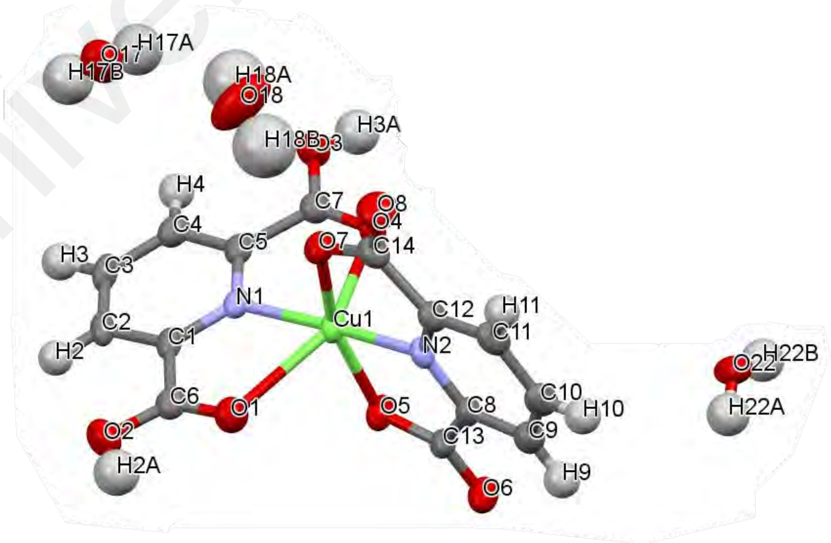

Figure 4.8: A view of CuPDC showing the labelled atoms with the thermal ellipsoids at 50% probability level.

$[Zn(C_7H_3NO_4)_2].3H_2O$: The PXRD and single crystal patterns of ZnPDC are compared in **Figure 4.10 (d)**. It can be seen that the peaks closely match each other, however there are two different peak intensities of single crystal observed at 2θ=11 and 2θ=28° which may arise from the preferred placement of the atoms in a specific plane in the crystal structure. The single crystal parameters of ZnPDC at present work are very similar to previously reported structures (CCDC-143229). A view of the molecular structure of ZnPDC obtained from its single crystal is shown in **Figure 4.9.** According to single crystal, Zn(II) metal ion is bonded to four O atoms and two N-pyridyl atoms from two ligand molecules with a distorted octahedral geometry in a monoclinic system with $P2_1/a$ space group. The two ligands in the Zn(II) are partially deprotonated, as identical monoanions which are nearly perpendicular to each other, and the complex is stabilized by O–H···O intermolecular hydrogen bonds between the complex and the water molecules. In the zinc coordination environment, the bond distance of Zn-N is shorter than Zn-O, however the FTIR shows higher vibrational peaks of Zn-O because of the coordination of Zn with four O atoms. The result of PLATON study on the crystal structure of ZnPDC reveals that its unit cell contains no solvent accessible void, confirming that ZnPDC is a metal complex instead of a MOF.

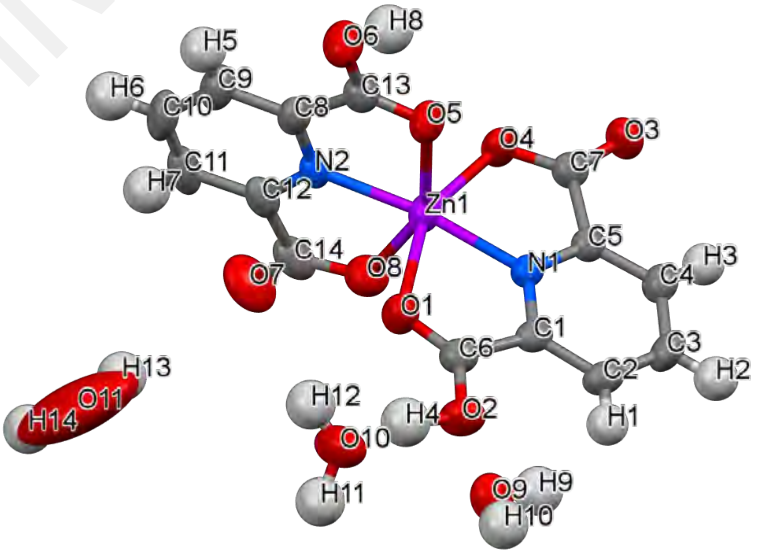

Figure 4.9: A view of ZnPDC showing the labelled atoms with the thermal ellipsoids at 50% probability level.

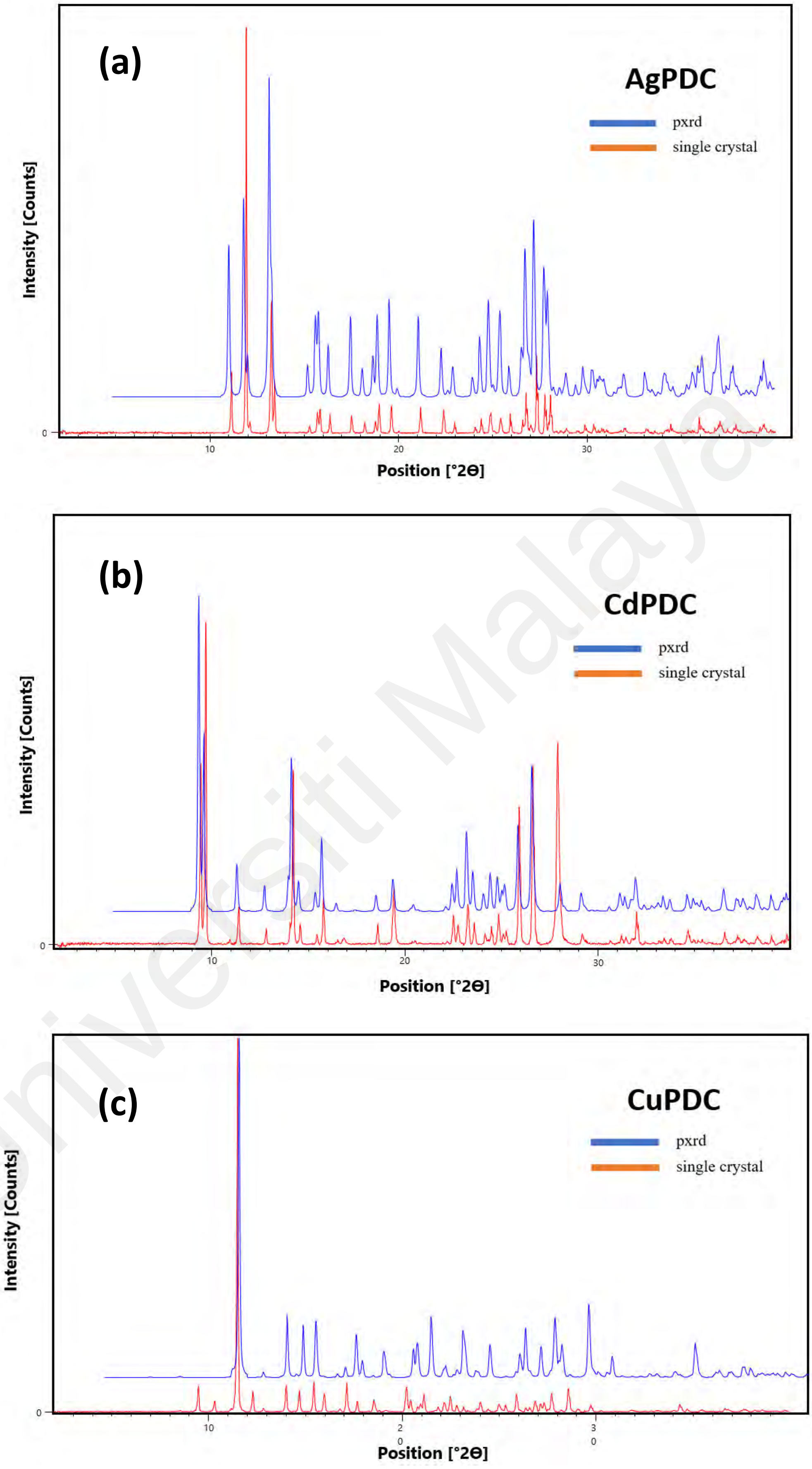

Figure 4.10: Stacked PXRD and single crystal peaks of all metal-PDC complexes (a) AgPDC, (b) CdPDC, (c) CuPDC and (d) ZnPDC.

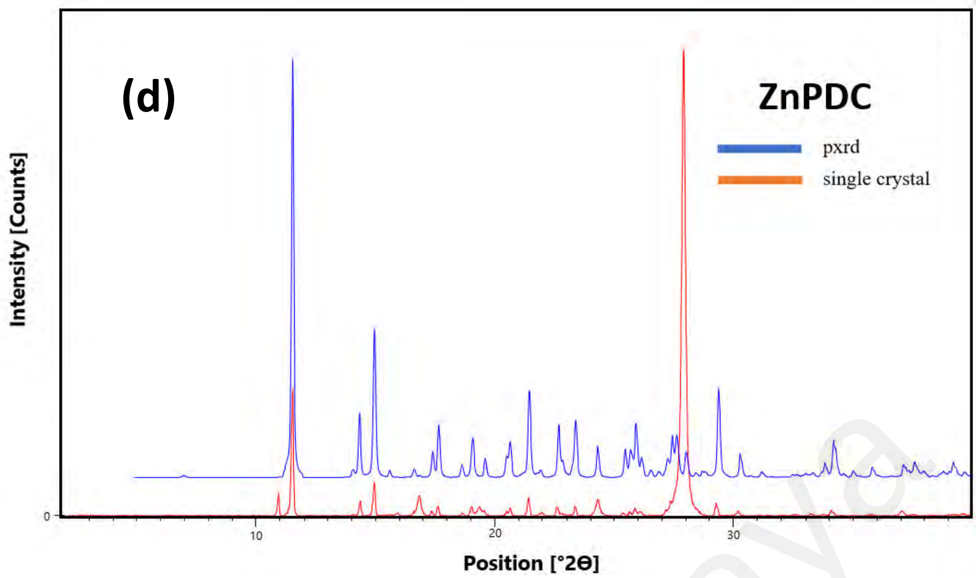

Figure 4.10, continued.

4.2.2 PPY/metal–PDC film composites

PXRD peaks of pure PPY is observed to be generally amorphous with low degree of crystallinity (**Figure 4.11**). The peaks observed in PPY and its composites consist of broad reflection peaks, indicating that the composite materials are dominated by the interplanary space scattering of the PPY chains. Specifically, broad peaks in the region of 2θ = 20°-25° is associated with the amorphous nature of the polymer and the XRD result here is in agreement with the literature (Yussuf et al., 2018; Yuan et al., 2016). It is suggested that PPY would be interconnected via secondary H bonds with the PDC of the metal complex (Arvas et al. 2022). According to literature, it is expected that H bonds were formed between the N atoms of the partially positively charged PPY chain and the carboxyl ends of PDC ligand during polymerization.

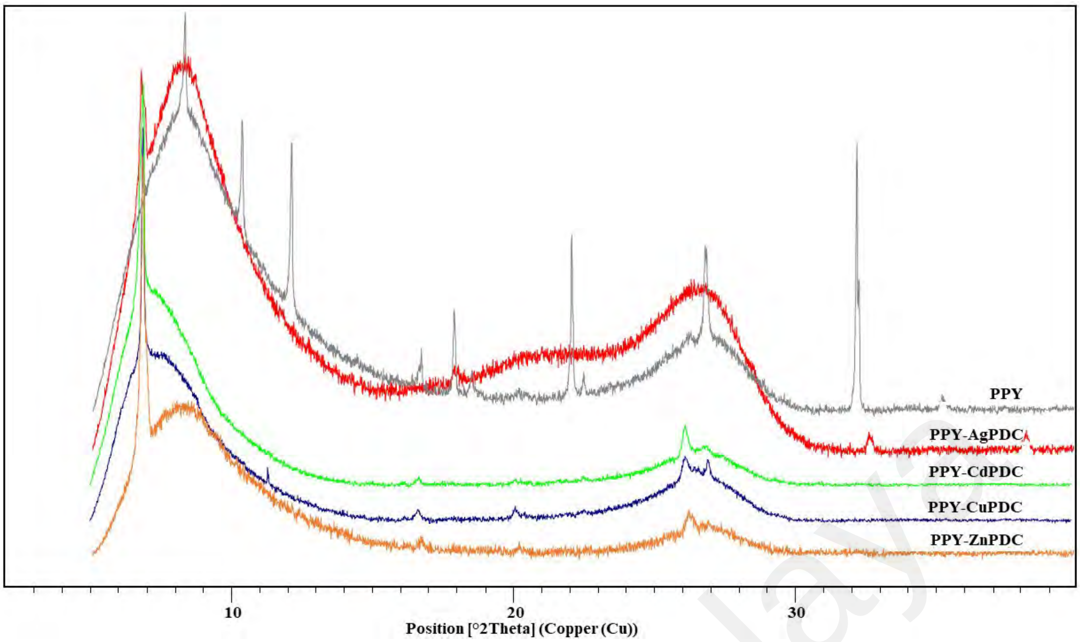

Figure 4.11: PXRD patterns of PPY and PPY/metal–PDC film composites.

4.2.3 Conclusion

The crystal parameters of synthesized AgPDC, CuPDC and ZnPDC match very closely with the previously reported structures (CCDC-248754, CCDC-1936104 and CCDC-143229 respectively) as well as its PXRD patterns**,** confirming that single crystals are the representative of the bulk materials. CdPDC in this work has been identified as a new unreported structure and its crystal structure has been deposited in crystal structure database (CCDC-2250637). The coordination environments as per crystal studies of the PDC ligand with each metal are in agreement with the structure suggested by FTIR analysis. The PXRD patterns of the composites suggest that the films are amorphous in nature.

4.3 FESEM analysis

FESEM images were taken to visually analyze the surface morphology and determine the elemental composition of the complexes and composites. Each of the complexes were obtained in distinct crystal forms after synthesis. Specifically, AgPDC crystals exhibited a colourless prismatic structure, CuPDC displayed a blue-coloured pillar-like crystalline structure, while ZnPDC appeared as white pillar-like crystals. CdPDC crystals are white and irregularly block shaped, identified as a new crystal structure, which is discussed in this work. **Figure 4.12** shows the microstructures of metal–PDC complexes obtained at >60,000 magnifications. Since the metal–PDC complexes were grinded to fine powder prior to characterization, the surfaces of the all complexes are observed to be fairly irregular.

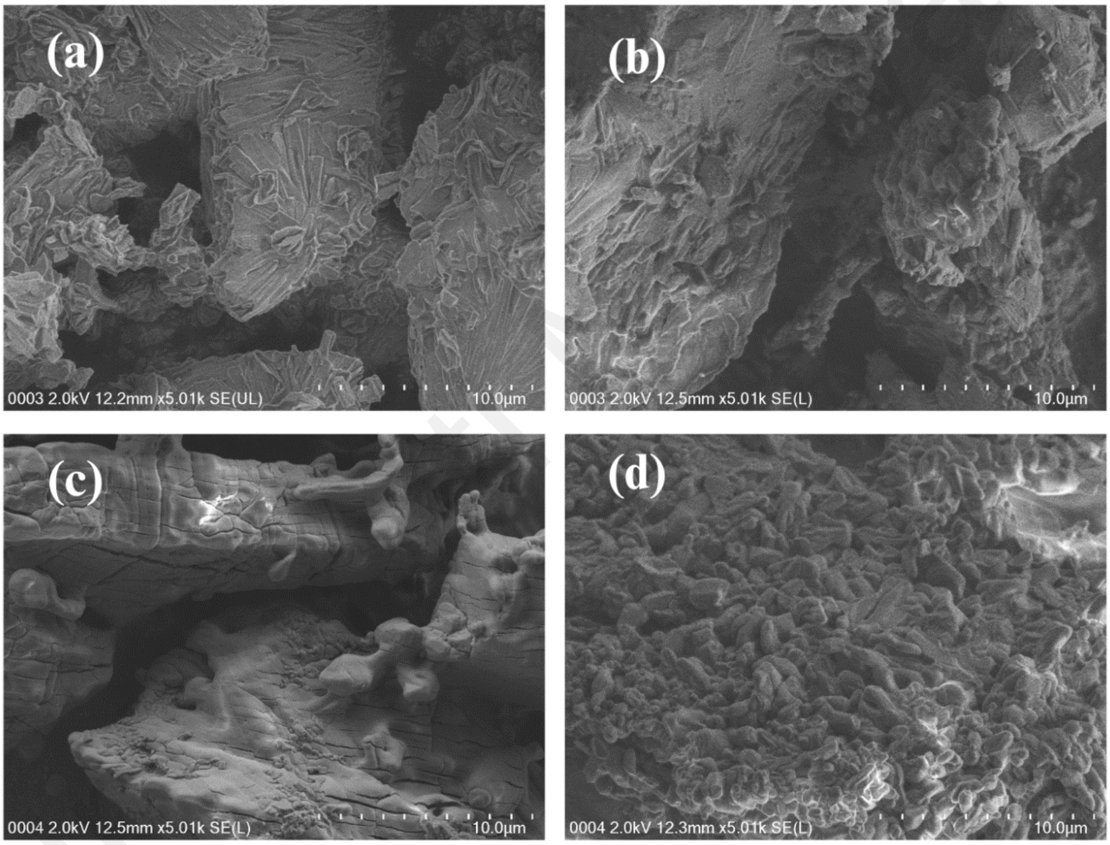

Figure 4.12: FESEM images of metal–PDC complexes (a) AgPDC, (b) CdPDC, (c) CuPDC and (d) ZnPDC.

Once the metal complexes are combined with PPY, they become physically indistinguishable from each other as all the composites turn into black in appearance which is characteristic color of PPY. **Figure 4.13** shows the FESEM images obtained for its powder and film form. PPY powder sample shows uniform microspherical morphology with the microstructures having an average diameter of 0.5 µm (**Figure 4.13 (a))**. Meanwhile, PPY film sample comprised of the characteristic microspherical structures with an average diameter of 2.4 µm in a uniform packed order, indicating aggregation of PPY (**Figure 4.13 (b))** (Wang et al., 2015; Liao et al., 2017).

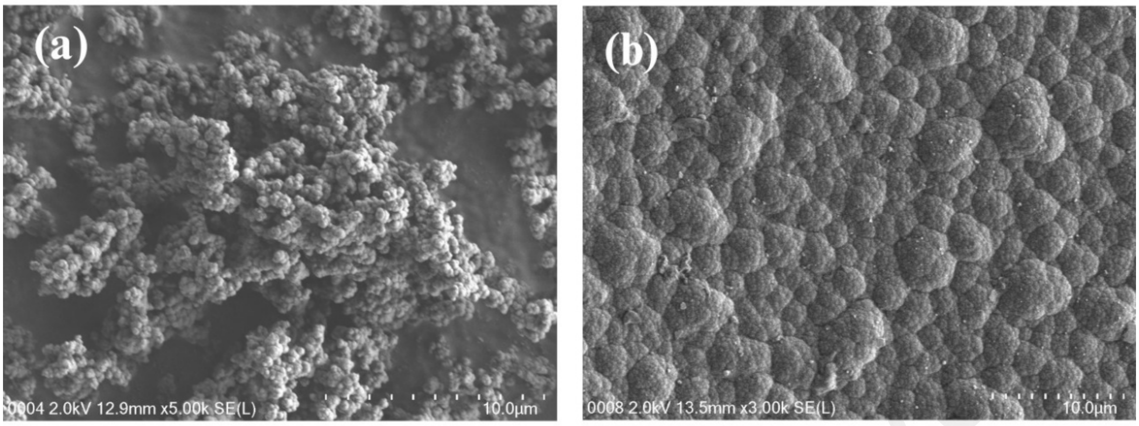

Figure 4.13: FESEM images of PPY (a) powder and (b) film.

When the powder composites are compared to their free metal complexes, the presence of PPY is identified by the distinctive globular structures as captured by FESEM. **Figure 4.14** shows the microstructures of all the powder composites. PPY is seen to cover over the structure of AgPDC in the PPY-AgPDC powder sample (**Figure 4.14 (a)**). Although the structure of other complexes was not distinctively observed in its composite powder, the presence of the metals was confirmed by EDX. These images suggest that the metal complexes were encapsulated by the microspheres of PPY. PPY can serve as a hinge to interconnect the complexes, facilitating the electron transport (Wang et al., 2018).

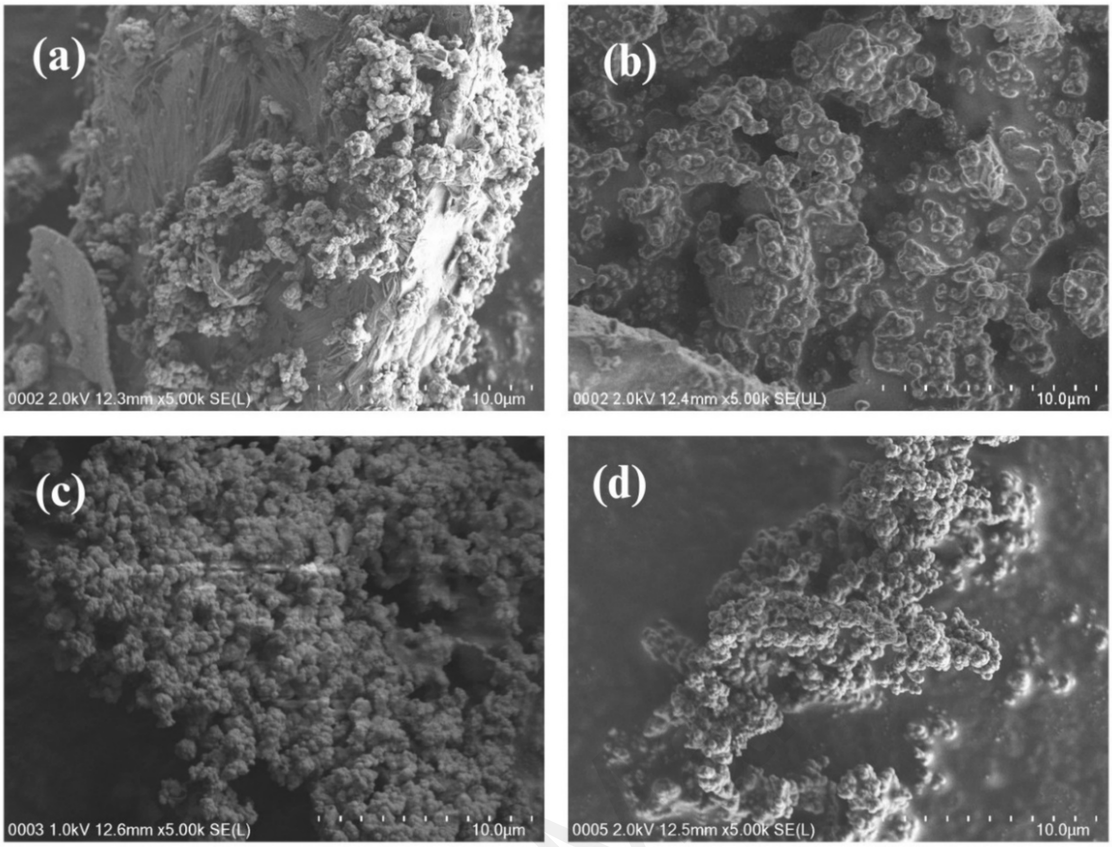

Figure 4.14: FESEM images of PPY/metal–PDC powder composites (a) PPY-AgPDC, (b) PPY-CdPDC, (c) PPY-CuPDC and (d) PPY-ZnPDC.

Meanwhile, in the FESEM captured images of the film composites, they were seen to possess uneven structures of corresponding metal complexes embedded and distributed non-uniformly within the microspheres of PPY **(Figure 4.15**). The images were captured at >65,000 magnifications. The average size of the PPY microspheres seen within the film composites is 1.2 µm. The length of the metal complex within the film composites in the selected images range from 1.11-2.66 µm (AgPDC), 1.17-1.75µm (CdPDC), 0.98-1.89 µm (CuPDC) and 1.10 µm (ZnPDC). The corrugated surface morphology of the PPY microspheres is necessary for integrating the active materials onto the film (Kaiser et al., 2019). All the composite films showed valleys upon which the metal–PDC complex were accommodated. The conducting metals in the composite can mediate the electron hopping within the conjugated backbone of PPY chains while the PDC in the composite can act as spacers to avoid the PPY films from restacking (Gan et al., 2015).

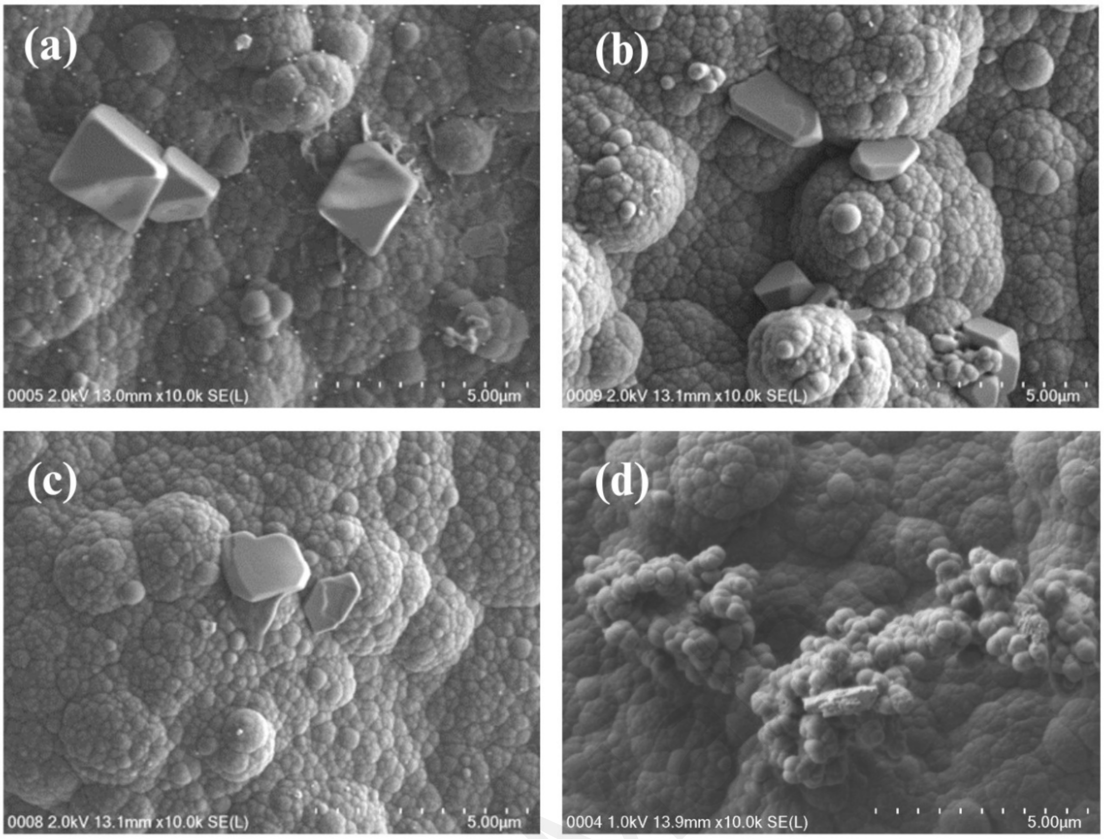

Figure 4.15: FESEM images of PPY/metal–PDC film composites (a) PPY-AgPDC, (b) PPY-CdPDC, (c) PPY-CuPDC and (d) PPY-ZnPDC.

Thus, it can be seen that the morphological changes of the PPY composites are influenced by the different synthesis methods which also influence the conductivity of the materials. The particle sizes of PPY within the powder and film composites are seen to decrease compared to pure PPY due to increase in nucleation size during its polymerization process (Sutar et al., 2019). For both the powder and film composites, the characteristic amorphous nature of PPY is observed (Wang et al., 2015). Although the crystallinity of the metal complex in the composites (as inferred by XRD) is lost, the amorphous PPY composites can exhibit good thermal conductivity (Chougule et al., 2011).

4.4 EDX analysis

The atomic composition with standard deviation (SD) of complexes, powder composites and film composites with regards to the metals they contained are listed in **Table 4.4, Table 4.5** and **Table 4.6** respectively.

C, N and O correspond to the atoms for PDC in the complexes. The experimental atomic composition of the metal complexes as shown in **Table 4.4** is closely in agreement with the theoretical data. The presence of metal also confirmed the successful formation of the complex structure.

Since all the metals were also detected in their respective PPY-composites, it indicated that the metal complexes were successfully introduced and combined into their composites with PPY. There is a significant amount of carbon, oxygen and nitrogen which are attributed to both the organic ligand and PPY in the composites. Meanwhile, the S in the film composites is accounted for the presence of sulphur in the dopant *p*-TSO.

It is noteworthy to mention that the nitrogen signal was not obtained for CdPDC and PPY-CdPDC powder sample. Furthermore, the nitrogen percentage obtained for PPY-CdPDC film sample is very less (0.08%) as can be seen in **Table 4.6**. The signal for nitrogen from the pyrrole rings and pyridyl ligand that was not identified could be due to the obscuration of its signal by the abundant carbon and oxygen present in the organic PDC and PPY in the sample (Patterson et al., 2020). In comparison to other samples, carbon percentage in cadmium samples is the highest. This abundance of carbon is likely to mask the appearance of nitrogen in the sample.

Table 4.4: Atomic composition of metal–PDC complexes obtained from EDX

Complex	**Atomic composition**							
	C		**N**		**O**		**Metal**	
	At%	**SD**	**At%**	**SD**	**At%**	**SD**	**At%**	**SD**
AgPDC	46.15	3.27	16.42	5.06	34.23	2.12	3.20	0.26
CdPDC	64.24	2.93	-	-	46.87	1.19	1.59	0.90
CuPDC	48.43	0.86	20.35	0.59	28.26	0.27	2.95	0.04
ZnPDC	37.27	0.89	31.99	4.22	30.48	3.01	0.25	0.32

Table 4.5: Atomic composition of PPY and PPY/metal–PDC powder composites obtained from EDX

Powder	Atomic composition							
	C		N		O		Metal	
	At%	SD	At%	SD	At%	SD	At%	SD
PPY	58.86	1.67	21.99	1.23	19.15	0.62	-	-
PPY-AgPDC	55.40	0.98	11.25	0.59	30.27	3.10	3.09	1.52
PPY-CdPDC	73.82	1.08	-	-	25.89	1.05	0.28	0.14
PPY-CuPDC	52.08	9.66	25.99	6.98	21.85	2.57	0.08	0.12
PPY-ZnPDC	59.57	2.19	23.77	0.92	16.63	1.27	0.04	0.01

Table 4.6: Atomic composition of PPY and PPY/metal–PDC film composites obtained from EDX

Film	Atomic composition									
	C		N		O		S		Metal	
	At%	SD	At%	SD	At%	SD	At%	SD	At%	SD
PPY	67.92	0.75	17.36	0.27	11.23	0.57	3.49	0.19	-	-
PPY-AgPDC	68.94	2.65	12.17	2.68	15.04	1.23	3.80	0.36	0.05	0.04
PPY-CdPDC	83.42	0.79	0.08	0.06	11.48	0.13	4.27	0.17	0.02	0.01
PPY-CuPDC	67.88	1.06	16.95	1.11	11.90	0.15	3.24	0.15	0.07	0.04
PPY-ZnPDC	57.15	0.36	25.48	1.16	15.05	0.50	2.32	0.40	0.05	0.02

4.5 TGA studies

4.5.1 Metal complexes

The results of TGA for all the metal complexes are compiled in **Table 4.7** and the curves are stacked in **Figure 4.16**. The TGA was recorded at temperature range of 30°C-600°C. The thermal decomposition of the organic PDC ligand in the complexes is observed to occur by at most two steps. Initially there is a common weight loss near 100°C which is attributed to evaporation of the water molecules present and/or coordinated to the metal complexes. Thereafter, rapid weight loss for the decomposition of the coordinated ligand is seen at 150-530°C.

For AgPDC, the early weight loss at 65-165°C is due to the removal of two water molecules, followed by degradation of two PDC units at temperatures 165-280°C leaving silver oxide residues. This result is in good agreement with the calculated theoretical percentages, XRD, as well as the previously reported literature (Etaiw & El-bendary, 2018).

CdPDC loses three water molecules at a much higher range (108-195°C) which can be due to increased bond strength as a consequence of coordination with the metal center (further confirmed from XRD results). Hereafter, two step degradation occurs where two PDC units are removed at 195-530°C leaving behind 24.9% (calc. 22.6%) cadmium metal oxide as residue. This result is close in agreement with the theoretical values and XRD study.

CuPDC is seen to have one small weight loss of water molecules prior to the one step rapid degradation at 150-310°C with weight loss of 66.2% (calc. 65%). This is attributed to the partial decomposition of the two coordinated PDC molecules. The observed 21.8% of the residue above 310°C is close with the calculated residual loss of copper oxides (23.4%). This observation corresponds with the XRD characterization of the structure and matches closely with previously reported literature (Demir et al., 2017).

For ZnPDC, complete removal of three water molecules and two coordinated PDC is seen at 93-100 °C and 100-291°C respectively leaving behind with only 16.7% (calc. 15%) residue of zinc oxide. The experimental values are in agreement with the theoretical values, literature (Kremer & Englert, 2019) as well as the structure determined from XRD studies.

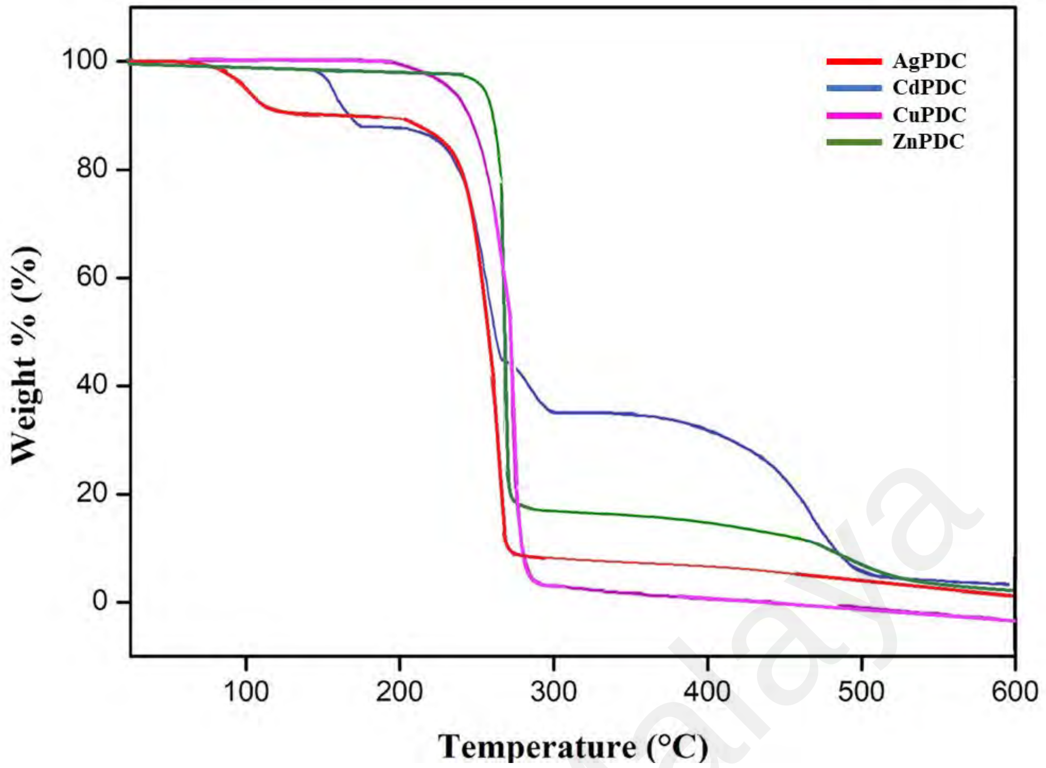

Figure 4.16: TGA curves of metal-PDC complexes.

Table 4.7 TGA analysis for metal-PDC complexes

Complex	Decomposition range		Moiety lost	Remaining weight (%) Obs. (Calc.)	Expected residue
	Temperature range (°C)	Weight loss (%)			
		Obs. (Calc.)			
AgPDC	65.0 – 165.0 165.0 – 280.0	7.5 (7.5) 59.6 (59.1)	H_2O PDC	32.9 (33.4)	Silver oxide
CdPDC	108.0 – 195.0 195.0 – 530.0	9.8 (10.8) 65.3 (67.1)	H_2O PDC	24.9 (22.1)	Cadmium oxide
CuPDC	85.0 - 100.0 150.0 - 310.0	12.0 (12.0) 66.2 (64.6)	H_2O PDC	21.8 (23.4)	Copper oxides
ZnPDC	93.1 – 100.3 100.3 – 291.3	2.3 (3.9) 81.0 (81.1)	H_2O PDC	16.7 (15.0)	Zinc oxide

4.5.2 PPY/metal–PDC powder composites

To validate the presence of PPY in the PPY-metal complex composite samples, TGA analysis was done at temperature range of 30-600°C. The TGA curves of all powder composites with pure PPY have been compiled for comparison in **Figure 4.17** and summarized in **Table 4.8**. the DTG curves are provided in **Appendix F**.

The initial weight loss that is observed to occur approximately from 60-180°C for pure PPY sample is attributed to the evaporation of water molecules and possible low-molecular weight impurities in the sample. The main weight loss starting around 180°C till 360°C is associated to the degradation of the pyrrolic backbone. Similar PPY synthesized with ammonium persulfate has also been reported to thermally degrade around 187°C which is in agreement with the TGA and DTG observation here (Yussuf et al., 2018). This range is also comparable with several other reported literatures where degradation of PPY is observed from 190°C (Jakab et al., 2007; Bose et al., 2010). The remaining 9.5% residue could be the remains of any inorganic impurities.

All the composites show similar initial weight loss around 60-190°C which could be associated with both the loss of water molecules coordinated within their respective metal complex and absorbed moisture. From 180°C-190°C onwards, the degradation of the PPY chains and partial degradation of PDC is expected. This is a common trend for all the composites and the temperature closely reflects the observed degradation range of pure PPY in the present study as well as reported degradation temperature for PPY (Yussuf et al., 2018). Final degradation of PDC units of the complexes within the composites is expected from 360°C onwards and this range is agreeable as it is correlated with the range seen from its respective metal complexes. The residual content after 600°C is expected to be the inorganic metal oxides as the percentages obtained is higher than pure PPY. Since the observed final residues of all the PPY powder composites are more than that of pure PPY (9.5%), it can be said that the PPY /metal-PDC composites prepared by chemical oxidation have improved thermal stability (Su, 2015).

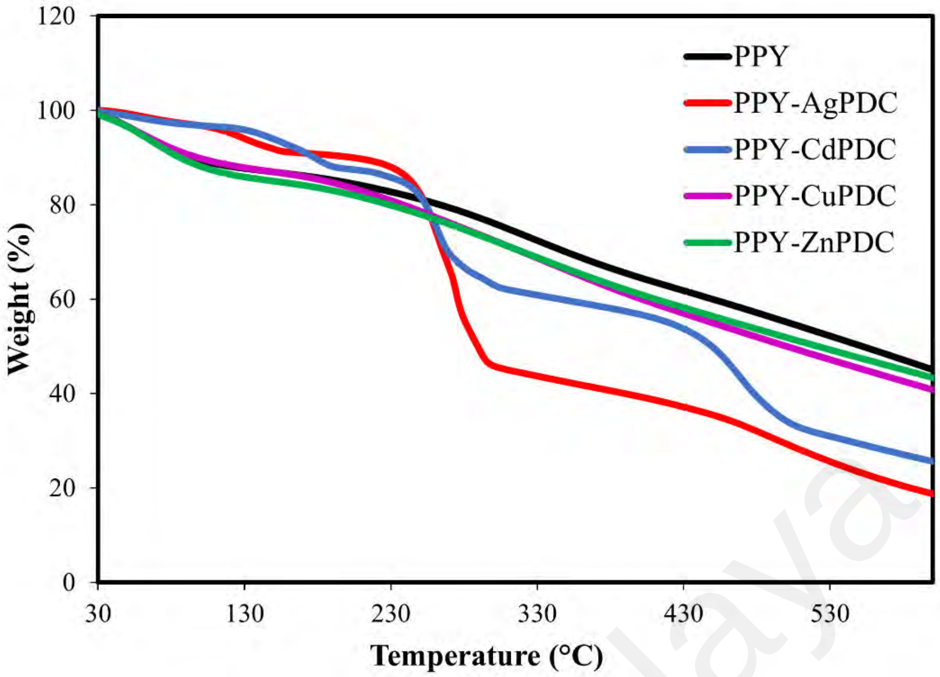

Figure 4.17: TGA curves of PPY and PPY/metal-PDC powder composites.

Table 4.8: TGA analysis for PPY and PPY/metal–PDC powder composites

Sample	Decomposition range (°C)	Weight loss (%)	Moiety lost	Residue (%)	Expected residue
PPY	60.0 – 180.0 180.0 – 360.0	12.7 77.8	H_2O PPY	9.5	Inorganic impurity
PPY-AgPDC	90.0 –181.0 181.0 – 363.0 363.0 – 542.0	9.3 49.0 17.4	H_2O PPY PDC	24.3	Silver oxides
PPY-CdPDC	95.0 – 192.0 192.0 – 363.0 363.0 – 542.6	12.1 28.9 29.0	H_2O PPY PDC	30.0	Cadmium oxides
PPY-CuPDC	70.0 – 180.0 180.0 – 363.0 363.0 – 541.9	14.6 20.8 18.3	H_2O PPY PDC	46.3	Copper oxides
PPY-ZnPDC	74.0 – 180.0 180.0 – 385.0 385.0 – 542.0	16.4 20.9 14.3	H_2O PPY PDC	48.4	Zinc oxides

4.5.3 PPY/metal–PDC film composites

PPY and all its film composites show a one-step degradation process (**Figure 4.18**). In the initial temperature of 25-179°C PPY is seen to be stable as inferred by the straight line of the thermogram which also suggested that there was little to no moisture absorbed in the sample film prior analysis. At temperatures beyond 180°C, a rapid degradation of the polymer chains occurs with 30.7% weight loss leaving behind 69.2% residual weight at 600°C. All the composites show slightly increased thermal stability till around 200°C followed by rapid weight loss (see **Table 4.9**) leaving around 65% residue at 600°C. The weight loss from 200-600°C in the composites could be associated with both the loss of PPY and *p*-TSO including the PDC units and this range is agreeable as it is correlated with the range seen from its respective metal complexes, leaving behind metal oxides as residue. The slight delay of thermal degradation of PPY in the composites is due to the overall increase in molecular weight of the composites with the integration of metal complexes (Kumar et al., 2014) and have slightly improved thermal stability. It is important to acknowledge the influence of PPY integration on the residual content of metal oxides. Indeed, the presence of PPY can impact the decomposition temperature of PDC and the formation of metal oxides. However, it is also worth noting that the content of the metal in both the metal-PDC and PPY/metal-PDC materials remains consistent (Khan et al., 2009).

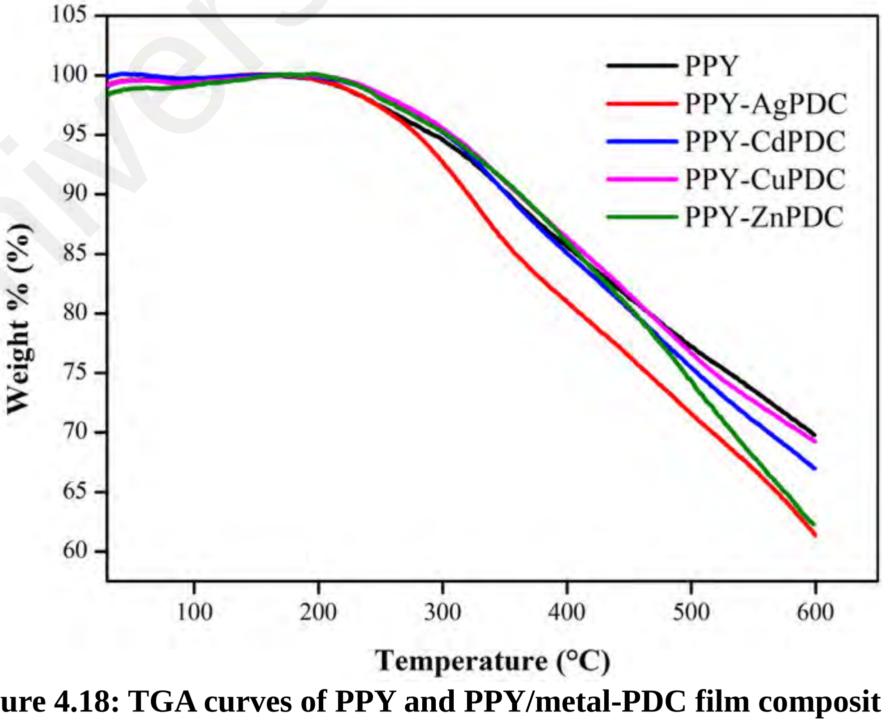

Figure 4.18: TGA curves of PPY and PPY/metal-PDC film composites.

Table 4.9: TGA analysis for PPY and PPY/metal–PDC film composites

Sample	Decomposition range (°C)	Weight loss (%)	Moiety lost	Residue (%)	Expected residue
PPY	180.0 – 600.0	30.7	PPY	69.2	Inorganic impurity
PPY-AgPDC	194.0 – 599.0	39	PPY, PDC	61	Silver oxides
PPY-CdPDC	195.0 – 600.0	32.4	PPY, PDC	67.5	Cadmium oxides
PPY-CuPDC	205.0 – 600.0	30.9	PPY, PDC	69.0	Copper oxides
PPY-ZnPDC	199.0 – 599.0	38.2	PPY, PDC	61.7	Zinc oxides

4.5.4 Conclusion

The thermal stability of metal–PDC complexes, powder and film composites were discussed in detail. The result of the TGA analysis of the metal–PDC complexes are supported by theoretical calculations, XRD studies and existing literatures. Both the powder and film composites of PPY/metal–PDC are suggested to have slightly improved thermal stability compared to pure PPY.

4.6 CV analysis

4.6.1 PPY/metal–PDC powder composites

The electrochemical performance of PPY and PPY/metal-PDC powder composites was evaluated by obtaining its CV in a three-electrode cell at room temperature. The powder samples were initially combined with carbon black and PVDF to create a viscous slurry which was then coated evenly over a graphite sheet that acted as current collector for the working electrode. The choice of electrolyte for CV is crucial to consider as the electrode material should not be soluble in it, hence 1 M H_2SO_4 was chosen as PPY is known to be insoluble in acid electrolytes (Yogeeshwari et al., 2020). **Figure 4.19** shows the CV curves of the samples obtained at scan rate of 10 mV.s^{-1} and potential range of -0.2 V to +0.8 V.

The voltammograms obtained for all the composite samples showed a near quasi-rectangular shape similar to pure PPY. However, there are some noticeable differences. Firstly, all composites exhibited higher current density response with larger integrated polygon area than PPY. This is indicative of good capacitive charge-storage behaviour (Yu et al., 2019).

Interestingly, PPY-AgPDC composite electrode showed an unique pair of redox peaks. A small oxidation peak is observed at +0.4 V and a broad reduction peak occurred at +0.25 V and these are in attributed to the oxidation of Ag/Ag^+ and reduction of Ag^+/Ag respectively. This observation is also in good agreement with other PPY/Ag based electrodes in H_2SO_4 electrolyte (Gan et al., 2015; Gupta et al., 2015). The result suggests that silver in the PPY-AgPDC composite is additonally influencing a redox behaviour in the capacitive performance.

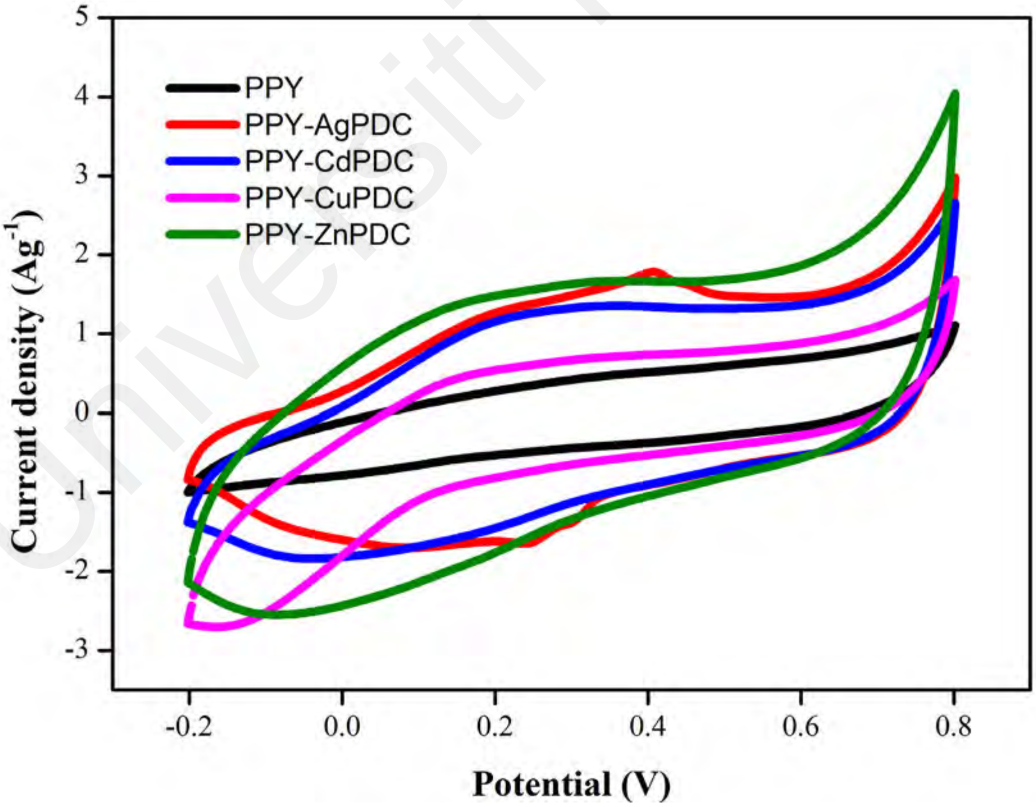

Figure 4.19: CV comparison of PPY and PPY/metal–PDC powder composites as slurry-coated graphite sheet electrode (WE) with Pt wire (CE) and Ag/AgCl (RE) in 1 M H_2SO_4 obtained at scan rate of 10 mV.s^{-1}.

4.6.2 PPY/metal–PDC film composites

The electrochemical performance of PPY and PPY/metal-PDC film composites was studied by obtaining its CV in a similar three-electrode cell at room temperature. The ITO glass containing the deposited film acted as current collector for the working electrode. In this set up, a redox active electrolyte was incorporated with a neutral salt in order to enhance the charge-transfer process. **Figure 4.20** shows the CV curves of the samples obtained at scan rate of 10 mV.s^{-1} and potential range of -0.5 V to +0.9 V.

The CV for all the composite electrodes revealed a broader pair of redox peaks with higher current response and slightly larger integral area compared to pure PPY film. The redox peaks arise from the faradaic redox reaction of $Fe(CN)_6$ in the electrolyte solution and the mechanism is shown in **Equation [4.1]** (Ramachandran et al., 2018):

$$[Fe(CN)_6]^{4-} \rightleftharpoons [Fe(CN)_6]^{3-} + e^- \qquad \textbf{[4.1]}$$

The reaction is proposed in **Equation [4.2]** where upon charging with positive potential scan, both the anion $[Fe(CN)_6]^{4-}$ in the electrolyte and the neutral PPY undergoes oxidation and the oxidized $[Fe(CN)_6]^{3-}$ would have been incorporated in the positively charged polymer matrix. The process is reversed upon discharging with negative potential scan, where the cation K^+ in the solution might have diffused with PPY while $[Fe(CN)_6]^{3-}$ leaves the polymer as it gets reduced back into the solution by gaining an electron. The anodic and cathodic peaks of the composites related to the redox couple $[Fe(CN)_6]^{3-/4-}$ with higher current response are actively influencing better electron transfer, *i.e.* suggesting an increase in pseudo-capacitance compared to pure PPY. The redox process of the composites is similarly proposed to follow **Equation [4.3].**

$$[(pyrrole^+|\,TSO^-)^0_n\,K^+ + \;n[Fe(CN)_6]^{4-} \;\rightleftharpoons\; [(pyrrole^+|\,TSO^-)^+_n\,[Fe(CN)_6]^{3-} + ne^- + \;K^+ \textbf{[4.2]}$$

$$[(pyrrole^+|\,TSO^-|\,m^+ - PDC^-)^0_n\,K^+ + \;n[Fe(CN)_6]^{4-} \rightleftharpoons\; [(pyrrole^+|TSO^-|m^+ - PDC^-)^+_n\,[Fe(CN)_6]^{3-} + ne^- + \;K^+ \qquad \textbf{[4.3]}$$

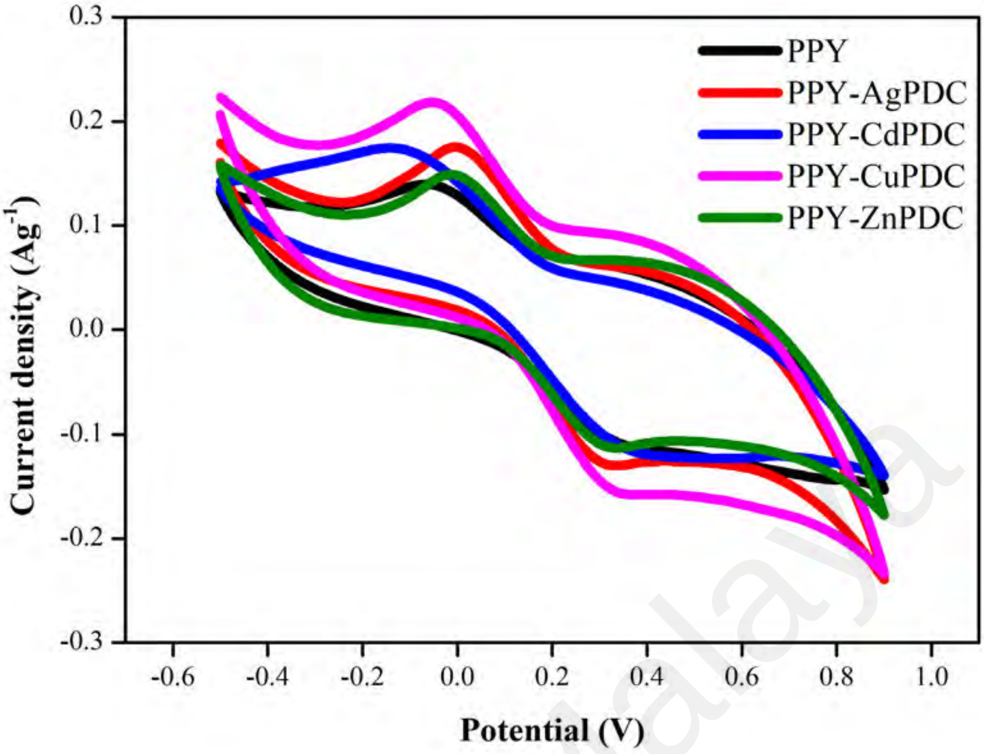

Figure 4.20: CV comparison of PPY doped with *p*-TSO and its PPY/metal-PDC film composites on ITO glass (WE), graphite rod (CE) and Ag/AgCl (RE) at scan rate of 10 mVs^{-1} in 0.01 M $K_3[Fe(CN)_6]$ + 0.1 M KCl solution

4.6.3 Conclusion

Therefore, it was seen that the PPY/metal-PDC powder composites exhibited capacitive behaviour and PPY/metal-PDC film composites exhibited redox pseudo-capacitance depending on the electrolytes used at fixed scan rate of 10 mV.s^{-1}. In both cases, all the composites showed improved performance compared to pure PPY. Based on our knowledge, this is a new study concerning composite films of metal-PDC complexes with PPY, hence additional research on this topic is required for further optimization of the materials and methods that utilizes its electrochemical properties for energy storage.

4.7 EIS studies

EIS was performed to study the frequency independent DC conductive properties of the composite materials. The Nyquist impedance plots of PPY and its composites are presented in **Figure 4.21** and **Figure 4.22,** where Z_r (Ω) represents the real and Z_i (Ω) represents the imaginary parts of complex impedance (Z^*) plotted in response to different frequencies. The DC conductivity of the electrodes (σ_{dc}) was calculated using **Equation [4.4]**:

$$\sigma_{dc} = \frac{1}{R_b} \times \frac{t}{A} \qquad \textbf{[4.4]}$$

where t is the thickness of the sample, A is the surface area of the electrode material and R_b is the bulk resistance of the active material (Abdulwahid et al. 2021). R_b was obtained from the starting intercept of the impedance curve on Z_r axis at the high frequency region of the Nyquist plot (Abdul Halim et al., 2021; Yao et al., 2018). The obtained values from the Nyquist plots are also presented and compared.

4.7.1 PPY/metal–PDC powder composites

The EIS of PPY and its powder composites as slurry-coated graphite sheets were recorded in the frequency of 0.1 Hz to 100 kHz after its CV using the same three-electrode cell set up performed in 1 M H_2SO_4. This frequency range was chosen similar to the range chosen by Arvas et al. (2022) for PPY-PDC in 1M H_2SO_4 electrolyte solution. The average thickness of the sample was measured by subtracting the thickness of the graphite sheet before and after mass loading.

The first intercept of the semicircle in the Z_r axis represents R_b (also termed as equivalent series resistance) which determines the total resistance between the electrolyte, current collector and the active material (Gan et al., 2015). The estimated diameter of this semicircle represents the charge transfer resistance (R_{ct}), while the oblique line with a 45° angle beyond the arc in low frequency is known as Warburg region which indicates a nearly ideal capacitive behaviour (Laschuk et al., 2021; P Mahore et al., 2018). In general, the semicircles in the high to medium frequency is associated with charge transfer process at the electrode-electrolyte interface and the sloped line in low frequency is attributed to ion-diffusion process at the interfacial region (Sultana et al., 2012).

Figure 4.21 presents the Nyquist plots of all the samples. It can be seen that the Nyquist plots of all the samples consist of a small arc in the high frequency region followed by a sloped line in the low frequency region. The data obtained from **Figure 4.21** is compiled in **Table 4.10**. The R_{ct} values of all the composites are smaller than pure PPY ($< 0.58\ \Omega$). This suggests that the composites have better kinetic properties due to faster charge transfer. A linear increase of the sloped line in the low frequency region was due to good capacitive behaviour of the electrodes which was also observed from the CV analysis. This observation is also in agreement with the reported porous PPY-PDC electrode in H_2SO_4 (Arvas et al., 2022). In our case, the improved capacitance is achieved with the addition of metals in the composite electrode containing PDC and PPY.

The conductivity values that were determined from R_b are listed in **Table 4.10**. Pure PPY was found to have conductivity of 8.62×10^{-4} $S.cm^{-1}$. PPY prepared by oxidative polymerization have been previously reported to have conductivities within the range of $10^{-3} – 10^{-4}$ $S.cm^{-1}$ (Dave & Nerkar, 2021). It is observed that all composites revealed improved conductivity compared to pure PPY by one order of magnitude. PPY-CuPDC has the highest conductivity value, followed by PPY-CdPDC, PPY-AgPDC and PPY-ZnPDC.

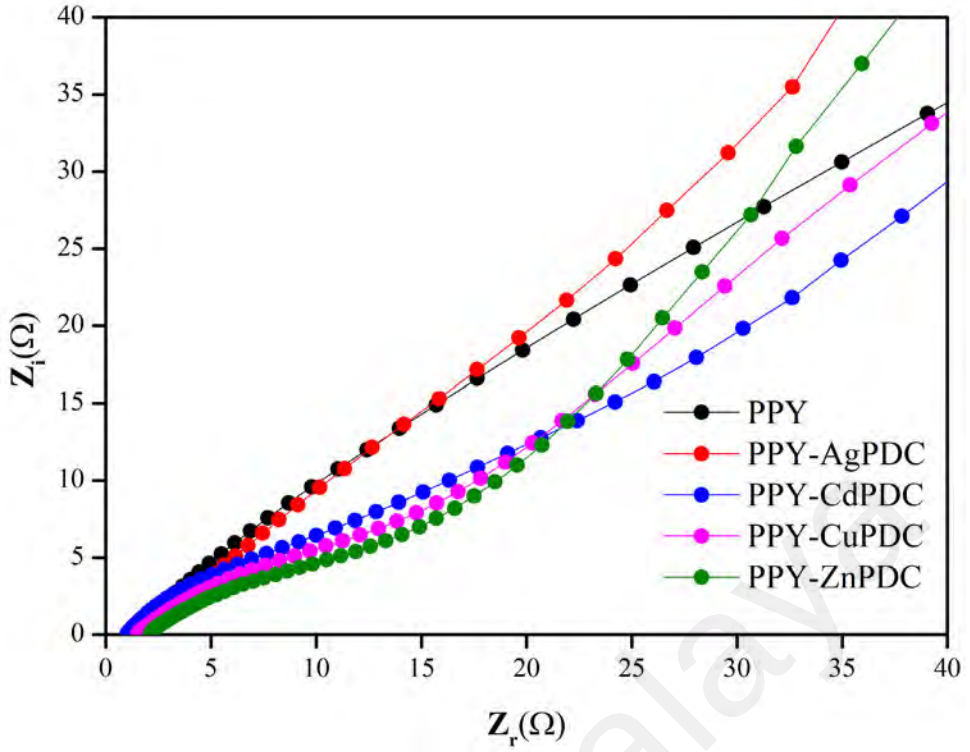

Figure 4.21: Nyquist plots of PPY and PPY/metal–PDC powder composites.

Table 4.10: Bulk resistance, charge transfer resistance and electrical conductivity of PPY and PPY/metal–PDC powder composites

Sample film	R_b (Ω)	R_{ct} (Ω)	Conductivity (S.cm^{-1})	
			σ_{dc}	**SD**
PPY	1.16	0.58	8.62×10^{-4}	0.21×10^{-4}
PPY-AgPDC	1.98	0.24	1.36×10^{-3}	0.15×10^{-3}
PPY-CdPDC	1.02	0.23	3.04×10^{-3}	0.74×10^{-3}
PPY-CuPDC	1.54	0.39	4.41×10^{-3}	0.55×10^{-3}
PPY-ZnPDC	2.12	0.47	1.03×10^{-3}	0.01×10^{-3}

4.7.2 PPY/metal–PDC film composites

The EIS of the films were performed in the frequency range of 40 Hz – 5 MHz in room temperature. The frequency range is typically based on the specific application, in this case a broader range was chosen for the impedance measurement of the dry films intended for general analysis (Abdulwahid et al., 2021; Megha et al., 2020). The films were simply sandwiched between the stainless-steel electrode holder as depicted in **Figure 3.7**. Since the films slowly loses its adhesion to the ITO surface when immersed in the electrolyte for prolonged period, this method was attempted to directly measure the impedance of the films without using an electrolyte. The thickness was initially measured from different sites of each film and then the average value taken into account for calculating the conductivity.

Nyquist plots of the films are compiled in **Figure 4.22**. The Nyquist plot of PPY film revealed a single incomplete semicircle whereas all the composites showed a single compressed curve. The impedance plot of the film composites appears as a sloping line instead of a straight line with a 45° slope, extending from the origin of the plot. This is known as finite Warburg plot. Referring to the nature of our materials, we believe that the diffusion-controlled or mass-transport-limits process in the electrochemical system was absent. Fundamentally, ions or charge carriers need time to diffuse through the electrolyte or the material being analysed, resulting in a Warburg element on the EIS plot which is not happening in our materials and lead to a finite Warburg plot (Lazanas & Prodromidis, 2023). This observation of the dry films is also comparable to Nyquist plots of PPY, PPY/Cu and PPY/Cu-ZnO composites whose impedance was measured in the form of pellets in 100 Hz – 5 MHz (Megha et al., 2020). According to this literature, the semicircle plot indicates absence of contact effects, bearing resemblance to a simple Debye model for non-interacting dipoles.

As seen in **Table 4.11,** all composites showed lowered bulk resistance and increased conductivities than pure PPY film. PPY-CdPDC was seen to exhibit the lowest R_b and highest conductivity followed by PPY-CuPDC, PPY-ZnPDC and PPY-AgPDC. Although the R_{ct} values are high, the intrinsic resistance of the composite films as represented by R_b is observed to be lower than PPY film. Hence, the conductivity of the films was slightly increased.

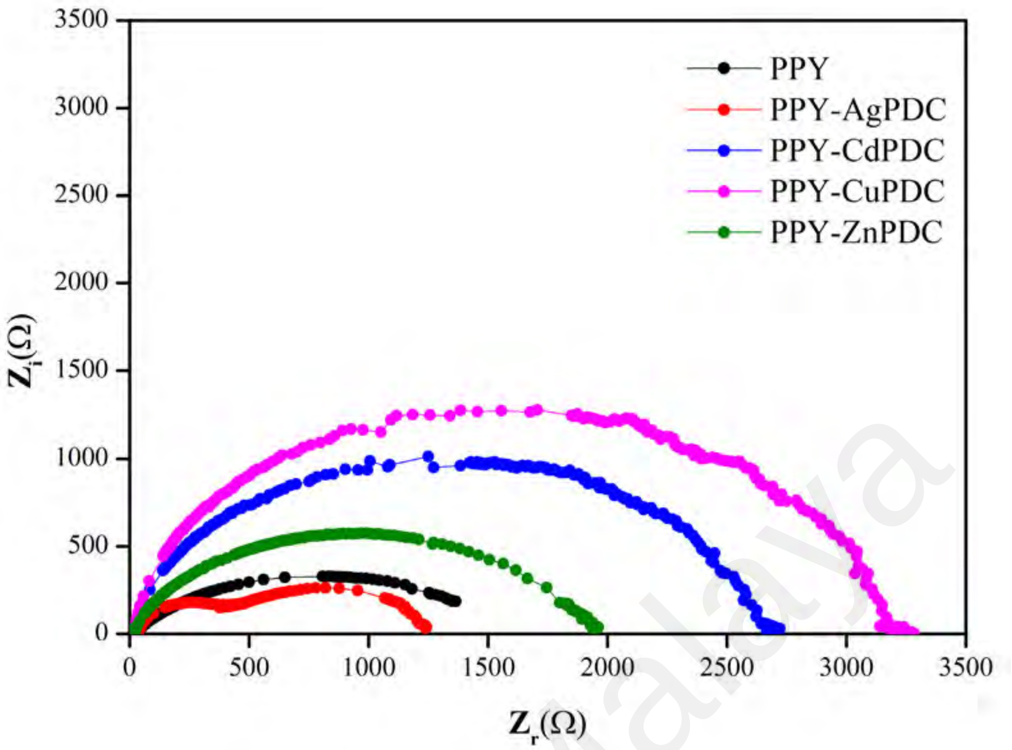

Figure 4.22: Nyquist plots of PPY and PPY/metal–PDC film composites.

Table 4.11: Bulk resistance, charge transfer resistance and electrical conductivity of PPY and PPY/metal–PDC film composites

Sample film	R_b (Ω)	R_{ct} (Ω)	Conductivity (S.cm^{-1})	
			σ_{dc}	SD
PPY	33.21	1633	1.04×10^{-5}	0.35×10^{-5}
PPY-AgPDC	31.55	1418	2.16×10^{-5}	0.14×10^{-5}
PPY-CdPDC	19.05	2570	4.78×10^{-5}	0.23×10^{-5}
PPY-CuPDC	20.92	3252	3.25×10^{-5}	0.07×10^{-5}
PPY-ZnPDC	20.98	1870	3.01×10^{-5}	0.08×10^{-5}

4.7.3 Comparisons

In short, both powder and film composites exhibited improved conductivity when compared with pure PPY. The powder composites as slurry coated electrodes have higher conductivity (~10^{-3} S.cm^{-1}) than the film composites (~10^{-5} S.cm^{-1}). A possible reason could be linked to the electrode set-up for impedance measurement. Since a three-electrochemical cell was used for the powder composites in the presence of an electrolyte, it allowed the interactions between the working electrode and electrolyte resulting in smaller R_{ct} values which did not happen for the dry films. **Table 4.12** lists the available conductivity values of few selected PPY based electrodes from literature. It can be observed that the conductivity of PPY powder composite in this work is in the same range with other PPY synthesized via chemical oxidative polymerization. Whereas the conductivity of PPY film composite is less by at most two orders of magnitude.

Good electrical conductivity of composite material is usually known to lead high energy storing ability and a promising candidate for energy storage devices (Gong et al. 2021; Yu et al. 2021). Clearly, these values indicate that the integration of PPY with each metal–PDC complexes has influenced and contributed to improved electrical and electrochemical conductivity compared to PPY of its own.

Table 4.12: Available conductivities of PPY based electrodes from literature

Material	**Polymerization method**	**Conductivity** ($S.cm^{-1}$)	**Reference**
PPY	Chemical oxidative ($FeCl_3$)	5.4×10^{-4}	Dave & Nerkar, 2021
PPY	Chemical oxidative ($FeCl_3$), *p*-TSO	3.1×10^{-2}	Song et al., 2016
PPY-Ag	Chemical oxidative ($FeCl_3.6H_2O$), immersion	1.1×10^{-4}	Škodová et al., 2013
PPY/ZCO	Chemical oxidative (APS)	1.8×10^{-3}	Sutar et al., 2019
SPVA/GO/ZnO-Nps/PPY	Chemical oxidative	1.6×10^{-3}	Mustafa et al., 2023
PPY-CuI	Chemical oxidative (APS)	1.7×10^{-3}	Singh et al., 2021
PPY	Electrochemical	3.7×10^{-3}	Rueda et al., 2020
PPY PPY-Ag	Electrochemical	1.4×10^{-4} 12.0×10^{-4}	García-Cabezón et al., 2023
PPY PPY-AgPDC	Chemical oxidative (APS)	8.62×10^{-4} 1.36×10^{-3}	This work
PPY PPY-AgPDC	Electrochemical	1.04×10^{-5} 2.16×10^{-5}	This work

4.8 Chapter summary

In summary, PPY based composites of four metal–PDC complexes were synthesized by chemical oxidation and electrochemical polymerization methods. All the complexes, powder composites, film composites and PPY were characterized via FTIR, PXRD, FESEM, EDX and TGA. FESEM studies showed different surface morphology for the powder and films. TGA analysis suggested slightly improved thermal stability of the composites compared to PPY. The electrochemical studies of PPY and composites were carried out by CV and EIS. For CV study performed at 10 mV.s^{-1} scan rate, the powder PPY and its composites were made as slurry coated graphite sheet electrodes in 1M H_2SO_4 electrolyte meanwhile, the PPY film and its composites deposited over ITO glass was directly used as working electrode in KCl+ $K_3[Fe(CN)_6]$ electrolyte solution. Powder composites showed enhanced capacitive behaviour whereas the film composites exhibited improved pseudocapacitive behaviour. The pseudocapacitive behaviour is associated with the redox couple of $[Fe(CN)_6]^{3-/4-}$. EIS study of the powder PPY and composites was carried out in the same electrochemical set up after its CV. EIS of the film PPY and composites was carried out by directly measuring the dry film. Both powder and film composites revealed improved conductivity values. This may be because of the decrease in inter-chain separation of PPY in the composites due to the formation of interfaces and interactions between PPY and metal–PDC complex through hydrogen bonding. As a result, it encouraged the charge carriers to travel longer distances at the interface causing it to increase in its conductivity and lead to exhibit synergistic effects between the metal–PDC and PPY (Megha et al., 2020). The specific metal ion within the composite plays a significant role in determining its electrical conductivity (Chatterjee et al., 2015). Different metal ions possess distinct electronic characteristics that impact their electron donation or acceptance abilities, thus influencing the overall electrical behaviour of the composite (Liu et al., 2016; Melot & Tarascon., 2013). Furthermore, the ligands that surround the metal ion can modify the electron distribution around the metal, consequently affecting its redox properties and rates of electron transfer (Evangelio & Ruiz-Molina, 2008). In our case, as we employ the same ligand in all composites, we expect that the net contribution remains consistent. Additionally, the three-dimensional arrangement of metal ions and ligands within the complex can influence conductivity. Structural factors such as coordination geometry, bond lengths, and symmetry play pivotal roles in shaping the pathways for electron transfer and, consequently, the material's capacity to conduct electricity (Shimazaki et al. 2009; Otero et al. 2017).

CHAPTER 5: CONCLUSION AND SUGGESTION FOR FUTURE WORK

5.1 Conclusion

This dissertation focuses on the potential of existing metal–PDC complexes as new PPY based composite electrode materials. In conclusion, all the objectives of the present study were achieved.

Metal-PDC complexes of Ag, Cd, Cu and Zn have been successfully synthesized via a facile method at room temperature and characterized for morphological and structural confirmation. The present synthesis method enabled to acquire unique pristine crystals of these metal-PDC complexes successfully. XRD studies of AgPDC, CuPDC and ZnPDC obtained at present study match very close to its respective reported structures. Obtained cadmium complex, CdPDC as [$(Cd(C_7H_3NO_4)(3H_2O)).C_7H_5NO_4$] has been identified as a new crystal structure by both PXRD and single crystal.

PPY and its composites were obtained at room temperature using two different methods: chemical oxidative (powder) and electrochemical polymerization (films). Chemical oxidative polymerization was done in the presence of APS and electrochemical polymerization was done with *p*-TSO dopant over ITO glass.

Composite analysis by FTIR, PXRD and FESEM, EDX and TGA made it possible to identify characteristic traits of individual components proving successful integration by current synthesis method. The results suggest that PPY might be connected to the metal complex via secondary H---H bonding forming the composites. Morphological studies of the powder composites suggested that PPY microspheres encapsulated the metal complexes. PXRD and morphological studies of the film composites revealed that the metal complexes were distributed irregularly within the microspheres of PPY. Observed electrochemical response of PPY and all its composites by CV revealed that at 10 mVs^{-1} scan rate, the composites can exhibit improved capacitance behaviour in 1 M H_2SO_4

analyte as well as improved pseudocapacitive behaviour in 0.1 M KCl + 0.01 M $K_3[Fe(CN)_6]$ analyte with larger integral area compared to pure PPY. Furthermore, impedance study of PPY and its composites as solid films was done to measure and compare the conductivities and electronic properties. The values obtained and determined from Nyquist plots indicate that all PPY/metal-PDC composites have achieved higher conductivity. The conductivity values determined for PPY powder slurry was 8.62×10^{-4} $S.cm^{-1}$ and for PPY film was 1.04×10^{-5} $S.cm^{-1}$. Powder composites exhibited increased conductivity in the range of $1.03 \times 10^{-3} – 4.41 \times 10^{-3}$ $S.cm^{-1}$ and film composites were in range of $4.78 \times 10^{-5} – 2.16 \times 10^{-5}$ $S.cm^{-1}$. Based on the current studies by CV and EIS, the enhanced electrochemical properties of PPY/metal-PDC composites are promising for potential supercapacitor application.

5.2 Suggestion for future work

In this work, powder PPY/metal–PDC composites as slurry coated graphite sheet electrodes showed better capacitive performance and higher conductivity. Further investigations on the electronic properties as well as energy storing capacity of these composites like long-term cycling stability, specific capacitance, energy, and power density can be determined by GCD method for conclusively evaluating their performance and utilization efficiency as new functional electrode materials. Besides, the conductivity may be improved additionally by optimizing the ratio of PPY and the metal–PDC complex.

REFERENCES

Abdul Halim, S. I., Chan, C. H., & Apotheker, J. (2021). Basics of teaching electrochemical impedance spectroscopy of electrolytes for ion-rechargeable batteries–part 1: a good practice on estimation of bulk resistance of solid polymer electrolytes. Chemistry Teacher International, 3(2), 105-115.

Abdulwahid, R. T., Aziz, S. B., Brza, M. A., Kadir, M. F. Z., Karim, W. O., Hamsan, H. M., ... & Dannoun, E. M. (2021). Electrochemical performance of polymer blend electrolytes based on chitosan: dextran: impedance, dielectric properties, and energy storage study. Journal of Materials Science: Materials in Electronics, 32, 14846-14862.

Ahmad, N., Sultana, S., Sabir, S., & Khan, M. Z. (2020). Exploring the visible light driven photocatalysis by reduced graphene oxide supported Ppy/CdS nanocomposites for the degradation of organic pollutants. *Journal of Photochemistry and Photobiology A: Chemistry, 386*, 112129.

Ali, A., Li, X., Song, J., Yang, S., Zhang, W., Zhang, Z., ... & Xu, X. (2017). Nature-mimic ZnO nanoflowers architecture: chalcogenide quantum dots coupling with ZnO/ZnTiO3 nanoheterostructures for efficient photoelectrochemical water splitting. The Journal of Physical Chemistry C, 121(39), 21096-21104.

Anwar, N., Asif, M., Shakoor, A., Niaz, N. A., Qasim, M., Irfan, M., ... & Mahmood, A. (2020). Electrical Properties and Characteristics of Polypyrrole Cadmium Oxide (PPy-CdO) Nanocomposite Schottky Diodes. *Polymer Science, Series A*, *62*(5), 543-549.

Arunkumar, M., & Paul, A. (2017). Importance of electrode preparation methodologies in supercapacitor applications. ACS omega, 2(11), 8039.

Arvas, M. B., Yazar, S., & Sahin, Y. (2022). The Synthesis of 2, 6-Pyridinedicarboxylic Acid Modified Porous Polypyrrole Electrodes and Its Energy Storage Application. *ECS Journal of Solid State Science and Technology*, *11*(11), 113006.

Ateh, D. D., Navsaria, H. A., & Vadgama, P. (2006). Polypyrrole-based conducting polymers and interactions with biological tissues. *Journal of the royal society interface*, *3*(11), 741-752.

Ates, M., Serin, M. A., Ekmen, I., & Ertas, Y. N. (2015). Supercapacitor behaviors of polyaniline/CuO, polypyrrole/CuO and PEDOT/CuO nanocomposites. *Polymer Bulletin*, *72*(10), 2573-2589.

Ay, B., Yildiz, E., & Kani, İ. (2018). Semiconducting lanthanide polymers of pyridine-2, 6-dicarboxylate: Hydrothermal synthesis, structural characterization, electrical conductivity and luminescence properties. *Polyhedron, 142*, 1-8.

Aydoğdu Tığ, G., Günendi, G., & Pekyardımcı, Ş. (2017). A selective sensor based on Au nanoparticles-graphene oxide-poly (2, 6-pyridinedicarboxylic acid) composite for simultaneous electrochemical determination of ascorbic acid, dopamine, and uric acid. *Journal of Applied Electrochemistry, 47*(5), 607-618.

Bach, M. L., & Gilvarg, C. (1966). Biosynthesis of dipicolinic acid in sporulating Bacillus megaterium. *Journal of Biological Chemistry*, *241*(19), 4563-4564.

Balint, R., Cassidy, N. J., & Cartmell, S. H. (2014). Conductive polymers: Towards a smart biomaterial for tissue engineering. *Acta biomaterialia*, *10*(6), 2341-2353.

Baratto, R. A., & Pezzin, S. H. (2022). One-pot synthesis of silver nanowires/polypyrrole nanocomposites. *Bulletin of Materials Science*, *45*(3), 138.

Bardini, Luca. (2015). EIS 101, an introduction to electrochemical spectroscopy. What was a website is now available as a self-contained PDF.

Batten, S. R., Champness, N. R., Chen, X. M., Garcia-Martinez, J., Kitagawa, S., Öhrström, L., ... & Reedijk, J. (2012). Coordination polymers, metal–organic frameworks and the need for terminology guidelines. *CrystEngComm*, *14*(9), 3001-3004.

Bhat, A. H. (2023). Fabrication of versatile Ag-P/Ppy core-shell nanocomposite: Adsorption efficacy for chromium (VI) removal and assessment of antioxidant and antibacterial activities. *Journal of Environmental Chemical Engineering*, *11*(5), 110664.

Bibi, A., & Shakoor, A. (2021). Electrical Properties and Characteristics of Polypyrrole/Cadmium Oxide for Thermoelectric Applications. *Polymer Science, Series A*, *63*(5), 585-590.

Bose, S., Kuila, T., Uddin, M. E., Kim, N. H., Lau, A. K., & Lee, J. H. (2010). In-situ synthesis and characterization of electrically conductive polypyrrole/graphene nanocomposites. *Polymer*, *51*(25), 5921-5928.

Cao, S., Yuan, R., Chai, Y., Zhang, L., Li, X., & Gao, F. (2007). A mediator-free amperometric hydrogen peroxide biosensor based on HRP immobilized on a nano-Au/poly 2, 6-pyridinediamine-coated electrode. *Bioprocess and biosystems engineering*, *30*(2), 71-78.

Chatterjee, S., Maiti, R., Saha, S. K., & Chakravorty, D. (2015). Enhancement of electrical conductivity in CoO-SiO2 nanoglasses and large magnetodielectric effect in ZnO-nanoglass composites. *Journal of Applied Physics*, *117*(17).

Chen, G. Z. (2013). Understanding supercapacitors based on nano-hybrid materials with interfacial conjugation. *Progress in Natural Science: Materials International*, *23*(3), 245-255.

Chen, T., Fan, Y., Wang, G., Yang, Q., & Yang, R. (2015). Rationally designed hierarchical ZnCo 2 O 4/polypyrrole nanostructures for high-performance supercapacitor electrodes. *Rsc Advances*, *5*(91), 74523-74530.

Chen, T., Zeng, W., Liu, Y., Yu, M., Huang, C., Shi, Z., ... & Wu, M. (2022). Cu-doped polypyrrole with multi-catalytic activities for sono-enhanced nanocatalytic tumor therapy. *Small*, *18*(29), 2202964.

Chen, Y., Lu, X., Lamaka, S. V., Ju, P., Blawert, C., Zhang, T., ... & Zheludkevich, M. L. (2020). Active protection of Mg alloy by composite PEO coating loaded with corrosion inhibitors. *Applied Surface Science*, *504*, 144462.

Choudhary, R. B., Ansari, S., & Majumder, M. (2021). Recent advances on redox active composites of metal-organic framework and conducting polymers as pseudocapacitor electrode material. *Renewable and Sustainable Energy Reviews*, *145*, 110854.

Chougule, M. A., Pawar, S. G., Godse, P. R., Mulik, R. N., Sen, S., & Patil, V. B. (2011). Synthesis and characterization of polypyrrole (ppy) thin films. *Soft Nanoscience Letters*, *01*(01), 6–10.

Chuhadiya, S., Suthar, D., Patel, S. L., & Dhaka, M. S. (2021). Metal organic frameworks as hybrid porous materials for energy storage and conversion devices: A review. *Coordination Chemistry Reviews*, *446*, 214115.

Cui, L., Ai, S., Shang, K., Meng, X., & Wang, C. (2011). Electrochemical determination of NADH using a glassy carbon electrode modified with Fe3O4 nanoparticles and poly-2, 6-pyridinedicarboxylic acid, and its application to the determination of antioxidant capacity. *Microchimica Acta*, *174*(1), 31-39.

Cui, L., Fu, Y., Liu, L., Jiang, J., Ding, Y., & Chen, L. (2021). Alkali metal–lanthanide co-encapsulated 19-tungsto-2-selenate derivative and its electrochemical detection of uric acid. *Inorganic Chemistry Communications*, *130*, 108734.

Dave, N. V., & Nerkar, D. M. (2021). The influence of the oxidant on structural and morphological properties of conductive polypyrrole. *Materials Today: Proceedings*, *45*, 5939-5943.

Decker, G. E., Lorzing, G. R., Deegan, M. M., & Bloch, E. D. (2020). MOF-mimetic molecules: Carboxylate-based supramolecular complexes as molecular metal–organic framework analogues. *Journal of Materials Chemistry A*, *8*(8), 4217-4229.

Demir, S., Çepni, H. M., Hołyńska, M., Kavanoz, M., Yilmaz, F., & Zorlu, Y. (2017). Copper (II) complexes with pyridine-2, 6-dicarboxylic acid from the oxidation of copper (I) iodide. *Journal of Coordination Chemistry*, *70*(19), 3422-3433.

Derikvand, Z., Dorosti, N., Hassanzadeh, F., Shokrollahi, A., Mohammadpour, Z., & Azadbakht, A. (2012). Three new supramolecular compounds of copper (II), cobalt (II) and zirconium (IV) with pyridine-2, 6-dicarboxylate and 3, 4-diaminopyridine: Solid and solution states studies. *Polyhedron*, *43*(1), 140-152.

Du, J., Yang, H., Wang, C. L., & Zhan, S. Z. (2021). A nickel (II) complex of 2, 6-pyridinedicarboxylic acid ion, an efficient electro-catalyst for both hydrogen evolution and oxidation. *Molecular Catalysis*, *516*, 111947.

Dubal, D. P., Ayyad, O., Ruiz, V., & Gomez-Romero, P. (2015). Hybrid energy storage: the merging of battery and supercapacitor chemistries. *Chemical Society Reviews*, *44*(7), 1777-1790.

Ebadi, S. V., Semnani, D., Fashandi, H., & Rezaei, B. (2019). Synthesis and characterization of a novel polyurethane/polypyrrole-p-toluenesulfonate (PU/PPy-pTS) electroactive nanofibrous bending actuator. Polymers for Advanced Technologies, 30(9), 2261-2274.

Ensafi, A. A., Moosavifard, S. E., Rezaei, B., & Kaverlavani, S. K. (2018). Engineering onion-like nanoporous CuCo 2 O 4 hollow spheres derived from bimetal–organic frameworks for high-performance asymmetric supercapacitors. *Journal of Materials Chemistry A*, *6*(22), 10497-10506.

Espinet, P., Miguel, J. A., García-Granda, S., & Miguel, D. (1996). Palladium complexes with the tridentate dianionic ligand pyridine-2, 6-dicarboxylate, dipic. Crystal structure of [Pd (dipic)(PBu3)] 2. *Inorganic chemistry*, *35*(8), 2287-2291.

Etaiw, S. E. D. H., & El-bendary, M. M. (2018). Hydrogen bonded 3D-network of silver and 2, 6-pyridinedicarboxylic acid complex: Structure and applications. *Journal of Molecular Structure*, *1173*, 7-16.

Evangelio, E., & Ruiz-Molina, D. (2008). Valence tautomerism: More actors than just electroactive ligands and metal ions. *Comptes Rendus Chimie*, *11*(10), 1137-1154.

Fan, W., Zhang, X., Kang, Z., Liu, X., & Sun, D. (2021). Isoreticular chemistry within metal–organic frameworks for gas storage and separation. *Coordination Chemistry Reviews*, *443*, 213968.

Fan, X., Zhong, C., Liu, J., Ding, J., Deng, Y., Han, X., ... & Zhang, J. (2022). Opportunities of Flexible and Portable Electrochemical Devices for Energy Storage: Expanding the Spotlight onto Semi-solid/Solid Electrolytes. *Chemical Reviews*.

Feng, L., Zhang, W., Wang, R., Xu, L., Li, D., Xiao, C., & Zhang, Y. (2020). Preparation of CuO@ PPy hybrid nanomaterials as high cyclic stability anode of lithium-ion battery. *Micro & Nano Letters*, *15*(7), 441-445.

Fleischmann, S., Mitchell, J. B., Wang, R., & Zhan, C. (2020). D.-e Jiang, V. Presser and V. Augustyn. *Chem. Rev*, *120*, 6738-6782.

Forouzandeh, P., Kumaravel, V., & Pillai, S. C. (2020). Electrode materials for supercapacitors: a review of recent advances. *Catalysts*, *10*(9), 969.

Gan, J. K., Lim, Y. S., Huang, N. M., & Lim, H. N. (2015). Hybrid silver nanoparticle/nanocluster-decorated polypyrrole for high-performance supercapacitors. *RSC advances*, *5*(92), 75442-75450.

García-Cabezón, C., Godinho, V., Pérez-González, C., Torres, Y., & Martín-Pedrosa, F. (2023). Electropolymerized polypyrrole silver nanocomposite coatings on porous Ti substrates with enhanced corrosion and antibacterial behavior for biomedical applications. *Materials Today Chemistry*, *29*, 101433.

Ghanbari, R., Ghorbani, S. R., Arabi, H., & Foroughi, J. (2018). The charge transport mechanisms in conducting polymer polypyrrole films and fibers. *Materials Research Express*, *5*(10), 105701.

Ghosh, S., Keshri, S. R., Bera, S., & Basu, R. N. (2020). Enhanced solar hydrogen generation using Cu–Cu2O integrated polypyrrole nanofibers as heterostructured catalysts. *International Journal of Hydrogen Energy*, *45*(11), 6159-6173.

Glaser, F., & Wenger, O. S. (2020). Recent progress in the development of transition-metal based photoredox catalysts. *Coordination chemistry reviews*, *405*, 213129.

Gong, X., Yang, Q., Zhi, C., & Lee, P. S. (2021). Stretchable energy storage devices: from materials and structural design to device assembly. *Advanced Energy Materials*, *11*(15), 2003308.

Gonzalez-Baró, A. C., Castellano, E. E., Piro, O. E., & Parajón-Costa, B. S. (2005). Synthesis, crystal structure and spectroscopic characterization of a novel bis (oxo-bridged) dinuclear vanadium (V)–dipicolinic acid complex. *Polyhedron*, *24*(1), 49-55.

Gopi, C. V. M., Vinodh, R., Sambasivam, S., Obaidat, I. M., & Kim, H. J. (2020). Recent progress of advanced energy storage materials for flexible and wearable supercapacitor: From design and development to applications. *Journal of energy storage*, *27*, 101035.

Guan, B. Y., Yu, X. Y., Wu, H. B., & Lou, X. W. (2017). Complex nanostructures from materials based on metal–organic frameworks for electrochemical energy storage and conversion. *Advanced materials*, *29*(47), 1703614.

Guo, Y., Zhang, S., Wang, J., Liu, Z., & Liu, Y. (2020). Facile preparation of high-performance cobalt–manganese layered double hydroxide/polypyrrole composite for battery-type asymmetric supercapacitors. *Journal of Alloys and Compounds*, *832*, 154899.

Gupta, R., Jayachandran, K., Gamare, J. S., Rajeshwari, B., Gupta, S. K., & Kamat, J. V. (2015). Novel electrochemical synthesis of polypyrrole/ag nanocomposite and its electrocatalytic performance towards hydrogen peroxide reduction. *Journal of Nanoparticles*, *2015*.

Hao, J., Peng, S., Li, H., Dang, S., Qin, T., Wen, Y., ... & Cao, G. (2018). A low crystallinity oxygen-vacancy-rich Co 3 O 4 cathode for high-performance flexible asymmetric supercapacitors. *Journal of Materials Chemistry A*, *6*(33), 16094-16100.

Hassanpoor, A., Mirzaei, M., Eshtiagh-Hosseini, H., & Majcher, A. (2018). Constructing two 1D coordination polymers and one mononuclear complex by pyrazine-and pyridinedicarboxylic acids under mild and sonochemical conditions: magnetic and CSD studies. *CrystEngComm*, *20*(26), 3711-3721.

Heidari, A., Mansouri-Torshizi, H., Saeidifar, M., Dehghanian, E., Abdi, K., & Delarami, H. S. (2022). Diverse coordination of dipicolinic acid to Pd (II) ion result antitumor complexes, their interaction with CT-DNA by spectroscopic experiments and computational methods. *Journal of Molecular Structure*, *1261*, 132937.

Henríquez, R., Mestra-Acosta, A. S., Muñoz, E., Grez, P., Navarrete-Astorga, E., & Dalchiele, E. A. (2021). High-performance asymmetric supercapacitor based on

CdCO 3/CdO/Co 3 O 4 composite supported on Ni foam. *RSC advances*, *11*(50), 31557-31565.

Huang, J., Yuan, K., & Chen, Y. (2022). Wide voltage aqueous asymmetric supercapacitors: advances, strategies, and challenges. *Advanced Functional Materials*, *32*(4), 2108107.

Husain, Ahmad & Ahmad, Sufiyan & Ansari, Shahid Pervez. (2021). Electrical Conductivity and Structural Studies on Polypyrrole Synthesized in Different Environments. 08. 157-162. 10.22607/IJACS.2020.804005.

Imaduddin, I. S., Majid, S. R., Aziz, S. B., Brevik, I., Yusuf, S. N. F., Brza, M. A., ... & Kadir, M. F. Z. A. (2021). Fabrication of Co3O4 from Cobalt/2, 6-Napthalenedicarboxylic acid metal-organic framework as electrode for supercapacitor application. *Materials*, *14*(3), 573.

Jiang, Y., & Liu, J. (2019). Definitions of pseudocapacitive materials: a brief review. *Energy & Environmental Materials*, *2*(1), 30-37.

Jiao, L., Seow, J. Y. R., Skinner, W. S., Wang, Z. U., & Jiang, H. L. (2019). Metal–organic frameworks: Structures and functional applications. *Materials Today*, *27*, 43-68.

Juni, F. J., Majid, S. R., Yusuf, S. N. F., & Osman, Z. (2021). Electrochemical characteristics of Cu/Cu2O/C composite electrode for supercapacitor application. *Microchemical Journal*, *164*, 106055.

Kaiser, M. R., Han, Z., & Wang, J. (2019). Electro-polymerized polypyrrole film for fabrication of flexible and slurry-free polypyrrole-sulfur-polypyrrole sandwich electrode for the lithium-sulfur battery. *Journal of Power Sources*, *437*, 226925.

Kaynak, A. (2009). Decay of electrical conductivity in p-toluene sulfonate doped polypyrrole films. Fibers and Polymers, 10, 590-593.

Khan, S., Nami, S. A., Siddiqi, K. S., Husain, E., & Naseem, I. (2009). Synthesis and characterization of transition metal 2, 6-pyridinedicarboxylic acid derivatives, interactions of Cu (II) and Ni (II) complexes with DNA in vitro. *Spectrochimica Acta Part A: Molecular and Biomolecular Spectroscopy*, *72*(2), 421-428.

Kim, S., Jang, L. K., Park, H. S., & Lee, J. Y. (2016). Electrochemical deposition of conductive and adhesive polypyrrole-dopamine films. *Scientific reports*, *6*(1), 1-8.

Kouser, S., Hezam, A., Khadri, M. N., & Khanum, S. A. (2022). A review on zeolite imidazole frameworks: Synthesis, properties, and applications. *Journal of Porous Materials*, *29*(3), 663-681.

Krasnovskaya, O., Naumov, A., Guk, D., Gorelkin, P., Erofeev, A., Beloglazkina, E., & Majouga, A. (2020). Copper coordination compounds as biologically active agents. *International Journal of Molecular Sciences*, *21*(11), 3965.

Kremer, M., & Englert, U. (2019). Zn and Ni complexes of pyridine-2, 6-dicarboxylates: crystal field stabilization matters!. *Acta Crystallographica Section E: Crystallographic Communications*, *75*(6), 903-911.

Kumar, A., Singh, R. K., Singh, H. K., Srivastava, P., & Singh, R. (2014). Enhanced capacitance and stability of p-toluenesulfonate doped polypyrrole/carbon composite for electrode application in electrochemical capacitors. *Journal of Power Sources*, *246*, 800-807.

Laschuk, N. O., Easton, E. B., & Zenkina, O. V. (2021). Reducing the resistance for the use of electrochemical impedance spectroscopy analysis in materials chemistry. *RSC advances*, *11*(45), 27925-27936.

Lazanas, A. C., & Prodromidis, M. I. (2023). Electrochemical Impedance Spectroscopy─ A Tutorial. *ACS Measurement Science Au*.

Li, X., Deng, L., Ma, F., & Yang, M. (2020). A luminous off-on probe for the determination of 2, 6-pyridinedicarboxylic acid as an anthrax biomarker based on water-soluble cadmium sulfide quantum dots. *Microchimica Acta*, *187*, 1-8.

Liao, Q., Hou, H., Duan, J., Liu, S., Yao, Y., Dai, Z., ... & Li, D. (2017). Composite sodium p-toluene sulfonate–polypyrrole–iron anode for a lithium-ion battery. *Journal of Applied Polymer Science*, *134*(24).

Liao, Q., Hou, H., Duan, J., Liu, S., Yao, Y., Dai, Z., ... & Li, D. (2017). Composite sodium p-toluenesulfonate/polypyrrole/TiO2 nanotubes/Ti anode for sodium ion battery. *International Journal of Hydrogen Energy*, *42*(17), 12414-12419.

Liu, C., Neale, Z. G., & Cao, G. (2016). Understanding electrochemical potentials of cathode materials in rechargeable batteries. *Materials Today*, *19*(2), 109-123.

Liu, J. Q., Luo, Z. D., Pan, Y., Singh, A. K., Trivedi, M., & Kumar, A. (2020). Recent developments in luminescent coordination polymers: Designing strategies, sensing application and theoretical evidences. *Coordination chemistry reviews*, *406*, 213145.

Liu, Q., Zhang, H., Xie, J., Liu, X., & Lu, X. (2020). Recent progress and challenges of carbon materials for Zn-ion hybrid supercapacitors. *Carbon Energy*, *2*(4), 521-539.

Ma, Y., Yang, H., Zuo, H., Zuo, Q., He, X., Chen, W., & Wei, R. (2023). EG@ Bi-MOF derived porous carbon/lauric acid composite phase change materials for thermal management of batteries. *Energy*, *272*, 127180.

Madani, A., Nessark, B., Boukherroub, R., & Chehimi, M. M. (2011). Preparation and electrochemical behaviour of PPy–CdS composite films. *Journal of electroanalytical chemistry*, *650*(2), 176-181.

Majumdar, D. (2021). Recent progress in copper sulfide based nanomaterials for high energy supercapacitor applications. *Journal of Electroanalytical Chemistry*, *880*, 114825.

Majumdar, D., & Ghosh, S. (2021). Recent advancements of copper oxide based nanomaterials for supercapacitor applications. *Journal of Energy Storage*, *34*, 101995.

Majumder, A., Gramlich, V., Rosair, G. M., Batten, S. R., Masuda, J. D., El Fallah, M. S., ... & Mitra, S. (2006). Five new cobalt (II) and copper (II)-1, 2, 4, 5-benzenetetracarboxylate supramolecular architectures: Syntheses, structures, and magnetic properties. *Crystal growth & design*, *6*(10), 2355-2368.

Malinowski, J., Zych, D., Jacewicz, D., Gawdzik, B., & Drzeżdżon, J. (2020). Application of coordination compounds with transition metal ions in the chemical industry—A review. *International Journal of Molecular Sciences*, *21*(15), 5443.

Mallakpour, S., Nikkhoo, E., & Hussain, C. M. (2022). Application of MOF materials as drug delivery systems for cancer therapy and dermal treatment. *Coordination Chemistry Reviews*, *451*, 214262.

Manyani, N., Siwatch, P., Rana, S., Sharma, K., & Tripathi, S. K. (2023). Study of electrochemical behaviour of binder-free nickel metal-organic framework derived by benzene-1, 3, 5-tricarboxylic acid for supercapacitor electrode. *Materials Research Bulletin*, *165*, 112320.

Mao, H., Ji, C., Liu, M., Cao, Z., Sun, D., Xing, Z., ... & Song, X. M. (2018). Enhanced catalytic activity of Ag nanoparticles supported on polyacrylamide/polypyrrole/graphene oxide nanosheets for the reduction of 4-nitrophenol. *Applied Surface Science*, *434*, 522-533.

Martak, F., & Christanti, T. A. (2014). Synthesis and Toxicity Test Of Zinc (II) Pyridine-2, 6-Dicarboxylate Complexes. *IPTEK The Journal for Technology and Science*, *25*(1).

Megha, R., Ravikiran, Y. T., Kumari, S. V., Rajprakash, H. G., Manjunatha, S., Revanasiddappa, M., ... & Thomas, S. (2020). AC conductivity studies in copper decorated and zinc oxide embedded polypyrrole composite nanorods: Interfacial effects. *Materials Science in Semiconductor Processing*, *110*, 104963.

Melot, B. C., & Tarascon, J. M. (2013). Design and preparation of materials for advanced electrochemical storage. *Accounts of chemical research*, *46*(5), 1226-1238.

Meng, Q., Cai, K., Chen, Y., & Chen, L. (2017). Research progress on conducting polymer based supercapacitor electrode materials. *Nano Energy*, *36*, 268-285.

Muhamad, S. U., Idris, N. H., Yusoff, H. M., Din, M. M., & Majid, S. R. (2017). In-situ encapsulation of nickel nanoparticles in polypyrrole nanofibres with enhanced performance for supercapacitor. *Electrochimica Acta*, *249*, 9-15.

Mulik, S. V., Jadhav, S. A., Patil, P. S., & Delekar, S. D. (2022). Transition metal oxide–conducting polymer nanocomposites and metal-organic framework-based composites for supercapacitor application. In *Advances in Metal Oxides and Their Composites for Emerging Applications* (pp. 135-185). Elsevier.

Murinzi, T. W., Hosten, E., & Watkins, G. M. (2017). Synthesis and characterization of a cobalt-2, 6-pyridinedicarboxylate MOF with potential application in electrochemical sensing. *Polyhedron*, *137*, 188-196.

Mustafa, S. K., Aljohani, M. M., Alessa, A. H., Al-Aoh, H. A., Abdelaziz, M. A., Omer, N., ... & Ahmad, F. (2023). Soft Robotic Actuation Facilitated by Polypyrrole Coated-Sulfonated Polyvinyl Alcohol-Graphene Oxide-ZnO Network-Based Nanocomposite Membranes. *Journal of Polymers and the Environment*, 1-13.

Nezakati, T., Seifalian, A., Tan, A., & Seifalian, A. M. (2018). Conductive polymers: opportunities and challenges in biomedical applications. *Chemical reviews*, *118*(14), 6766-6843.

Nguyen, L. H., Tran, D. P., & Truong, T. N. (2022). Computational Study on the Nature of Bonding between Silver Ions and Nitrogen Ligands. *ACS omega*, *7*(49), 45231-45238.

Noori, A., El-Kady, M. F., Rahmanifar, M. S., Kaner, R. B., & Mousavi, M. F. (2019). Towards establishing standard performance metrics for batteries, supercapacitors and beyond. *Chemical Society Reviews*, *48*(5), 1272-1341.

Norkus, E., Stalnionienė, I., & Crans, D. C. (2003). Interaction of pyridine-and 4-hydroxypyridine-2, 6-dicarboxylic acids with heavy metal ions in aqueous solutions. *Heteroatom Chemistry: An International Journal of Main Group Elements*, *14*(7), 625-632.

Okabe, N., & Oya, N. (2000). Copper (II) and zinc (II) complexes of pyridine-2, 6-dicarboxylic acid. *Acta Crystallographica Section C: Crystal Structure Communications*, *56*(3), 305-307.

Olabi, A. G., Abbas, Q., Al Makky, A., & Abdelkareem, M. A. (2022). Supercapacitors as next generation energy storage devices: Properties and applications. *Energy*, *248*, 123617.

Otero, R., de Parga, A. V., & Gallego, J. M. (2017). Electronic, structural and chemical effects of charge-transfer at organic/inorganic interfaces. *Surface Science Reports*, *72*(3), 105-145.

P Mahore, R., K Burghate, D., B Kondawar, S., P Mahajan, A., & V Nandanwar, D. (2018). Polypyrrole/MnO2 nanocomposites as potential electrodes for supercapacitor. *Advanced Materials Letters*, *9*(8), 538-543.

Pang, A. L., Arsad, A., & Ahmadipour, M. (2021). Synthesis and factor affecting on the conductivity of polypyrrole: a short review. *Polymers for Advanced Technologies*, *32*(4), 1428-1454.

Parnell, C. M., Chhetri, B. P., Mitchell, T. B., Watanabe, F., Kannarpady, G., RanguMagar, A. B., ... & Ghosh, A. (2019). Simultaneous electrochemical deposition of cobalt complex and poly (pyrrole) thin films for supercapacitor electrodes. *Scientific reports*, *9*(1), 5650.

Patterson, N., Xiao, B., & Ignaszak, A. (2020). Polypyrrole decorated metal–organic frameworks for supercapacitor devices. *RSC advances, 10*(34), 20162-20172.

Pérez-Torres, A. F., González-Hernández, M., Ortiz, P., & Cortés, M. T. (2022). Statistical Study of the Influence of Electrosynthesis Conditions on the Capacitance of Polypyrrole. ACS omega, 7(18), 15580-15595.

Purty, B., Choudhary, R. B., Biswas, A., & Udayabhanu, G. (2018). Potentially enlarged supercapacitive values for CdS-PPY decorated rGO nanocomposites as electrode materials. *Materials Chemistry and Physics, 216*, 213-222.

Qin, Z., Xu, Y., Liu, L., Liu, M., Zhou, H., Xiao, L., ... & Chen, C. (2022). Ni-MOF composite polypyrrole applied to supercapacitor energy storage. *RSC advances*, *12*(45), 29177-29186.

Rafique, S., Rashid, I., & Sharif, R. (2021). Cost effective dye sensitized solar cell based on novel Cu polypyrrole multiwall carbon nanotubes nanocomposites counter electrode. *Scientific Reports, 11*(1), 14830.

Ramachandran, R., Xuan, W., Zhao, C., Leng, X., Sun, D., Luo, D., & Wang, F. (2018). Enhanced electrochemical properties of cerium metal–organic framework based composite electrodes for high-performance supercapacitor application. *RSC advances*, *8*(7), 3462-3469.

Rodtuk, N., Takeuchi, K., Hirai, T., Nakamura, Y., Sajomsang, W., Chaiyasat, P., ... & Fujii, S. (2023). Antibacterial rattle-type polypyrrole-silver nanocomposite particles synthesized by aqueous chemical oxidative dispersion polymerization. *Chemistry Letters*, *52*(X).

Roy, S., Darabdhara, J., & Ahmaruzzaman, M. (2023). Recent advances of Cu− BTC MOF based engineered materials for the photocatalytic treatment of pharmaceutical wastewater towards environmental remediation. *RSC Sustainability*.

Rueda, F. C. G., & González, J. T. (2020). Electrochemical polymerization of polypyrrole coatings on hard-anodized coatings of the aluminum alloy 2024-T3. *Electrochimica Acta, 347*, 136272.

Sabalová, M., Oriňaková, R., Oriňak, A., Smoradová, I., Kupková, M., & Strečková, M. (2017). Electrocatalytic hydrogen evolution in acidic media using electrodeposited Ag/PPy and Ni/PPy hybrid materials. *Chemical Papers, 71*, 513-523.

Saikia, P., Dutta, K., Guha, A. K., Dolui, S. K., Barman, P., & Borthakur, L. J. (2021). High-performance aqueous electrolyte based supercapacitor of carboxylic acid functionalized carbon-nanotubes and graphene nano composite. *Materials Chemistry and Physics, 258*, 123786.

Sarno, M. (2020). Catalysis, Green Chemistry and Sustainable Energy. *Edited A. Basile, G. Centi, M. De Falco and G. Iaquaniello, 179*, 431-458.

Sarno, M. (2020). Nanotechnology in energy storage: The supercapacitors. In *Studies in surface science and catalysis* (Vol. 179, pp. 431-458). Elsevier.

Scaldini, F. M., Corrêa, C. C., Yoshida, M. I., Krambrock, K., & Machado, F. C. (2014). 2-D coordination polymers of copper and cobalt with 3, 4-pyridinedicarboxylic acid: synthesis, characterization, and crystal structures. *Journal of Coordination Chemistry*, *67*(18), 2967-2982.

Scindia, S. S., Kamble, R. B., & Kher, J. A. (2019). Nickel ferrite/polypyrrole core-shell composite as an efficient electrode material for high-performance supercapacitor. AIP Advances, 9(5), 055218.

Sethi, M., Shenoy, U. S., & Bhat, D. K. (2020). A porous graphene–NiFe 2 O 4 nanocomposite with high electrochemical performance and high cycling stability for energy storage applications. *Nanoscale Advances*, *2*(9), 4229-4241.

Shahroosvand, H., Nasouti, F., Sousaraei, A., Mohajerani, E., & Khabbazi, A. (2013). Enhancement of electroluminescence in zirconium poly carboxylic acid-based light emitting diodes by bathophenanthroline ligand. *Physical Chemistry Chemical Physics*, *15*(24), 9899-9906.

Shan, Y., Zhao, J., Li, W., Huang, Q., & Xiao, C. (2018). Dual effect of polypyrrole doping on cadmium sulfide for enhanced photocatalytic activity and robust photostability. *Journal of Materials Science*, *53*, 2065-2076.

Sharma, P., & Kumar, V. (2020). Current technology of supercapacitors: A review. *Journal of Electronic Materials*, *49*(6), 3520-3532.

Shen, M., Chen, L., Ren, S., Chen, Y., Li, W., Zheng, R., ... & Han, D. (2021). Construction of CuO/PPy heterojunction nanowire arrays on copper foam as integrated binder-free electrode material for high-performance supercapacitor. *Journal of Electroanalytical Chemistry*, *891*, 115272.

Shimazaki, Y., Stack, T. D. P., & Storr, T. (2009). Detailed evaluation of the geometric and electronic structures of one-electron oxidized group 10 (Ni, Pd, and Pt) metal (II)-(disalicylidene) diamine complexes. *Inorganic chemistry*, *48*(17), 8383-8392.

Shimoga, G., Palem, R. R., Choi, D. S., Shin, E. J., Ganesh, P. S., Saratale, G. D., ... & Kim, S. Y. (2021). Polypyrrole-Based Metal Nanocomposite Electrode Materials for High-Performance Supercapacitors. *Metals*, *11*(6), 905.

Shin, S. J., Gittins, J. W., Balhatchet, C. J., Walsh, A., & Forse, A. C. (2023). Metal–Organic Framework Supercapacitors: Challenges and Opportunities. *Advanced Functional Materials*, 2308497.

Shrivastav, V., Sundriyal, S., Goel, P., Kaur, H., Tuteja, S. K., Vikrant, K., ... & Deep, A. (2019). Metal-organic frameworks (MOFs) and their composites as electrodes for lithium battery applications: Novel means for alternative energy storage. *Coordination Chemistry Reviews*, *393*, 48-78.

Singh, A., Goswami, A., & Nain, S. (2020). Enhanced antibacterial activity and photo-remediation of toxic dyes using Ag/SWCNT/PPy based nanocomposite with core–shell structure. *Applied Nanoscience*, *10*, 2255-2268.

Singh, A., Salmi, Z., Joshi, N., Jha, P., Decorse, P., Lecoq, H., ... & Chehimi, M. M. (2013). Electrochemical investigation of free-standing polypyrrole–silver nanocomposite films: a substrate free electrode material for supercapacitors. RSC advances, 3(46), 24567-24575.

Singh, N., Chand, S., & Taunk, M. (2021). Facile in-situ synthesis, microstructural, morphological and electrical transport properties of polypyrrole-cuprous iodide hybrid nanocomposites. *Journal of Solid State Chemistry*, *303*, 122501.

Škodová, J., Kopecký, D., Vrňata, M., Varga, M., Prokeš, J., Cieslar, M., ... & Stejskal, J. (2013). Polypyrrole–silver composites prepared by the reduction of silver ions with polypyrrole nanotubes. *Polymer Chemistry*, *4*(12), 3610-3616.

Song, H., Li, T., Han, Y., Wang, Y., Zhang, C., & Wang, Q. (2016). Optimizing the polymerization conditions of conductive polypyrrole. *Journal of Photopolymer Science and Technology*, *29*(6), 803-808.

Sriram, G., Kurkuri, M., & Oh, T. H. (2023). Recent Trends in Highly Porous Structured Carbon Electrodes for Supercapacitor Applications: A Review. *Energies*, *16*(12), 4641.

Stejskal, J., Trchová, M., Bober, P., Morávková, Z., Kopecký, D., Vrňata, M., ... & Watzlová, E. (2016). Polypyrrole salts and bases: superior conductivity of nanotubes and their stability towards the loss of conductivity by deprotonation. RSC advances, 6(91), 88382-88391.

Su, N. (2015). Stability, and Solubility of Polyaniline-Polypyrrole Nanocomposite by Doping with Anionic Spherical Polyelectrolyte Brushes. *Nanoscale Res. Lett*, *10*, 301.

Sultana, I., Rahman, M. M., Li, S., Wang, J., Wang, C., Wallace, G. G., & Liu, H. K. (2012). Electrodeposited polypyrrole (PPy)/para (toluene sulfonic acid)(pTS) free-standing film for lithium secondary battery application. *Electrochimica acta*, *60*, 201-205.

Sundriyal, S., Kaur, H., Bhardwaj, S. K., Mishra, S., Kim, K. H., & Deep, A. (2018). Metal-organic frameworks and their composites as efficient electrodes for supercapacitor applications. Coordination Chemistry Reviews, 369, 15-38.

Sutar, R. A., Kumari, L., & Murugendrappa, M. V. (2019). Room temperature ac conductivity, dielectric properties and impedance analysis of polypyrrole-zinc cobalt oxide (PPy/ZCO) composites. *Physica B: Condensed Matter*, *573*, 36-44.

Tan, Y., & Ghandi, K. (2013). Kinetics and mechanism of pyrrole chemical polymerization. *Synthetic metals*, *175*, 183-191.

Tang, C., Chen, N., & Hu, X. (2017). Conducting polymer nanocomposites: Recent developments and future prospects. *Conducting Polymer Hybrids*, 1-44.

Tang, H., Zheng, M., Hu, Q., Chi, Y., Xu, B., Zhang, S., ... & Pang, H. (2018). Derivatives of coordination compounds for rechargeable batteries. Journal of Materials Chemistry A, 6(29), 13999-14024.

Tian, F., Zhang, Y., Liu, L., Zhang, Y., Shi, Q., Zhao, Q., ... & Song, X. (2020). Spongy p-toluenesulfonic acid-doped polypyrrole with extraordinary rate performance as durable anodes of sodium-ion batteries at different temperatures. *Langmuir*, *36*(49), 15075-15081.

Tığ, G. A., Zeybek, B., & Pekyardımcı, Ş. (2016). Electrochemical DNA biosensor based on poly (2, 6-pyridinedicarboxylic acid) modified glassy carbon electrode for the determination of anticancer drug gemcitabine. *Talanta*, *154*, 312-321.

Truong, V. T. (1992). Thermal degradation of polypyrrole: effect of temperature and film thickness. Synthetic metals, 52(1), 33-44.

Tsivadze, A. Y., Aksyutin, O. E., Ishkov, A. G., Knyazeva, M. K., Solovtsova, O. V., Men'shchikov, I. E., ... & Grachev, V. A. (2019). Metal-organic framework structures: Adsorbents for natural gas storage. *Russian Chemical Reviews*, *88*(9), 925.

Vera, R., Schrebler, R., Grez, P., & Romero, H. (2014). The corrosion-inhibiting effect of polypyrrole films doped with p-toluene-sulfonate, benzene-sulfonate or dodecyl-sulfate anions, as coating on stainless steel in NaCl aqueous solutions. *Progress in Organic Coatings*, *77*(4), 853-858.

Vijayan, S. (2020). Just Add Water: For Instant and Scalable Conversion of Metal Acetate to Metal-Organic Frameworks.

Wang, A., Zhao, W., & Yu, W. (2015). Effect of acid/base on the third-order optical nonlinearity of polypyrrole. *Journal of Molecular Structure*, *1099*, 291-296.

Wang, B., Li, W., Liu, Z., Duan, Y., Zhao, B., Wang, Y., & Liu, J. (2020). Incorporating Ni-MOF structure with polypyrrole: enhanced capacitive behavior as electrode material for supercapacitor. *RSC Advances*, *10*(21), 12129-12134.

Wang, H. N., Zhang, M., Zhang, A. M., Shen, F. C., Wang, X. K., Sun, S. N., ... & Lan, Y. Q. (2018). Polyoxometalate-based metal–organic frameworks with conductive polypyrrole for supercapacitors. *ACS applied materials & interfaces*, *10*(38), 32265-32270.

Wang, J., Fu, D., Ren, B., Yu, P., Zhang, X., Zhang, W., & Kan, K. (2019). Design and fabrication of polypyrrole/expanded graphite 3D interlayer nanohybrids towards high capacitive performance. *RSC advances*, *9*(40), 23109-23118.

Wang, M. (2016). Emerging multifunctional NIR photothermal therapy systems based on polypyrrole nanoparticles. *Polymers*, *8*(10), 373.

Wang, T., Wang, Y., Zhang, D., Hu, X., Zhang, L., Zhao, C., ... & Ma, Z. F. (2021). Structural tuning of a flexible and porous polypyrrole film by a template-assisted method for enhanced capacitance for supercapacitor applications. *ACS Applied Materials & Interfaces*, *13*(15), 17726-17735.

Wang, Y., Odoko, M., & Okabe, N. (2004). (6-Carboxylatopyridine-2-carboxylic acid-κ2N, O)(pyridine-2, 6-dicarboxylic acid-κ2N, O) silver (I) dihydrate. *Acta Crystallographica Section E: Structure Reports Online*, *60*(8), m1178-m1180.

Weller, M., Weller, M. T., Overton, T., Rourke, J., & Armstrong, F. (2014). *Inorganic chemistry*. Oxford University Press, USA.

Wen, X., Zhang, Q., & Guan, J. (2020). Applications of metal–organic framework-derived materials in fuel cells and metal-air batteries. *Coordination Chemistry Reviews*, *409*, 213214.

Winarta, J., Shan, B., Mcintyre, S. M., Ye, L., Wang, C., Liu, J., & Mu, B. (2019). A decade of UiO-66 research: a historic review of dynamic structure, synthesis mechanisms, and characterization techniques of an archetypal metal–organic framework. *Crystal Growth & Design*, *20*(2), 1347-1362.

Wu, H. B., & Lou, X. W. (2017). Metal-organic frameworks and their derived materials for electrochemical energy storage and conversion: Promises and challenges. *Science Advances*, *3*(12), eaap9252.

Xie, Y. (2019). Electrochemical performance of transition metal-coordinated polypyrrole: A mini review. *The Chemical Record*, *19*(12), 2370-2384.

Xuan, L., Chen, L., Yang, Q., Chen, W., Hou, X., Jiang, Y., ... & Yuan, Y. (2015). Engineering 2D multi-layer graphene-like Co 3 O 4 thin sheets with vertically aligned nanosheets as basic building units for advanced pseudocapacitor materials. *Journal of Materials Chemistry A*, *3*(34), 17525-17533.

Xue, J., Yang, Q., Guan, R., Shen, Q., Liu, X., Jia, H., & Li, Q. (2020). High-performance ordered porous Polypyrrole/ZnO films with improved specific capacitance for supercapacitors. *Materials Chemistry and Physics*, *256*, 123591.

Yang, J., Cao, J., Peng, Y., Bissett, M., Kinloch, I. A., & Dryfe, R. A. (2021). Unlocking the energy storage potential of polypyrrole via electrochemical graphene oxide for high performance zinc-ion hybrid supercapacitors. *Journal of Power Sources, 516*, 230663.

Yang, J., Yang, T., Feng, Y., & Jiao, K. (2007). A DNA electrochemical sensor based on nanogold-modified poly-2, 6-pyridinedicarboxylic acid film and detection of PAT gene fragment. *Analytical biochemistry*, *365*(1), 24-30.

Yang, Q., Lu, Z., Sun, X., & Liu, J. (2013). Ultrathin Co3O4 nanosheet arrays with high supercapacitive performance. *Scientific Reports*, *3*(1), 1-7.

Yao, H., Zhang, F., Zhang, G., Luo, H., Liu, L., Shen, M., & Yang, Y. (2018). A novel two-dimensional coordination polymer-polypyrrole hybrid material as a high-performance electrode for flexible supercapacitor. *Chemical Engineering Journal*, *334*, 2547-2557

Yin, W. X., Liu, Y. T., Ding, Y. J., Lin, Q., Lin, X. M., Wu, C. L., ... & Cai, Y. P. (2015). Construction of variable dimensional cadmium (II) coordination polymers from pyridine-2, 3-dicarboxylic acid. *CrystEngComm*, *17*(19), 3619-3626.

Yogeeshwari, R. T., Shreenivasa, L., Krishna, R. H., Prashanth, S. A., Banuprakash, G., & Ashoka, S. (2020). Synthesis of acid resistant Fe2V4O13-polypyrrole nanocomposite: its application towards the fabrication of disposable electrochemical sensor for the detection of As (III). *Materials Research Express*, *6*(12), 126448.

Yong Jung, J., & Soo Yi, S. (2021). Enhanced Photoluminescence Properties of Polyhedral Oligomeric Silsesquioxane-Based Hybrid Phosphors for Anti-Counterfeiting and Flexible Composite Applications. *Science of Advanced Materials*, *13*(5), 748-754.

Yu, J., Fu, N., Zhao, J., Liu, R., Li, F., Du, Y., & Yang, Z. (2019). High specific capacitance electrode material for supercapacitors based on resin-derived nitrogen-doped porous carbons. *ACS omega*, *4*(14), 15904-15911.

Yu, L., Lu, L., Zhou, X., Xu, L., Alhalili, Z., & Wang, F. (2021). Strategies for Fabricating High-Performance Electrochemical Energy-Storage Devices by MXenes. *ChemElectroChem*, *8*(11), 1948-1987.

Yu, Z., Tetard, L., Zhai, L., & Thomas, J. (2015). Supercapacitor electrode materials: nanostructures from 0 to 3 dimensions. *Energy & Environmental Science*, *8*(3), 702-730.

Yuan, T., Ruan, J., Zhang, W., Tan, Z., Yang, J., Ma, Z. F., & Zheng, S. (2016). Flexible overoxidized polypyrrole films with orderly structure as high-performance anodes for Li-and Na-ion batteries. *ACS Applied Materials & Interfaces*, *8*(51), 35114-35122.

Yue, L., Wang, D., Wu, Z., Zhao, W., Ren, Y., Zhang, L., ... & Sun, X. (2022). Polyrrole-encapsulated Cu2Se nanosheets in situ grown on Cu mesh for high stability sodium-ion battery anode. *Chemical Engineering Journal*, *433*, 134477.

Yussuf, A., Al-Saleh, M., Al-Enezi, S., & Abraham, G. (2018). Synthesis and characterization of conductive polypyrrole: the influence of the oxidants and monomer on the electrical, thermal, and morphological properties. *International Journal of Polymer Science*, *2018*.

Zang, Q., Zhong, G. Q., & Wang, M. L. (2015). A copper (II) complex with pyridine-2, 6-dicarboxylic acid: synthesis, characterization, thermal decomposition, bioactivity and interactions with herring sperm DNA. *Polyhedron*, *100*, 223-230.

Zayan, S., Elshazly, A., & Elkady, M. (2020). In situ polymerization of polypyrrole@ aluminum fumarate metal–organic framework hybrid nanocomposites for the application of wastewater treatment. Polymers, 12(8), 1764.

Zhang, D. M., Xu, C. G., Liu, Y. Z., Fan, C. B., Zhu, B., & Fan, Y. H. (2020). A series of coordination polymers based on 2, 6-pyridinedicarboxylic acid ligand: Synthesis, crystal structures, photo-catalysis and fluorescent sensing. *Journal of Solid State Chemistry*, *290*, 121549.

Zhang, R., Chen, C., Yu, H., Cai, S., Xu, Y., Yang, Y., & Chang, H. (2021). All-solid-state wire-shaped asymmetric supercapacitor based on binder-free CuO nanowires on copper wire and PPy on carbon fiber electrodes. *Journal of Electroanalytical Chemistry*, *893*, 115323.

Zhang, S., & Pan, N. (2015). Supercapacitors performance evaluation. *Advanced Energy Materials*, *5*(6), 1401401.

Zhang, Y., Liu, J., Li, S. L., Su, Z. M., & Lan, Y. Q. (2019). Polyoxometalate-based materials for sustainable and clean energy conversion and storage. *EnergyChem*, *1*(3), 100021.

Zhao, J., Li, W., Fan, L., Quan, Q., Wang, J., & Xiao, C. (2019). Yolk-porous shell nanospheres from siliver-decorated titanium dioxide and silicon dioxide as an enhanced visible-light photocatalyst with guaranteed shielding for organic carrier. *Journal of colloid and interface science*, *534*, 480-489.

Zhu, C., Zhai, J., Wen, D., & Dong, S. (2012). Graphene oxide/polypyrrole nanocomposites: one-step electrochemical doping, coating and synergistic effect for energy storage. Journal of Materials Chemistry, 22(13), 6300-6306.